

Lithophile and Chalcophile Elements in Sphalerite from the Anarraaq Sediment-Hosted Zn-Pb-Ag Deposit, Red Dog District, Alaska

by

Devon Smith

A thesis submitted in partial fulfillment of the requirements for the degree of

Master of Science

Department of Earth and Atmospheric Sciences
University of Alberta

© Devon Smith, 2017

Abstract

The age of many sedimentary hosted base metal deposits has been a topic of debate for several decades, due to a lack of minerals ideal for geochronological age in these systems. One technique is focused on dating the ore minerals (sphalerite) directly with the Rb-Sr method. The main issue with the application of this technique is that the location of the Rb and Sr has never been definitively identified in sphalerite. It has been proposed that the Rb and Sr could be lattice bound, perhaps involved in a coupled substitution, however, this is unlikely due to the much larger size of these ions, relative to Zn. Furthermore it has been suggested that the Rb and Sr could potentially reside in mineral inclusions within the sphalerite which would compromise the accuracy of the method. This study uses sphalerite from the Anarraaq deposit, Alaska, to address whether the Rb and Sr are hosted in the sphalerite or in mineral inclusions which may not be co-genetic with sphalerite precipitation.

The Red Dog district of Alaska is a world class sediment-hosted Zn-Pb district. The Anarraaq deposit lies approximately 10 km NW of the main Red Dog deposits and hosts an additional inferred resource of 19.4 Mt at 14.4% Zn and 4.2% Pb. Zinc-lead mineralization in the Red Dog district is hosted by organic-rich mudstones which were deposited in a passive margin setting in the mid-late Mississippian. The Anarraaq sphalerite has been divided into 6 distinct generations based on textural variation and cross-cutting relationships. Variability in color also exists within each of the 6 sphalerite stages and textures include spherical, fibrous, bladed, and oscillatory zoned colloform banding.

Following characterization of the textural variability and reconnaissance electron microprobe analyses (EMPA), element mapping of Rb, Sr, Al, Si, Fe, Cu, Ge, As, Ag, Cd, Sb, Hg, Tl, and Pb was conducted using laser ablation inductively coupled plasma mass

spectrometry (LA-ICPMS). The laser was modified with an aerosol rapid induction system (ARIS). This advanced mapping technique involved using a series of high speed laser ablated line scans combined with unconventional laser ablation operating conditions such as low laser fluence and high laser repetition rate.

This application of LA-ICPMS mapping provides new information about the complexities of trace element distributions in Anarraaq sphalerite which include Fe controlled oscillatory zoning, oscillatory zoning independent of Fe content, sector zoning, and mineral inclusions. Strontium is mostly hosted in carbonate mineral inclusions within the sphalerite. This study does not show evidence that supports a coupled substitution involving Rb in the sphalerite lattice. Rubidium is hosted in silicate mineral inclusions which cannot be determined to be syngenetic with the sphalerite and this would prevent any accurate Rb-Sr dating of this deposit.

Acknowledgements

I would like to thank my advisor, Dr. Sarah Gleeson for her generous guidance and patience throughout this process. Sarah gave me this opportunity despite my very non-traditional path in life and remained by my side even after she relocated >7,200 km away. Thanks also to my co-advisor, Dr. Graham Pearson, who provided valuable insight and made time for me even when he had no time to spare.

Sample preparation and analytical work was provided from PhD funding for Merilie Reynolds by Teck Resources Limited and a Natural Sciences and Engineering Research Council of Canada (NSERC) Collaborative Research Development Grant awarded to Dr. Sarah Gleeson, Dr. Robert Creaser and Teck. Additional EPMA analytical funding was provided by a NSERC Discovery grant awarded to Dr. Sarah Gleeson. The LA-ICPMS work completed at the University of Alberta was funded by the Canada Excellence Research Chairs program awarded to Dr. Graham Pearson. The Trinity College Dublin LA-ICPMS analyses were funded from a Helmholtz-Rekrutierungsinitiative provided to Dr. Sarah Gleeson.

Dr. Andrew Locock, Dr. Yan Luo, Dr. Andy DuFrane, and Cora McKenna are greatly appreciated for analytical assistance.

Merilie Reynolds, Alex Sheen, Michael Rogers, and Dr. Yannick Bussweiler should also be thanked for their time with numerous discussions, even when it was really just listening to my confusion and frustrations.

Finally, I would like to thank my husband, Andrew, for all his help throughout this process, patience when I was not at my best, and listening to me even when he had no idea what I was talking about.

Table of Contents

1	Introduction	1
1.1	Sphalerite	1
1.1.1	Sphalerite Rb-Sr Dating and Methodology	2
1.1.2	Where is the Rb and Sr in the sphalerite?	5
1.2	Red Dog Sphalerite	6
2	Geologic Background	8
2.1	District Geology	8
2.2	Anarraaq Deposit	9
3	Methods	11
3.1	EPMA	12
3.1.1	JEOL JXA-8900 Superprobe – University of Alberta	12
3.1.2	CAMECA SX100 – University of Alberta	14
3.1.3	JEOL JXA-8500F Hyperprobe – GFZ, Potsdam, Germany	16
3.2	LA-ICPMS	16
3.2.1	Thermo Element XR – University of Alberta	17
3.2.2	Thermo iCapQc – University of Alberta	18
3.2.3	Thermo iCapQs – Trinity College, Dublin, Ireland	21
4	Results	26
4.1	Lower Ore Zone	28
4.1.1	Sphalerite L1	28
4.1.2	Sphalerite L2	42
4.1.3	Sphalerite L3	58
4.1.4	Sphalerite L4	63
4.1.5	Sphalerite L5	73
4.2	Upper Ore Zone	78
4.2.1	Sphalerite U1	78
5	Discussion	89
5.1	Potential alteration of sphalerite composition during the Brookian Orogeny	89
5.2	Chalcophile elements in sphalerite	89
5.3	Controls on trace element distribution	94

5.3.1	Fluid mixing.....	94
5.3.2	Fluid-rock interaction.....	95
5.3.3	Co-precipitation of a sulfide assemblage.....	96
5.3.4	Physiochemical changes	97
5.3.5	Lattice-scale controls	99
5.4	Distribution of Rb in sphalerite	99
5.5	Distribution of Sr in sphalerite	101
5.6	Implications for the Rb-Sr dating of sphalerite.....	102
5.7	Distribution of Na in sphalerite.....	104
5.8	Implications for geometallurgy.....	104
6	Conclusions	105
6.1	Future work	106
	References.....	108
	Appendix A: EPMA Quantitative Spot Analyses	doi:10.7939/DVN/FHE6LC
	Appendix B: JEOL JXA8900 Images.....	doi:10.7939/DVN/SWEUWM
	Appendix C: CAMECA SX100 Images.....	doi:10.7939/DVN/KBJ4SG
	Appendix D: JEOL JXA8500F Images.....	doi:10.7939/DVN/FW34UI
	Appendix E: Thermo Element XR2 LA-ICPMS Element Maps....	doi:10.7939/DVN/FDECI5
	Appendix F: Thermo iCapQc LA-ICPMS Element Maps.....	doi:10.7939/DVN/2LDFQ4
	Appendix G: Thermo iCapQs LA-ICPMS Element Maps.....	doi:10.7939/DVN/WH204W

List of Tables

Table 1: Compilation of deposits which have been dated using Rb-Sr on sphalerite.....	4
Table 2: List of standards and specifications used for JEOL analyses.....	13
Table 3. List of standards and specifications used for CAMECA analyses.....	15
Table 4: Summary of Anarraaq sphalerite stages, textural variation, spatial occurrence, and trace element distribution determined using LA-ICPMS.....	27
Table 5: Descriptive statistics of combined weight percent (Wt%) data of 13 elements obtained from 322 electron probe microanalyses (EPMA) using the wave dispersive spectrometer (WDS) on the JEOL JXA-8900 Superprobe and 18 elements obtained from 189 electron probe microanalyses (EPMA) using the wave dispersive spectrometer (WDS) on the CAMECA SX100.....	33

List of Figures

- Figure 1. (a) Location map of the Red Dog District within the Brooks Range of Northern Alaska. (b) Plot of tonnage versus grade for deposits in the district. The combined main Red Dog deposits consists of Main, Paalaaq, Aqqaluk, and Qanaiyaq. Modified from Graham et al., 2009; Blevings et al., 2013; and Riehle et al., 1997. 7
- Figure 2. (a) Plan view of Anarraaq deposit at depth showing extent of upper and lower ore zones, drill hole, and cross section locations. (b) A-A' cross section showing the location of key samples within the mineralized Ikalukrok unit. (c) B-B' long section shows the location of key samples from the Upper and Lower ore zones. Modified from M. Reynolds and Teck geologists, unpublished.10
- Figure 3. CellSpace images of Rb in sample 923-2277a area 3. (a) CellSpace image with automatically calculated upper limit compared to manually lowered limits (b) and (c) which begin to show additional features in the images. (d) A log scale image is also sometimes helpful at illustrating distinct groups of concentration in the image.23
- Figure 4. A comparison of qualitative X-ray element mapping, quantitative EPMA spot analyses, and semi-quantitative LA-ICPMS element mapping on the same sphalerite L1 area. (a) Iron X-ray element map using a 1 μm /pixel resolution. (b) LA-ICPMS Fe map using a 5 μm laser aperture and MASS-1 standard. (c) LA-ICPMS Fe map using a 20 μm laser aperture and MASS-1 standard. (d) LA-ICPMS Fe map using a 20 μm laser aperture and NIST610 standard. (e) BSE image with locations of EPMA spot analyses. The spot locations are accompanied by Fe wt% data for each location.25
- Figure 5. (a) Reflected light image from sample 923 - 2277.6a showing homogenous sphalerite (sp) replacing spherical pyrite (labeled as black 'py') and fine grained pyrite (labeled as red 'py'). (b) Transmitted light image illustrating spherical sphalerite which has a core and rim structure. Individual spherical sphalerites have been outlined (in white) in both images to emphasize how the spherical structures change in size at depth. An opaque spherical feature only visible in transmitted light is shown in green and is likely a subsurface pyrite feature. (c) Coarser spherical sphalerite surrounded by a dark, non-metallic matrix which is mostly opaque in transmitted light (d). Green box indicates locating of (e) and (f). Dark sphalerite L1a contains abundant very fine pyrite inclusions (e-1). The dark sphalerite is followed by a slight color change in the rim (f-2). Dark

sphalerite is followed by a rim of white to light tan sphalerite L1b (f-3). Within the light rim, a lineation of color is seen which follows the shape of the oscillatory zoning (f-4). The light colored rim is followed by a bright orange L1c sphalerite and an area of darker L1b occurs at the transition (f-5). The matrix material later fills in around and cuts the sphalerite (e-6). Very fine galena later cuts the sphalerite (e-7).....29

Figure 6. Combined JEOL and CAMECA analyses. (a) Zinc wt% versus S wt% plot showing range in Zn and S concentrations relative to pure ZnS (67% Zn, 33% S; shown as black dot). The later stage sphalerite L5 as well as the upper ore zone (U1) plot closest to the ZnS whereas the earlier stages vary significantly from the ZnS. (b) Plot of Zn wt% and Fe wt% showing a strong negative correlation in sphalerite stages L1-L4. R2 values reported are the calculated coefficient of determination (R2). (c) Plot of Zn wt% and Cd wt% which does not show a strong negative correlation, however, a negative trend is observed. Sphalerite L2 strays furthest from the trend. (d) Iron wt% and Cd wt% show a positive trend which is also not a strong correlation. (e) Zinc and Na stages L1-L4 also show a strong negative correlation. (f) Sodium and Cl are not related. (g) Sodium and Fe indicate a variably strong positive correlation which supports the Zn and Na relationship observed.....31

Figure 7. Box plots showing distribution of major and minor elements throughout the sphalerite textures. Red dashed line = LOD. Black dashed line = divide between lower and upper ore zone generations. Filled box represents range in data from first quartile to third quartile. Whiskers represent minimum and maximum in data. Black line = median. Black dot = mean value. Outliers are represented as individual symbols.....32

Figure 8. (a) Transmitted light photomicrograph of oscillatory zoned sphalerite L1 in sample 923 2277.6a. (b) Reflected light photomicrograph showing locations of pyrite and quartz within the sphalerite as well as matrix material which is surrounding the sphere of sphalerite. (c) BSE image of sphalerite stage L1 shows cross cutting galena and locations of spot analyses. Zinc (Zn) X-ray map of sphalerite L1 shows a variation in Zn concentration. Oscillatory zoning is seen in the Fe X-ray map and correlates with the sphalerite color and Zn spatial distribution. Lead (Pb) X-ray map illustrates spatial distribution of cross cutting galena. Silicon (Si), Al, and K X-ray maps show a presence in the matrix as well as cross cutting the sphalerite.....35

Figure 9. Quadrupole laser ablation element mapping of sphalerite L1. The white box represents the area that was mapped. The red lines were traced along the rim of the Fe rich zone and then overlaid on the photomicrograph of the mapped area and the Cd map. Zinc (Zn) and Fe spatially correlate with the oscillatory color zonation, however, Cd and Hg appear independent of the color zoning. The Cd extends past the Fe rich-Fe poor transition (red lines). Mercury is variably present in the Fe rich cores (black arrows). The additional trace element maps show a narrow oscillatory zoning pattern (red arrows) which is independent from the zoning seen in the Fe concentration and L1 color. The innermost zone (lower red arrow) occurs along the rim of the Fe rich L1b sphalerite. An additional narrow band is present within the Fe poor L1b stage of sphalerite (middle red arrow). A third zone is present along the rim of the L1b sphalerite (upper red arrow).....37

Figure 10. Combined JOEL and CAMECA box plots showing spatial distribution of lithophile elements through the sphalerite generations. Red dashed line = LOD. Black dashed line = divide between lower and upper ore zone generations. Box represents range in data from first quartile to third quartile. Whiskers represent minimum and maximum in data. Black line = median. Black dot = mean value. Outliers are represented as individual symbols.....40

Figure 11. Quadrupole laser ablation element maps of L1 sphalerite show the spatial distribution of lithophile elements (white box indicates map area). The Fe rich cores have been traced on the photomicrograph and transferred to the Si, Al, Rb, and Na maps (black lines). The matrix surrounding the sphalerite is rich in Ca, Sr, Si, Al, Rb, and Na. The Si, Al, Rb, and Na are seen in the sphalerite in the areas where the matrix material cuts the sphalerite (blue dashed line) and possibly off sets the lower darker cores (blue arrows indicate sense of potential offset). Calcium and Sr do not cut the sphalerite.....41

Figure 12. (a) Reflected light and (b, c) transmitted light photomicrographs of sample 923 – 2373.4a showing matrix material surrounding sphalerite L2 vein. (a) Sphalerite L2a contains linear inclusions (shown with red arrows). Galena (gl) is located at the center of the banded vein. (a, b) L2 and the matrix are cut by later sphalerite L5, quartz, and marcasite. (c) A closer look at (b) (shown with a red box) shows a rim of dark material which commonly occurs along the sphalerite L2 margin and sphalerite is sparse along this margin. Sphalerite L2 is hosted in L5 and the matrix (blue arrows). (d) Reflected

light and (e) transmitted light photomicrograph of sample 923 - 2251.2a showing bladed sphalerite L2b and sphalerite L2d (bright cream zone). The L2b sphalerite is seen as replacing large (up to 600 μm in length) blades. Inclusions of calcite (cal), pyrite (py), and galena (gl) are seen throughout the L2b sphalerite. (f) Transmitted light photomicrograph of fibrous L2c replacing marcasite. (g) Reflected light and (h) transmitted light photomicrographs of fibrous sphalerite L2c and bladed L2b replacing marcasite. Quartz is occasionally present in the bladed replacement and fibrous L2d rims the L2c.....42

Figure 13. Mosaic of transmitted light photomicrographs showing the relationship between the colloform banded sphalerite textures in sample 923 – 2277.6a. Corresponding quadrupole laser ablation maps show the spatial distribution of trace elements throughout the sphalerite generations. Sphalerite L2 contains Cd, Pb, Hg, Ce, Ge, As, Ag, Sb, and In. Cadmium, Hg, and Sb are more concentrated in the later L2c sphalerite. Sphalerite L3 contains low Fe, Hg, and Ag and increased Cd. Patches of Pb, Cu, As, and Sb are minimally present in L3. Earlier sphalerite L4a and L4b preferentially contain increased Fe and Cd concentrations, however, Pb, Hg, Cu, Ge, Ag, and Sb are concentrated in later sphalerite L4c. Lead is also seen in the matrix material and cutting into L4. Sphalerite L2 and L4c show decreased Fe and increased Pb, Hg, Cu, Ge, As, Ag, and Sb.....44

Figure 14. Thin section photograph of sample 923-2373.4b which contains sphalerite and matrix material distributed in a circular pattern which appears to mimic fluid-like flow. The sphalerite and matrix material is later cut by coarse pyrite/marcasite.....45

Figure 15. (a) Transmitted light photomicrograph of oscillatory zoned sphalerite L2 in sample 923 - 2373.4a. (b) Reflected light photomicrograph showing locations of cross cutting calcite and matrix material (c) BSE image of sphalerite stage L2 and inclusions of galena near the contact with later sphalerite L5. JOEL spot analyses are shown in red, CAMECA in blue. Zinc X-ray map of sphalerite shows zoning in Zn concentration. Oscillatory zoning is faintly seen in the Fe X-ray map and correlates with the color and Zn zoning. Lead X-ray map illustrates spatial distribution of galena in the matrix and in late sphalerite L5. Chlorine X-ray map shows that Cl is not significantly concentrated in stage L2 and the zoning observed is possibly caused by X-ray continuum. Silicon X-ray map shows Si in matrix material and rare inclusions in the sphalerite. Aluminum X-ray map

	shows Al present in the matrix and throughout the sphalerite. Potassium X-ray map shows that K rarely occurs in the matrix.....	46
Figure 16.	(a) Transmitted light photomicrograph of fibrous sphalerite L2c and patchy sphalerite L3 of sample 923 - 2277.6a which is being cut by late pyrite. A complex array of opaque micro veinlets is also seen in the sphalerite. (b) BSE image of sphalerite which shows late pyrite (black) is associated with galena (bright white). JOEL spot analyses are shown in red, CAMECA in blue. Zinc spatial distribution shows that Zn is higher in the later L3 sphalerite. Iron concentrations are higher in L3 and heterogeneously distributed in the L2c sphalerite. A fibrous texture is also seen in the L2c Fe map. Lead X-ray map also shows that galena is associated with late pyrite. Chlorine X-ray map shows that Cl is potentially present as a single fluid inclusion. Aluminum map shows rare, very fine Al. Silicon X-ray map showing significant abundance of Si micro veinlets, sometimes associated with late pyrite.....	48
Figure 17.	Quadrupole laser ablation maps of sphalerite L2 and L5 in sample 923 – 2373.4a show the spatial distribution of elements throughout the variable textures and generations. The spatial distributions have been traced out on the element maps and then overlaid on the transmitted light photomicrograph to observe the pattern of spatial distribution (shown as black lines). Earlier sphalerite L2a is rich in Fe, Cd, and Hg. It also contains patchy Ag. Sphalerite L2b contains less Fe and Cd, and is rich in Pb, Ag, Sb, and patchy Cu and Tl. Sphalerite 2d is rich in Cu, Ag, and As, however zoning is present along the contact between lighter and darker L2d. The lighter zone preferentially contains Fe, Hg, and As. The darker tips of L2d are richer in Pb and Tl. Sphalerite L5 contains minimal trace elements in relation to earlier L2, however, patchy Cd, Hg, and Ge are present.....	49
Figure 18.	Quadrupole laser ablation element maps show the spatial distribution of elements present in fibrous sphalerite L2c and later sphalerite L3 in sample 923 – 2277.6a. The white box on the photomicrograph shows the mapped area. Lead, Cu, Ge, Ag, Sb, and Tl are preferentially distributed in L2c and the fibrous texture is evident in these maps. Cadmium displays heterogeneity and is present in both textures, but absent along the boundary between the two stages. Mercury is also heterogeneous and preferentially is located in the earlier L2 sphalerite. Arsenic is heterogeneous and is likely associated with very fine pyrite inclusions in L2c.....	51

Figure 19. Quadrupole laser ablation trace element maps of lithophile elements distributed in sphalerite L2 and L5. Sodium appears homogeneous throughout the L2 textures but is not present in later L5 sphalerite. Silicon and Al are less common and an area in the top left corner of the maps (white arrow) contains Si, Al, and Rb and appears similar to the opaque matrix material. The Rb map also shows a homogeneous spatial distribution in sphalerite L2b and the darker tips of L2d. This spatial distribution is better illustrated on a log scale map of Rb. Strontium and Ca are associated with the late pyrite and are also seen cross cutting the sphalerite along a micro veinlet. Sodium, Si, and Rb are also associated with the pyrite.....54

Figure 20. Quadrupole laser ablation element map show the spatial distribution of lithophile elements present in sphalerite L2c and L3. The white box on the photomicrograph shows the mapped area. The maps have been overlaid on a reflected light photomicrograph of the area which was taken prior to the mapping. Sodium is preferentially located in L2c and appears homogeneous in this sphalerite. Silicon is heterogeneous and abundant in both textures. Aluminum, Rb, Ca, and Sr are heterogeneous and Ca shows an identical spatial distribution to Sr present.....56

Figure 21. Sphalerite L2c lithophile LA-ICPMS maps continued. The white box on the photomicrograph shows the mapped area. A log scale view of Na and Rb from Figure 20 shows the homogenous spatial distributions in the fibrous L2c texture. Additionally, a comparison of spots in the Si, Al, and Rb maps show that roughly half of the Rb spots spatially correlate with Al and Si also present (the pink boxes are where spots are present amongst all three of the maps).....57

Figure 22. (a) Reflected light photomicrograph shows pyrite, galena, and calcite in the L3 sphalerite. The calcite veins post-date the sphalerite. (b) Transmitted light photomicrograph showing the patchy nature of sphalerite L3. White box represents the area of Figure 23, 24, and 25.....58

Figure 23. (a) Transmitted light and (b) reflected light photomicrograph of sphalerite L3 of sample 923 2277.6b. Opaque inclusions are present at depth in the sphalerite. (c) BSE image of sphalerite which shows calcite (black) spatially associated with the opaque areas. Galena (bright white) is also present and associated with the calcite. Zinc map shows that the Zn concentration is variable in L3 sphalerite. The Fe concentration is

heterogeneously distributed in the L3 sphalerite and the increased Fe spatially correlates with the areas of decreased Zn. Pyrite inclusions appear as pink in the Fe map. Lead X-ray map shows that galena is only present in the same area identified in the BSE (white circle). Silicon x-ray map showing single inclusion of silicon associated with the calcite.....59

Figure 24. Quadrupole laser ablation maps of sphalerite L3 in sample 923 – 2277.6b show that the opaque inclusion area is lower in Fe and Cd content and higher in Pb, Hg, Cu, Ge, As, Ag, Sb, and Tl.....60

Figure 25. Quadrupole laser ablation element maps show the spatial distribution of lithophile elements present in sphalerite L3. The maps have been overlaid on a reflected light photomicrograph of the area which was taken prior to the mapping. Sodium is concentrated in the inclusion rich areas. Silicon is rarely present and associated with the calcite. Aluminum and Rb also show a similar orientation to the calcite and the two maps show little spatial correlation. Strontium is present in the calcite.....62

Figure 26. (a) Reflected light and (b) transmitted light photomicrograph of sample 923 – 2251.2b showing oscillating bands of sphalerite L4. The growth begins with dark reddish brown sphalerite L4a at the bottom of the sequence and ends with light tan sphalerite L4c. (c) Reflected light and (d) transmitted light photomicrograph of sample 923 – 2251.2a showing a banded vein of alternating L4a and L4b bands which is surrounded by an earlier L4c band and all of which are replacing marcasite. (e) Reflected light and (f) transmitted light photomicrograph of sample 923 – 2292.2a showing initial nucleation of a sphalerite L4b core which is then rimmed by L4a and lastly L4b. This sphalerite is associated with colloform banding and not the spherical pyrite as seen in Figure 5. (g) Reflected light and (h) transmitted light photomicrograph of sample 923 – 2251.2a showing a large (~1mm in length) sphalerite blade encased in marcasite (marc). The blade shows zoning from sphalerite L4b at the margins to sphalerite L4a in the center. (i) Higher magnification reflected light photomicrograph (exact area of image indicated in green on image (g) shows submicron sulfide inclusions in the sphalerite. A fibrous texture is also seen along an edge of the blade (red arrow) which is texturally comparable to the fibrous texture of sphalerite L2c and indicates that the sphalerite blade is replacing the marcasite.....64

Figure 27. Mosaic of transmitted light photomicrographs show the relationship between the sphalerite L4 and L5 textures and the later matrix material. Corresponding laser ablation maps show the spatial distribution of trace elements throughout the sphalerite and matrix. Sphalerite L4 contains variable amounts Fe, Cd, Hg, As, Ag, and Sb. The majority of these elements increase toward the very end of the growth (near the L5 contact). Sphalerite L5 hosts Cd and Fe in the darker areas and Hg, Ge, and Ag also show heterogeneity in this texture. The later matrix material contains Pb, Cu, Ge, and Ag. Indium is seen along the boundary between sphalerite L4 and L5.....65

Figure 28. (a) Transmitted light photomicrograph of zoned sphalerite L4 of sample 923 - 2251.2a. (b) BSE image of sphalerite which shows partially replaced pyrite and galena as well as late quartz. CAMECA spot analyses are shown in blue. Zinc spatial distribution shows that Zn is higher in the later L4c sphalerite. Iron concentration correlates with the Zn concentration and a distinct dark zone is visible in the Fe map (white arrows). Pyrite appears as white in the Fe map. Chlorine X-ray map show that Cl is present where the dark zone appears in the Fe map (white arrows). This is better visualized when the images have been combined into a Fe + Cl image (zone shown with white arrows). The arrow location have been transferred to the photomicrograph (black arrows on (a)) to compare to the color of the sphalerite. This shows that the Cl is present along a zone that does not represent the boundary between Fe rich and Fe poor L4 sphalerite. Lead X-ray map shows that galena is mostly associated with pyrite. Silicon X-ray map showing quartz only occurs in the center of the vein. Aluminum map showing occasional Al bearing inclusions in the sphalerite.....67

Figure 29. Quadrupole laser ablation element mapping shows the spatial distribution of elements present in a sphalerite L4 vein in sample 923 – 2251.2a. The white box on the photomicrograph shows the mapped area. The black arrows have been placed on the exact same location of the photomicrograph, the Fe map, and some of the trace element maps to show the correlation within the zones. The black lines on the Fe map represent the thin zones and have been traced out using the Sb map. Using the thin lines combined with the arrow location shows that Pb, Ge, As, Ag, Sb, and Tl occur in the earlier (see left black arrow on these images) zone which also contains Cl (see Figure 28). Additionally, Pb, As, Ag, Sb, and Tl are also present in a less defined zone which is located at the

transition from Fe poor L4c to more Fe rich L4a and L4b (see right black arrow on trace element maps, Fe map, and photomicrograph. The Cd concentration agrees with the Fe zoning. Mercury appear independent of the zoning and is heterogeneous. In addition to the zoning, Pb, Cu, Ge, Ag, Sb, and Tl are also heterogeneously distributed through the L4 sphalerite.....68

Figure 30. Quadrupole laser ablation element maps show the spatial distribution of lithophile elements present in a vein of sphalerite L4. The white box on the photomicrograph shows the mapped area. The maps (excluding the log scale images) have been overlaid on the Fe X-ray map to show presence of lithophile elements relative to the sphalerite zoning, pyrite (bright white), and quartz (dark). Sodium and Rb are also present in the thin outer zone which contains Cl, Pb, Ge, As, Ag, Sb, and Tl (see Figure 28, 29). Sodium and Rb are also present as inclusions and some of these inclusions also host Al, Si, Sr, and Ca. Additionally, Na, Rb, and Sr appear to be nearly homogeneous in log scale images.....71

Figure 31. Sector field laser ablation maps showing the spatial distribution of Fe, Si, Al, Rb, and Sr in sphalerite L4c and more Fe rich L4b. (a) Transmitted light photomicrograph showing location of (b) the mapped area (green box). Silicon appears to be nearly homogeneous in the sphalerite L4. Aluminum is present in a few areas and is mostly located in the lighter, Fe poor L4c sphalerite. Abundant Rb is present and is also preferentially located in the L4c sphalerite. A few areas of Sr rich inclusions are located along the boundary between L4b and L4c and when viewed with a log scale, zoning is evident in the Sr spatial distribution which correlates with the textural zoning and the Sr is nearly homogeneous.....72

Figure 32. (a) Transmitted light and (b) reflected light photomicrograph of L5 sphalerite in sample 923 – 2373.4b. The sphalerite is located in a quartz and pyrite vein. (c) BSE image of sphalerite which shows rare galena present in the pyrite. JOEL spot analyses are shown in red and CAMECA are shown in blue. The Zn spatial distribution shows that a subtle zoning in the Zn concentration is present which negatively correlates with the Fe present in the sphalerite. The Pb X-ray map shows that galena is only associated with the quartz and pyrite and not in the sphalerite. The Si X-ray map highlights the vein quartz and is not present in the sphalerite. Aluminum appears as very fine inclusions distributed throughout some areas of the sphalerite as well as the pyrite and quartz. (f) Chlorine is

only located in significant concentrations within the quartz and pyrite area (top of map).....74

Figure 33. Quadrupole laser ablation element maps show the spatial distribution of elements present in sphalerite L5 of sample 1714 – 2471.2b. The zoning in Fe content correlates with the color zones observed in transmitted light (a). Fluid inclusions as well as inclusions of opaque minerals are visible as imperfections on the sphalerite surface (b) as well as at depth using a high magnification (c). The location of (c) is indicated with a green square in (a). The Cd also correlates with the color zones, however, some areas of higher concentration are present in irregular zones. Many of the other element maps (Pb, Hg, Ge, Ag, Sb, and Tl) also have this irregular zoning which is mostly present in the areas of abundant inclusions. In addition to the irregular zoning, a thin zone is present in the Fe, Pb, Cu, Ge, Ag, Sb, and Tl and spatially correlates with a thin zone of opaque inclusions in the sphalerite (see black arrows).....75

Figure 34. Quadrupole laser ablation element maps show the spatial distribution of lithophile elements present in sphalerite L5. The trace element maps have been overlaid on a reflected light photomicrograph that was taken prior to the analyses. Log scale maps show that Na, Rb, and Sr are also concentrated in areas containing abundant inclusions in the sample. A few of the inclusions in this area also contain Si and Al and Ca is abundant throughout the map. Rubidium and to a lesser degree, Na and Sr, are present in the thin zone which also hosts Fe, Pb, Cu, Ge, Ag, Sb, and Tl (shown in Figure 33).....77

Figure 35. (a) Thin section image of sample 809 – 2332.7a which illustrates the relationship between sphalerite U1a, U1b, and U1c and the layering that is present in this sphalerite generation. The sphalerite has grown around earlier nodular pyrite. Soft sediment deformation features are most prominent between sphalerite U1a and U1b (black arrows). (b) Reflected light and (c) transmitted light image of dark brown sphalerite U1c showing sparse patches of sphalerite in a quartz dominated matrix. (d) Reflected light and (e) transmitted light image of sphalerite U1b showing variably colored sphalerite which is a mixture of U1c and U1a sphalerite. (f) Reflected light and (g) transmitted light image of sphalerite U1a showing dominant concentration of lighter cream colored sphalerite with inclusions of opaque material ((?) - likely mudstone host rock but not sure) and nodular pyrite. Quartz is less abundant in this lower texture of sphalerite.....79

Figure 36. X-ray element maps of sphalerite U1c (top row), U1b (middle row), and U1a (bottom row) indicating the spatial distribution of elements present in each of the sphalerite textures. Pyrite is illustrated in the Fe maps and is rare in U1c. The pyrite concentration decreases up-hole and nodular pyrite is abundant in U1a. The concentration of Pb is very low and difficult to interpret using this analytical method, however, the Pb may be increasing in concentration up-hole. Aluminum indicated in the element maps is hosted in the sphalerite and not in the quartz or pyrite. The Si concentration supports the quartz observation made in photomicrographs and the quartz abundance is clearly increasing up-hole. Chlorine increases in concentration up-hole and bedding in the U1a sphalerite is visible in the Cl map, however, the U1a zoning observed is possibly caused by X-ray continuum.....81

Figure 37. Quadrupole laser ablation element maps show the spatial distribution of trace elements in sphalerite U1a. (a) Reflected light photomicrograph show location of trace element mapping (black square). (b) Reflected light and (c) transmitted light photomicrograph of mapped area show the location of very fine acicular crystals (white square is crystal visible at the surface and is shown in Figure 41. White circle is additional crystal which is not exposed on the thin section surface). These crystals are oriented parallel to the sphalerite bedding in this sample. Cadmium, Hg, Ge, As, and Tl are mostly homogeneously distributed in the sphalerite. Iron, Cu, and Ag are only present as inclusions of additional sulfide minerals.....82

Figure 38. Quadrupole laser ablation element maps show the spatial distribution of trace elements present in U1c sphalerite. (a) Reflected light and (b) transmitted light photomicrograph showing location of (c) as well as trace element maps (white boxes). (c) Location of trace element mapping which shows sphalerite intergrown with abundant quartz. Aside from Fe, the trace element maps show a patchy spatial distribution and these elements are all present in the sphalerite and not in the quartz. Lead, Cu, Ge, As, Ag, and Tl appear to slightly increase in concentration further from the pyrite. Antimony shows an opposite trend and appears to increase toward the pyrite. Lead and Tl are higher in the pyrite nodule (lower right corner). I think I say abundance instead of concentration in the results.....84

Figure 39. Quadrupole laser ablation trace element maps show the spatial distribution of lithophile elements in sphalerite U1a. The maps have been overlaid on reflected light photomicrographs to investigate the presence of lithophile elements relative to surface features. Sodium and Rb are more concentrated in the lower sphalerite U1a, whereas Sr occurs across the map area. Silicon, Rb, Al, and Sr are highly concentrated in the opaque material which is host to acicular crystals. Silicon, Rb, Sr, and Ca are associated with the nodular pyrite.....86

Figure 40. Quadrupole laser ablation trace element maps show the spatial distribution of lithophile elements in sphalerite U1c. The maps have been overlaid on reflected light photomicrographs to investigate the presence of lithophile elements relative to the pattern of sphalerite and quartz. Sodium, Rb, and Sr are all present throughout the sphalerite. Aluminum is present in some areas of the sphalerite and sometimes correlates with Rb. Strontium and Ca show some correlation and are both present in the pyrite.....87

Figure 41. Field emission SE image and X-ray elemental maps of acicular mineral present in the opaque material of sphalerite U1a. The elemental maps indicate that the mineral is composed of Al, Si, and K with lesser amounts of Mg. Rubidium and Sr were not detected using this analytical technique. Chlorine is not present in the crystal of interest, however, is seen heterogeneously distributed in the U1a sphalerite.....88

1 Introduction

Sedimentary basins host some of the largest resources of base metals on Earth. The genesis of sedimentary hosted Pb-Zn deposits and the relationship of mineralization to basin evolution has long been a topic of debate (Johnston, 1999; Leach et al., 2001; Bradley and Leach, 2003; Bradley et al., 2004; Leach et al., 2010). In particular, researchers have debated whether sedimentary hosted deposits are the result of extensional tectonics during basin formation (syn-sedimentary models), or if they formed in the basin during later compression and are epigenetic (Leach et al., 2001; Bradley and Leach, 2003). The latter model was proposed to explain the relationship between Mississippi Valley-type (MVT) deposits and orogenic ages derived from paleomagnetic data (Leach et al., 2001; Bradley and Leach, 2003) but other workers have suggested these ages relate to fluid flow events in the basin that are unrelated to mineralization (Kesler and Carrigan, 2002; Kesler et al., 2004). This uncertainty about the genesis of the deposits is compounded as they rarely have minerals that can be directly dated by geochronological methods. As a result there has been interest in developing geochronological techniques that can directly date the ore mineral, sphalerite. Thus far, the Rb-Sr method is the only technique that may achieve this, and dating sphalerite with this technique is the focus of this thesis.

1.1 Sphalerite

Although multiple polymorphs of ZnS exist, Zn produced from mining sedimentary hosted deposits is primarily hosted in sphalerite. The structure of sphalerite (originally called zincblende) was first identified to be cubic with alternating lattice layers composed of either Zn or S atoms (Bragg, 1913) in a face-centered cubic lattice (Bragg, 1914). Wurtzite is a polymorph of cubic sphalerite where half of the tetrahedral layers have been rotated giving the lattice a hexagonal symmetry (Makovichy, 2006). Although wurtzite is thought to be a high temperature, low pressure polymorph, the exact temperature of phase transition is poorly constrained (Craig and Scott, 1974; Fleet, 2006) and the presence of trace metals can impact the wurtzite stability (Scott and Barnes, 1972). These ZnS polymorphs and their complexities have been studied in great detail and over 60 structural variations have been documented (Makovichy, 2006).

In addition to its structural variability, sphalerite can host a wide range in trace elements, some of which are sometimes in solid solution in the mineral (Fe, Cd, Mn, Co, Se, Cu, In, and possibly Sn, Ag, Ga, and Ge) while others may be present as mineral inclusions (Pb, Tl, As, Sb, and Bi) (e.g. Johan, 1988; Di Benedetto et al., 2005; Cook et al., 2009; Ye et al., 2011). The trace elements present in sphalerite are often distinct to the deposit type in which they formed (Ofstedahl, 1940; Cook et al., 2009) and are controlled by several factors including fluctuations in the source of the metals, the temperature of the fluids, the geological environment, as well as lattice-scale controls (Cook et al., 2013).

1.1.1 Sphalerite Rb-Sr Dating and Methodology

The deportment of chalcophile elements in sphalerite has been the focus of previous studies. There has been limited work carried out on the occurrence and distribution of alkali and alkaline earth metals within sphalerite. This topic is of importance because, since the pioneering work of Nakai et al., (1990), sphalerite has been widely utilized as a Rb-Sr geochronometer in sedimentary hosted deposits. The ^{87}Rb isotope decays to the ^{87}Sr isotope with a half-life of 48.8 billion years, making it suitable for dating ore deposits of all ages. The potential use of the Rb-Sr system for dating sphalerites was first suggested by Medford et al., (1983), who documented sphalerite with an Rb/Sr ratio suitable for radiogenic dating. The method was first applied by Nakai et al., (1990) on sphalerite from the Coy Mine, East Tennessee. Following the initial work of Nakai et al., (1990), several additional MVT deposits were dated using the Rb-Sr sphalerite method (Table 1; Brannon et al., 1992; Nakai et al., 1993; Christensen et al., 1995a, 1995b). The initial technique involved the dissolution of multiple grains of sphalerite in preparation for thermal ion mass spectrometer (TIMS) analyses (Nakai et al., 1990). Subsequent workers have pointed out various issues with this approach, including the fact that bulk sampling and dissolution of the sphalerite via a crush-leach approach will include in the analysis any protogenetic high Rb/Sr silicate inclusions. Nakai et al., (1993) later noted that the crush-leach method did not achieve complete separation of the fluid inclusions from the sphalerite and a very small amount of unopened inclusions can significantly impact the sphalerite analyses (Pettke and Diamond, 1996; Saintilan et al., 2015). In samples without a significant spread in $^{87}\text{Rb}/^{86}\text{Sr}$, early isochrons were defined by combining data from leached fluid inclusions and sphalerite residues (Table 1; Brannon et al., 1992; Nakai et al., 1993) to yield an age. These dates would

not be accurate if fluid inclusions were not syngenetic with the sphalerite and did not re-equilibrate when the sphalerite formed. Also, multiple generations of inclusions exist and further complicate geochronological approaches using bulk methods (Pettke and Diamond, 1995, 1996; Christensen et al., 1996).

Table 1. Compilation of deposits which have been dated using Rb-Sr on sphalerite

Deposit/District	Region	Deposit Type	Age of Host Rock	Rb-Sr Sphalerite			Additional Mineralization Age Determinations	
				Age	⁸⁷ Sr/ ⁸⁶ Sr Initial	MSWD	Paleomagnetic	Other Radiogenic
East Tennessee	Southern App. USA	MVT	Ordovician	377 ± 29 Ma Coy mine (Nakai et al., 1990); 347 ± 20 Ma Immel mine (Nakai et al., 1993)	0.7107 ± 3; 0.7103 ± 3	62.6; 192	314 ± 6 Ma (Symons and Stratakos, 2000)	272-303 Ma (K-Ar clay; Elliot and Aronson, 1987); 278 - 322 Ma (Ar-Ar K-spar; Hearn et al., 1987)
Pine Point	Western Canada	MVT	Middle Devonian	361 ± 13 Ma (Nakai et al., 1993); 374 ± 21 Ma (Brannon et al., 1995)	0.7087 ± 8	116	Permian (Beales and Jackson, 1982); 84-58 Ma (Symons et al., 1993)	
Polaris	Canadian Arctic	MVT	Ordovician	366 ± 15 Ma (Christensen et al., 1995a)	0.7086 ± 1	7.6	Late Devonian (Symons and Sangster, 1992)	374 ± 9 Ma (Re-Os bitumen; Selby et al., 2005)
Upper Mississippi Valley	Central US	MVT	Middle Devonian	270 ± 4 Ma C Horizon; 269 ± 6 Ma B Horizon (Brannon et al., 1992)	0.70932 ± 2; 0.70935 ± 2	1.33; 1.18		
Lennard Shelf	Australia	MVT	Late Devonian	358 ± 8 Ma for residues only* (Christensen et al., 1995b)	0.7127 ± 2	7.3		350 ± 15 Ma (Cement stratigraphy; McManus and Wallace, 1992) 351 ± 15 Ma (Calcite U-Pb; Brannon et al., 1996b) 325 ± 25 Ma (Stratigraphic constraints; Tompkins et al., 1994)
Silesia	Poland	MVT	Devonian to Jurassic	135 ± 4 Ma (Heijlen et al., 2003)	0.7088 ± 0.0002	3.3	Tertiary (Symons et al., 1995)	
Central African Copperbelt	DR Congo	Carbonate hosted	Neo-proterozoic	451.1 ± 6.0 Ma (Schneider et al., 2007a)	0.70897 ± 0.00002	1.4		450.5 ± 3.4 Ma (Renierite/bornite Re-Os; Schneider et al., 2007)
Sichuan–Yunnan–Guizhou (SYG) Province	China		Late Ediacaran to Permian	191.9 ± 6.9 Ma (Zhou et al., 2013) Single grain	0.7124, uncertainty unknown	0.39		228 ± 16 Ma and 225 ± 9.9 Ma (Sm–Nd hydrothermal calcite; Li et al., 2007);
Jura Mountains	Switzerland	Carbonate and Marl hosted	Mid Jurassic	162.0 ± 4.1 Ma Marl hosted group (Efimenko et al., 2013)	0.7088 ± 0.0001	1.3		183 ± 4 Ma (K-Ar clay minerals; Schaltegger et al., 1995)
Northern Eifel	Germany	Sandstone hosted	Devonian to Triassic	168 ± 6 Ma (Schneider et al., 1999)	0.71101 ± 8	1.21		
Laisvall	Sweden	Sandstone hosted	Ediacarin - Cambrian	467 ± 5 Ma (Saintilan et al., 2015)	0.715900 ± 0.000060	1.4		
Irish-type	Ireland	Irish-type	Carboniferous	360 ± 5.2 Ma Silvermines (Schneider et al., 2007b)	0.70794 ± 0.00003	2.2	269 ± 4 Ma Silvermines (Symons et al., 2007) 277 ± 7 Ma Lisheen (Pannalal et al., 2008a) 290 ± 9 Ma Galmoy (Pannalal et al., 2008b)	346.6 ± 3 Ma Lisheen and 334.0 ± 6 Ma Silvermines (Hnatyshin et al., 2015)
Franklinian Basin	Greenland	MVT	Upper Ordovician to Lower Silurian	388 ± 4 Ma (Rosa et al., 2016)	0.70930 ± 1	1.6		
Tres Marias	Mexico	MVT	Mid-Cretaceous	29.7 ± 1.2 Ma (Ostendorf et al., 2017) Paleomixing model	0.70761 ± 0.00012	82		

1.1.2 Where is the Rb and Sr in the sphalerite?

The results of the above geochronological studies have been questioned as the dates obtained sometimes contradicted previously determined ages constrained via other geological criteria (Garven and Sverjensky, 1994; Pettke and Diamond, 1995, 1996; Symons et al., 1996; Christensen et al., 1996; Leach et al., 2002). Of the many sediment hosted deposits dated using the sphalerite Rb-Sr method on sphalerite, several have Rb-Sr ages predating the paleomagnetic age leading to vigorous debate about the meaning of the Rb-Sr ages in the literature (Table 1; Kesler and Carrigan, 2002; Leach et al., 2002; Kesler et al., 2004; Bradley et al., 2004; Wilkinson et al., 2017). The crush-leach approach relies on the assumption that the residual sphalerite contains lattice-hosted Rb and Sr. A primary issue is the lack of understanding of how, and why, Rb and Sr should be incorporated into sphalerite. The increased concentration of Rb seen in some sphalerite, relative to the fluid inclusions (Nakai et al., 1993; Christensen et al., 1995a, 1995b), may indicate that a coupled substitution involving Zn^{2+} and Rb^+ occurs. Pettke and Diamond, (1996) suggested a coupled substitution of Rb^+ and a trivalent cation with 2 Zn^{2+} cations, however, this is problematic due to the very large size of the Rb and Sr ions, relative to the Zn ion (Nakai et al., 1993; Pettke and Diamond, 1996; Christensen et al., 1996). Saintilan et al., (2015) analyzed Laisvall sphalerite using in-situ laser ablation inductively coupled mass spectrometry (LA-ICPMS) for Mn, Fe, Cu, Ga, Se, Ag, Cd, In, Sn, Sb, and Pb as well as Rb and Sr and found that a consistent correlation was not present. It has also been suggested that Rb and Sr reside in the octahedral voids of the sphalerite structure or even within defects in the structure (Nakai et al., 1993; Pettke and Diamond 1996; Saintilan et al., 2015), rather than in the lattice itself.

Some authors have suggested that rapidly precipitated colloform sphalerite textures preferentially incorporate more Rb than euhedral crystals (Christensen et al., 1995b; Brannon et al., 1996a), but these textures may also incorporate more clay particles, impacting the Rb-Sr system (Garven and Sverjensky, 1994). Many authors have discussed the potential for mineral inclusion contamination on Rb-Sr sphalerite systematics (Brannon et al., 1992; Nakai et al., 1990, 1993; Christensen et al., 1995a, 1995b; Christensen et al., 1996; Brannon et al., 1996a; Bradley et al., 2004; Saintilan et al., 2015) and sphalerite used in Rb-Sr dating has been suspected as hosting mineral inclusions (Nakai et al., 1990, 1993; Christensen et al., 1995a). Inclusions of clay minerals have even been confirmed in sphalerite using SEM imaging (Nakai et

al., 1993; Bradley et al., 2004). Saintilan et al., (2015) took the inclusion investigation one step further and added Si and P to their LA-ICPMS spot analyses. Peak profiles showed that fluorapatite inclusions were Sr rich and fluid inclusions were both Sr and Rb rich. Despite these observations, no significant correlation between Si, P, Rb & Sr was consistently observed in spot analyses of “inclusion free” samples, however, a subset of samples did show a weak positive correlation between P and Sr.

1.2 Red Dog Sphalerite

In this study, we analyze sphalerite samples from the Red Dog district, Alaska, USA (Figure 1). The mine area deposits within the district consist of Qanaiyaq, Main, Aqqaluk, and Paalaaq (Figure 1; Blevings et al., 2013). Currently, the Aqqaluk and Qanaiyaq bodies host probable reserves of 50.9 Mt averaging 15.0% Zn, 4.2% Pb, and 76.4 g/t Ag (Teck Resources Limited, 2017). These two deposits, combined with the Paalaaq deposit, host additional indicated resources of 16.4 Mt averaging 7.7% Zn, 2.7% Pb and 49.7 g/t Ag and inferred resources of 6.6 Mt averaging 12.0% Zn, 4.6% Pb and 87.2 g/t Ag. (Teck Resources Limited, 2017). These deposits will be referred to as the main Red Dog deposits hereafter.

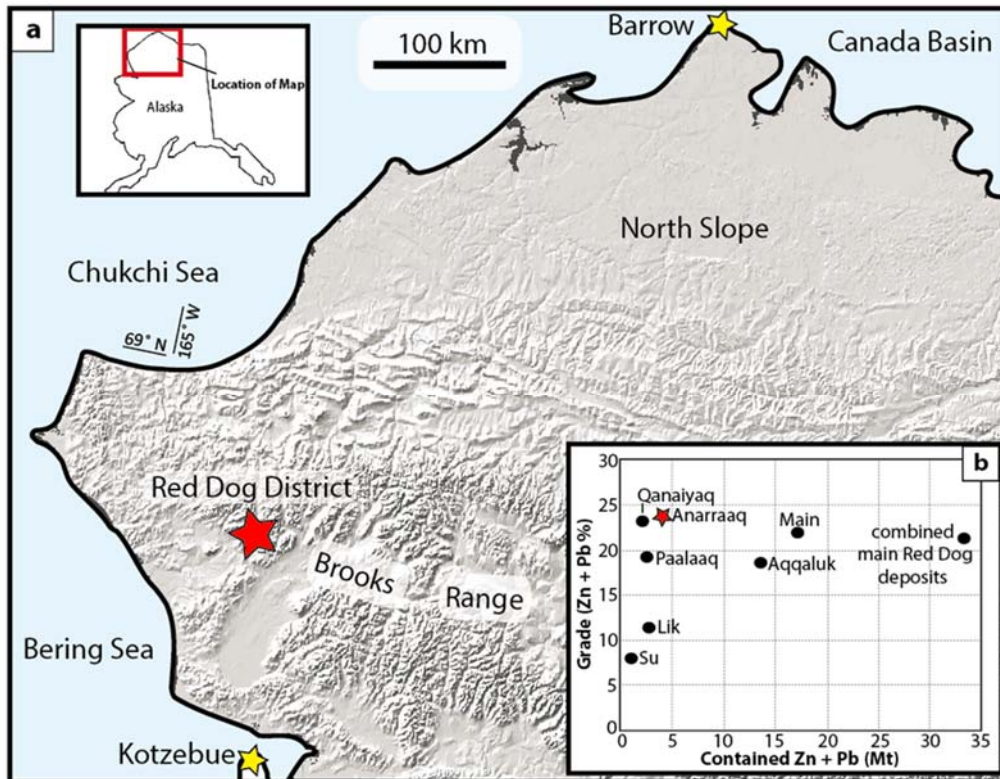


Figure 1. (a) Location map of the Red Dog District within the Brooks Range of Northern Alaska. (b) Plot of tonnage versus grade for deposits in the district. The combined main Red Dog deposits consists of Main, Paalaaq, Aqqaluk, and Qanaiyaq. Modified from Graham et al., 2009; Blevings et al., 2013; and Riehle et al., 1997.

Aside from the main Red Dog deposits, other discoveries have also been made within the Red Dog district. Discovered in 1999, Anarraaq is a Zn-Pb-Ag shale hosted massive sulfide deposit with inferred resources of 19.4 Mt containing 14.4% Zn, 4.2% Pb, and 73.4 g/t Ag (Teck Resources Limited, 2017). Anarraaq mineralization is texturally complex and although ore replacement textures are abundant, the age of mineralization overlaps the sediment age (Kelley et al., 2004b, Morelli et al., 2004; Dumoulin et al., 2004).

Modern day in-situ analytical techniques such as LA-ICPMS spot analyses allow for examining trace elements at sub-ppm concentrations. The only issue with applying spot analyses to samples which may host compositional zoning is that the data are likely to be biased towards preferentially sampled zones based on abundance or appearance in preliminary optical microscopy. The only way to truly assess the compositional zoning of sphalerite at trace concentrations, relative to previously assessed textural variation, is to use LA-ICPMS element mapping.

Here we provide detailed LA-ICPMS trace element maps of Anarraaq sphalerite which reveal complex chalcophile element spatial distributions such as Fe controlled oscillatory zoning, oscillatory zoning independent of Fe content, sector zoning, and mineral inclusions. Within these complex zones, Rb is commonly hosted in silicate mineral inclusions and Sr is mostly hosted in carbonate mineral inclusions within the sphalerite, the former having the potential to drastically compromise the accuracy of a Rb-Sr age because these inclusions cannot be separated from the sphalerite using current methods. Although the Rb and Sr distributions sometimes appear uniform, coupling the Rb maps with additional maps of chalcophile elements shows clearly that Rb cannot be involved in a coupled substitution with any of these elements as proposed by Pettke and Diamond, (1996) which agrees with the observations of Saintilan et al., (2015).

2 Geologic Background

2.1 District Geology

The Mississippian Kuna Formation is the result of deep water deposition in a restricted extensional basin (Dumoulin et al., 2004; Young, 2004). In the Red Dog area, the Kuna Formation is subdivided and the upper zone, known as the Ikalukrok unit, hosts the massive sulfide deposits (Moore et al., 1986). The Ikalukrok unit consists mostly of black shales and mudstones that contain up to 18% total organic carbon (TOC) and up to 4% phosphate (Dumoulin et al., 2004). The mudstones also host carbonate layers which are dominated by calcareous radiolarians and also contain lithic turbidites up to >4m thick (Dumoulin et al., 2004). Based on conodonts and radiolarians identified in drill core, the Ikalukrok unit is likely Meramecian to Chesterian in age (~340 Ma to 330 Ma; Dumoulin et al., 2004). Although it was persistently thought that Red Dog mineralization occurred in deep sediment within the anoxic zone of a stratified water column (Slack et al., 2004a; Slack et al., 2015), more recent findings have suggested that the mineralization actually occurred in outer shelfal sediment within a fluctuating oxygen minimum zone (Reynolds et al., 2015).

Pyrite associated with the sulfide mineralization has been dated at 338.3 ± 5.8 Ma by the Re-Os method (Morelli et al., 2004) and overlaps the age of the Ikalukrok host rock. Mineralization in the main Red Dog deposits is interpreted to be the result of a complex four stage process which includes replacement, brecciation, and vein ore textures (Kelley et al., 2004a). Despite the agreement on the timing of mineralization, the source of the metals,

transportation processes, and mechanisms for ore precipitation in this world class district are not yet understood (Kelley and Jennings, 2004). Leach et al., (2004) suggested that the mineralizing fluids which lead to the precipitation of ore-stage red-brown sphalerite at the main deposits were ultimately derived from evaporated seawater. They suggest therefore, that the mineralizing fluids were high salinity brines, potentially as high as 30 wt% saline before dilution, similar in temperature and electrolyte composition to that of MVT fluids.

Based on Pb isotopic analyses of Red Dog sulfides combined with litho-geochemical analyses, clastic sedimentary rocks of the Devonian-Mississippian Endicott Group are thought to be the source of Pb (Ayuso et al., 2004). The metalliferous brines are thought to have circulated in the underlying rocks at depths of up to >7 km before migrating, likely structurally controlled (Leach et al., 2004), into the Kuna Formation (Garven et al., 2003). Additional metals are thought to be from the same source as the Pb (Kelley et al., 2009; Slack et al., 2015).

Metal rich fluids are thought to have mixed with H₂S at the site of sulfide mineralization at temperatures <200°C (Kelley et al., 2004a; Leach et al., 2004; Schardt et al., 2008). Variability in S isotopic values may be explained by a combination of bacteriogenic sulfate reduction (BSR) at the site as well as reductive dissolution of previous barite (Johnson et al., 2004; Kelley et al., 2004a).

The Alaskan Brooks Range formed during the Mesozoic as the result of the southern Angayucham oceanic terrane colliding with the northern Arctic Alaska passive margin during the Brookian Orogeny (Mull et al., 1982; Moore et al., 1994). From the middle Jurassic to the early Cretaceous, compressional deformation affected the Red Dog region; currently the Red Dog mineralization is located within the Red Dog plate of the Endicott allochthon (Mull, 1982; Mayfield et al., 1988; Moore et al., 1994). Abundant late quartz veining is present in the deposits and is interpreted to be the result of later fluid flow during the Brookian Orogeny (Leach et al., 2004), however, it has also been suggested that large scale silicification occurred during the Mississippian (Slack et al., 2004b). Large scale post-Brookian Orogeny steeply dipping normal faults further complicate the structural framework of the district (Blevings et al., 2013).

2.2 Anarraaq Deposit

Anarraaq is hosted at depths of ~600-700 m from the surface (Blevings et al., 2013), and the mineralization occurred in sediment deposited before the water column reached euxinia (Johnson

et al., 2015). The Ikalukrok unit is significantly thicker at the Anarraaq deposit and this is likely due to an increase in the number of calcareous turbidites (Dumoulin et al., 2004). Although Zn is isotopically homogeneous in the main Red Dog deposits, the Anarraaq deposit hosts isotopically heavier Zn and this is suggested to be attributed to isotopic fractionation through the evolution of the system where Anarraaq represents more distal mineralization relative to the feeder zone at the main Red Dog deposits (Kelley et al., 2009). The source of reduced S had to be substantial in order to result in a long lived (0.3 m.y.; Schardt et al., 2008) mineralization event at Anarraaq.

An estimated 1 billion metric tons of barite overlies the sulfide deposit at Anarraaq (King et al., 2002) and the two deposits are separated by 70-100 m of the Ikalukrok unit (Kelley et al., 2004b; Figure 2). Barite is rarely present in the sulfide deposit of Anarraaq (Kelley et al., 2004b).

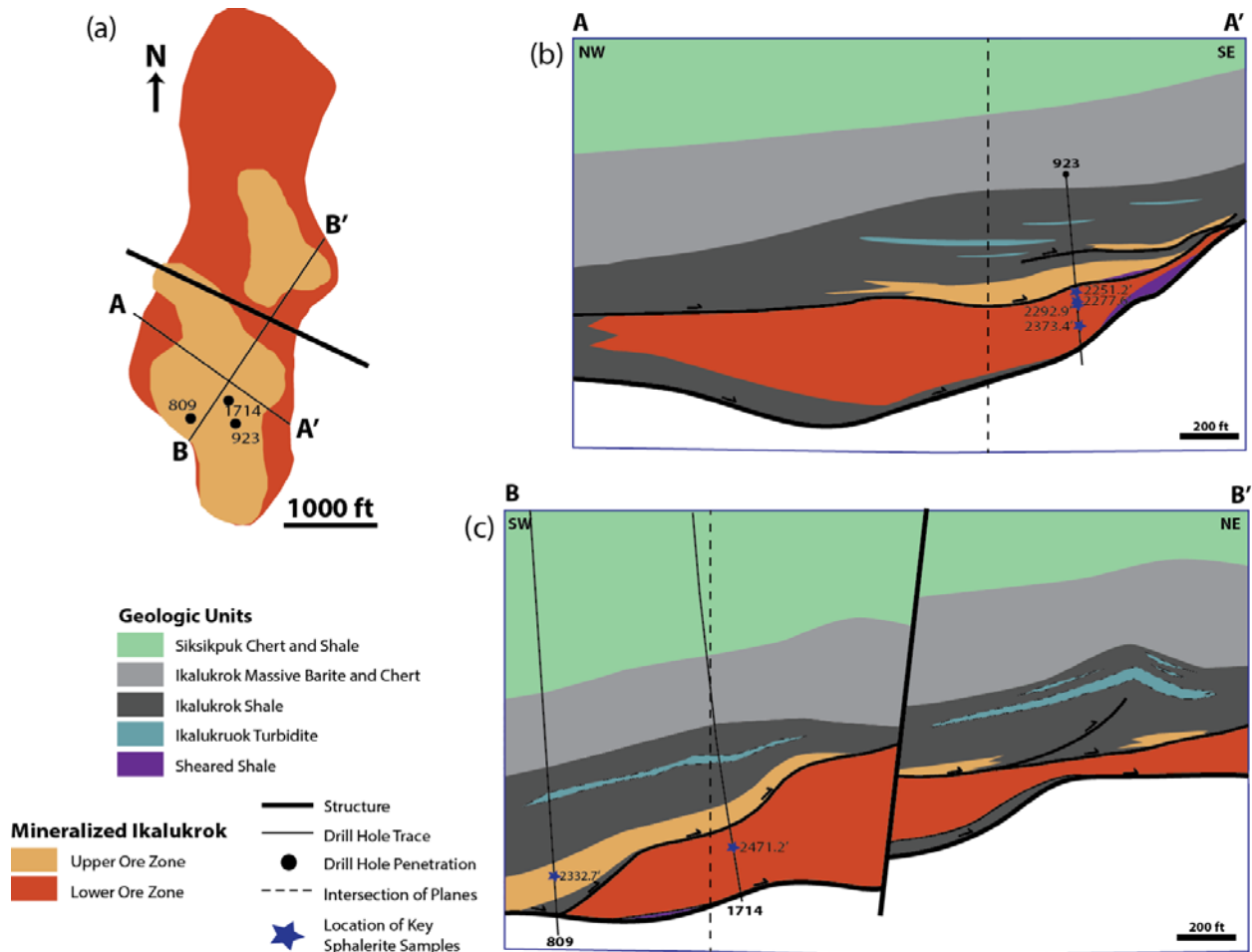


Figure 2. (a) Plan view of Anarraaq deposit at depth showing extent of upper and lower ore zones, drill hole, and cross section locations. (b) A-A' cross section showing the location of key samples within the mineralized

Ikalukrok unit. (c) B-B' long section shows the location of key samples from the Upper and Lower ore zones. Modified from M. Reynolds and Teck geologists, unpublished.

The massive ore (Lower ore zone; Figure 2) is a stratabound breccia dominated zone where coarse dark sphalerite bearing clasts (mm to cm in size) are supported in a matrix of mixed sulfides (Kelley et al., 2004b). Because later sulfides host clasts of earlier sulfides, brecciation is thought to have occurred during sulfide mineralization (Blevings et al., 2013). This zone is reported as having increased levels of Ag and Cu (Jennings and King, 2002). Evidence of open space filling is also present and voids are later filled by white carbonates or organic matter. In addition to the breccia ore, late veins are also present cutting the massive ore (Kelley et al., 2004b). The late veins range <1cm to <30 cm, cut the Ikalukrok unit, and vary in composition from sphalerite to even later crosscutting carbonate \pm pyrite \pm galena (Kelley et al., 2004b).

The banded ore (Upper ore zone; Figure 2) is a zone of laminated sphalerite, galena, and rounded iron sulfides and is located above and adjacent to the massive ore zone (Kelley et al., 2004b; Figure 2) and hosts high levels of Ge and Tl (Jennings and King, 2002). The banded sphalerite ranges from cream to tan, depending on intergrown quartz concentrations, and the laminations mimic the orientation of interlayered shale or mudstone (Kelley et al., 2004b).

The paleo-graphic relationship between mineralization at the main Red Dog deposits and Anarraaq is not known (Kelley et al., 2009). Unlike the main deposits, the Anarraaq mineralization is only constrained by a maximum age for the Ikalukrok unit (Meramecian to Chesterian; Dumoulin et al., 2004; Kelley et al., 2004b). Textural similarities are reported for the massive ore zone at Anarraaq and late stage veins within the main deposits (Kelley et al., 2004b). Despite having significant differences in accessory mineral content (carbonate in the Anarraaq massive zone; quartz and barite in the main deposit late stage veins), these zones from the different deposits are geochemically similar with comparable concentrations of Ag, Fe, and Co (Kelley et al., 2004b). (Kelley et al., 2004b) suggest the Anarraaq deposit formed by barite and sulfides replacing calcareous mass flow units.

3 Methods

The methods used in this study consist of electron probe micro analyzer (EPMA) and LA-ICPMS analyses. The EPMA was used to quantify major and minor elements in the sphalerite

and also map the spatial distributions of these elements using X-ray maps. Rubidium and Sr concentrations were below the limits of detection for the EPMA so additional analyses used LA-ICPMS mapping to first determine if Rb and Sr were even present in the sphalerite and secondly, to determine if these elements were lattice bound in sphalerite. Furthermore, other lithophile and chalcophile elements were analysed to assess if there were spatial correlations with Rb and Sr, which may help to identify potential mineral inclusions or coupled substitutions in the sphalerite. A detailed account of the procedures and operating conditions for these analyses follows.

3.1 EPMA

Three different EPMA instruments were used to quantify and describe the variability and distribution in major and minor element composition of Anarraaq sphalerite.

3.1.1 JEOL JXA-8900 Superprobe – University of Alberta

Wavelength dispersive spectrometry (WDS) using the JEOL JXA-8900 electron microprobe, housed at the University of Alberta, was conducted to quantify major and minor element compositions of sphalerite. A total of 13 elements were chosen for these analyses and consist mostly of chalcophile elements (Table 2). In total, 334 spots were analyzed and 22 points were removed from the data set due to total wt% values <99 or >101. The spots were set as traverses across the sphalerite samples by selecting a start and stop location as well as the number of points within the traverse. An electron beam diameter of 2 μm was used for all analyses. For the unknown analyses, an accelerating voltage of 20 kV and an electron beam current of 100 nA was used. A count time of 30s was used for major elements (Zn, S, Fe), 60s for minor elements (Pb, Sb, Ag, As, Cu, Se, Sn, Mn) and 90s for Hg and Cd. Standards were analyzed using 20s count times and electron beam currents included 30 nA (for Zn, S, Sb, Ag, Hg, Se, Sn, and Mn), 50 nA (Cu, Cd), and 100 nA (Pb, Fe, and As).

Table 2. List of standards and specifications used for JEOL analyses

Element	Standard	X-ray	Crystal	LOD* (Wt%)
Zn	Sphalerite	L α	TAP	0.033
S	Iron disulfide	K α	PET	0.054
Cd	Cadmium	L β	PET	0.042
Fe	Iron disulfide	K α	LIFH	0.123
Pb	Galena	M α	PETH	0.008
Sb	Antimony	L α	PET	0.018
Cu	Copper	K α	LIFH	0.009
Sn	Herzenbergite	L α	PETH	0.012
Hg	Cinnabar	M α	PETH	0.025
As	GaAs	L α	TAP	0.040
Se	GaSe	L α	TAP	0.021
Ag	Silver	L α	PET	0.031
Mn	Manganese	K α	LIFH	0.008

* LOD - Limit of determination calculated as 2x the detection limit.

A ZAF correction was applied which assumes a linear relation between concentration and X-ray intensity. Following analyses, minimum detection limits were calculated using background counts of the unknowns, net peak counts of the standards, and the concentration of the standard following that of Potts, (1992). The net peak counts of the standards were normalized to the count times and beam current used on the unknown analyses. The lower limit of determination is the point at which the peak signal becomes quantitative above the background signal (Potts, 1992) and was calculated as twice the magnitude of the minimum detection limit (Table 2).

Initial Zn, S, Fe, Cd, and Pb X-ray elemental maps of sample 923-2277.6a were also produced on the JXA-8900 to map the spatial distribution in major and minor elements and, more specifically, investigate the spatial occurrence of any Pb present in the sphalerite. Lead concentrations were a concern because of possible Pb contamination of the LA-ICPMS introduction system, which is used for highly precise U-Th-Pb isotopic analyses. Imaging using the back-scattered electron (BSE) detector was also used to aid in identifying Pb within the sphalerite. The X-ray maps were produced using 20kV accelerating voltage, 100nA beam current, a resolution of 1 $\mu\text{m}/\text{pixel}$, and a 20ms dwell time. The JEOL JXA-8900 quantitative dataset is available in Appendix A. Additionally, the JEOL JXA-8900 images and X-ray element maps are provided in Appendix B.

3.1.2 CAMECA SX100 – University of Alberta

Additional WDS analyses using the CAMECA SX100 electron microprobe, also housed at the University of Alberta, were conducted to quantify lithophile element compositions within the Anarraaq sphalerite as a proxy for potential inclusions of clay minerals or remnant host rock. Additional elements were added to the analyses to investigate the correlation between lithophile and chalcophile elements. Data obtained from elements which were identified on both instruments have been combined for data analyses using ioGAS v6.0.1.

A total of 18 elements were chosen and standards used for analyses are provided (Table 3). The 18 elements which were chosen for these analyses include 9 lithophile elements, 8 chalcophile, as well as Fe (Table 3). Potential interference were identified between Zn-Na, Pb-S, and Sn-Sb so these were corrected by measuring a pyrite standard for Pb, Sn on Sb standard, and Na on a sphalerite standard and subtracting these from the unknown analyses. A ZAF correction was also applied. In total, 204 points were analyzed and 15 points were removed due to inaccurate totals (total wt%). Analytical points were set by using traverses of multiple points across the sphalerite samples. This is done by choosing a start and stop location for the traverse and then selecting the desired spacing between each point. Each of the individual points was carefully checked once the traverse was set. An electron beam diameter of 2 μm was also used for these analyses. An accelerating voltage of 20 kV and an electron beam current of 20 nA for major elements (Zn, S, Fe, Cd) and 200 nA for minor elements (Cl, Si, Sb, Cu, Na, K, Pb, Sn, Hg, Al, Ba, Sr, Ca) was used. A count time of 30s was used for major elements, 60s for minor elements, and 120s for Rb. Standards were analyzed using 30s count times and 20nA beam current. The CAMECA SX100 quantitative dataset is available in Appendix A.

Table 3. List of standards and specifications used for CAMECA analyses

Element	Standard	X-ray	Crystal	LOD* (Wt%)
Zn	Sphalerite	K α	LLIF	0.047
S	Sphalerite	K α	PET	0.040
Cd	Cadmium	L α	LPET	0.062
Fe	Iron disulfide	K α	LLIF	0.024
Pb	Galena	M α	LPET	0.032
Sb	Antimony	L α	PET	0.019
Cu	Copper	K α	LLIF	0.008
Sn	Cassiterite	L α	PET	0.019
Hg	Cinnabar	L α	LLIF	0.050
Rb	RbTiOPO4	L α	LTAP	0.009
Sr	SrTiO3	L α	LPET	0.020
K	Sanidine	K α	PET	0.006
Al	Albite	K α	LTAP	0.005
Cl	Tugtupite	K α	PET	0.009
Na	Tugtupite	K α	LTAP	0.055
Si	Diopside	K α	LPET	0.006
Ca	Diopside	K α	PET	0.006
Ba	Sanbornite	L α	PET	0.020

* LOD - Limit of determination calculated as 2x the detection limit.

Potassium was apparently detected in 186 CAMECA analyses, however, following analyses, a peak overlap was found to exist between K and Cd and the data exhibited a very strong positive K-Cd correlation. Because of this, the K data is not reliable in the samples analysed.

Imaging using the BSE detector was also used to aid in identifying mineral inclusions within the sphalerite as well as careful selection of spot analyses locations. Extreme caution was used to avoid visible galena and pyrite while setting points for spot analyses. Secondary electron (SE) images were collected following the analyses to confirm the exact location of the CAMECA spot analyses as well as the previous JEOL analyses. However, this could not be completed for sample 923-2251.2a because it was polished for use in a separate study.

Additional X-ray element maps of Zn, Si, Al, Cl, and K were completed on sample 923-2277.6a. Elemental maps of Zn, S, Fe, Cd, Pb, Si, Al, Cl, and K were completed on additional areas of interest in the remaining key samples. Element mapping was completed using an acceleration voltage of 20 kV, a beam current of 100nA, a 1 μ m/pixel resolution, and a 20ms

dwel time. Because of a peak overlap between Zn and Na, Na could not be mapped using this method. The previously discover peak overlap between Cd and K was avoided by analyzing K on the $K\beta$ peak position. The CAMECA SX100 images and X-ray element maps are provided in Appendix C.

3.1.3 JEOL JXA-8500F Hyperprobe – GFZ, Potsdam, Germany

Additional X-ray element maps were conducted with the WDS equipped on the JEOL Hyperprobe JXA-8500F housed at the GFZ German Research Center, Potsdam. A beam current of 40nA was used in conjunction with a 15kV and 200ms dwell time. Compared with the previous mapping on the CAMECA SX100, these analyses were performed under a much lower beam current, lower accelerating voltage, a significantly longer dwell time (200nA, 20kV, 20ms previously), and at a smaller scale. This was done as an attempt to identify potential Rb and Sr bearing inclusions which could have been missed in the previous analyses. The stage scans ranged from 100 – 340 μm in size and were completed at a 1 μm /pixel resolution. In addition, a single beam scan was completed on an area 9x11 μm at 256x256 pixels allowing for a spot size of 35 nm. Opposed to stage scanning with a fixed beam position, beam scanning utilizes a fixed stage while the beam rasters across the sample surface. This technique causes the beam to become defocused toward the outer edges of the mapped region, therefore, maps produced using beam scan mapping must be interpreted with caution.

Following the initial mapping, elemental distributions which were observed in the maps were investigated in detail using energy dispersive spectrometry (EDS) spot analyses, spectrometer scans, and WDS spot analyses. This investigation proved difficult due to the size of the inclusions (<10 μm) and no quantitative data was produced.

3.2 LA-ICPMS

Following reconnaissance quantitative EPMA and qualitative X-ray element mapping, LA-ICPMS was used to determine the presence of Rb and Sr in sphalerite and investigate the spatial distribution of these elements, if present, relative to additional elements. The additional elements were added to resolve the actual host of Rb and Sr in the sphalerite.

3.2.1 Thermo Element XR2 – University of Alberta

Initial LA-ICPMS element mapping was conducted to investigate if Rb and Sr were present in the sphalerite in trace concentrations below the EPMA limit of determination. Five out of 9 experiments on sample 923-2277.6a were successful using ^{85}Rb , ^{88}Sr , ^{29}Si , ^{27}Al , and ^{57}Fe . Mapping was conducted using a Thermo Element XR2 LA-ICPMS housed in the Arctic Resources Laboratory at the University of Alberta. The mass spectrometer is equipped with a magnetic sector mass analyzer which is much more sensitive than a quadrupole analyzer, however, the scan speed of the sector field analyzer is much slower and therefore only a narrow mass range can be mapped. The mass spectrum is scanned electrostatically using a constant magnetic field and the mass range must stay within 30% of the magnetic position. If a narrow mass range is analyzed, total sweep times are comparable to that of a quadrupole analyzer. The increased sensitivity of the sector field make it ideal for trace element mapping. The mass spectrometer is coupled with a Resonetics M-50 LR laser system which is operated with Geostar software.

The 30 μm thin section was cleaned using acetone and blown off with N_2 gas and then placed in a stage alongside reference material epoxy mounts. Once the sample and reference material were securely mounted, the stage was scanned on an Epson flatbed and the resulting image was loaded in Geostar. Three points of reference located on the sample stage were matched with the scanned image syncing the coordinates between the sample cell and the stage image. The stage was then inserted into a Larentechnic Australia ablation cell. Following insertion, the cell was pressurised and subsequently purged with He 3x before being held at a steady He pressure. The squid (signal attenuation device) was removed in order to deliver sample aerosol (carried in an Ar stream) directly to the plasma as a transient signal. Prior to mapping, the instrument was calibrated by rastering a 33 μm long scan across reference material NIST612. This was completed each morning before beginning analyses to ensure low oxide formation, low doubly charged ion counts, and ideal sensitivity.

Operating conditions including spot size, scan speed, repetition rate, laser energy, dwell time and washout time, were selected and tested following that of Ubide et al., (2015) and George et al., (2015). A mask was applied to alter the laser aperture and ablate the sample with a square laser beam. Spacing between laser lines was set at the same diameter as the beam. A repetition rate of 10 Hz (10 pulses/second), a dwell time of 10 ms for each element, an initial

time of 40s and washout time of 40s were used for all of the preliminary mapping. Reference material NIST 610 (primary) and BCR-2G (secondary check) were initially selected and BCR-2G was later replaced by GSE-1 (as primary) because of a low Fe concentration in NIST 610 and low Rb concentration in BCR-2G. Identical rasters were completed on reference material before and after each map experiment.

Data reduction was completed using Iolite v3.32. The mass spectrometer data was imported into Iolite and then coupled with a laser log file which tracks the coordinates of the laser as it scans through the map region. Baseline, reference material, and output (sample data) integrations were applied and the linear fit between the standard runs was checked. 'Trace Elements_IS' was selected as a data reduction scheme and was ran using NIST 610 or GSE-1 as standard reference material and Fe as an internal standard, however, the maps were reproduced a semi-quantitative because of the variability in Fe across the individual map areas.

Following data reduction, images from the selection were created in Iolite. These images are very limited, therefore CellSpace images were created using the Epson scan of the stage which was exported from Geostar as a MAPPED image and .coord file. The map areas were first overlaid on the stage scan and then the coordinates of the maps were determined. CellSpace was then closed and the images were created again by manually entering the coordinates of the area. The semi-quantitative Thermo Element XR2 CellSpace images are available in Appendix E.

3.2.2 Thermo iCapQc – University of Alberta

Following the confirmation that Rb and Sr are present in low concentrations, additional LA-ICPMS mapping was completed to determine the spatial correlation of the Rb and Sr relative to additional lithophile as well as chalcophile elements. Four experiments were ran on sphalerite in samples 923-2277.6a, 923-2373.4a, and 809-2332.7a. The suite of elements mapped consisted of ^{23}Na , ^{27}Al , ^{29}Si , ^{31}P , ^{35}Cl , ^{39}K , ^{44}Ca , ^{55}Mn , ^{57}Fe , ^{59}Co , ^{61}Ni , ^{63}Cu , ^{71}Ga , ^{73}Ge , ^{75}As , ^{77}Se , ^{85}Rb , ^{88}Sr , ^{95}Mo , ^{107}Ag , ^{111}Cd , ^{115}In , ^{118}Sn , ^{121}Sb , ^{137}Ba , ^{202}Hg , ^{205}Tl , and ^{208}Pb , following that of George et al., (2015), with lithophile elements added in addition.

Mapping was conducted using a Thermo iCapQc at the University of Alberta. The mass spectrometer is equipped with a quadrupole mass analyzer making it ideal for mapping of a large suite of elements with a wide mass range. The mass spectrometer is coupled with a New Wave UP-213 laser ablation system. Ablation was completed in a He atmosphere cell and then

transported as an aerosol in a He carrier gas with a flow rate of 1 L/min. The aerosol/He carrier stream is then mixed with Ar gas at a flow rate of 1 L/min before being introduced to the plasma torch.

Prior to mapping, the instrument was tuned for sensitivity, molecular oxide production, and doubly charged ions by rastering across standard reference material NIST612 glass. This was completed each morning before attempting analyses.

Several laser and software limitations were encountered during these analyses. After setting 2 consecutive lines to raster, the software continually froze after the first line and the second line could not be initiated. Because of this issue, a line of 26 (12 μm in diameter) individual spots was created and the spots were spaced 8 μm apart to produce some overlap between the spots and simulate a raster line. The line of spots was then copied and pasted several times until 26 rows were present. Because the software displays a fixed spot size on the computer monitor, the true beam size and spacing between the rows was difficult to determine. A line of spots was first made on the reference material and then determined to be slightly larger than those evident on the digital display (at 12 μm in diameter). Some overlap between the lines is desirable so the lines were carefully positioned adjacent to each other. The lines were also carefully positioned so that offset between lines is minimal, however, some offset is unavoidable.

A laser repetition rate of 10 Hz (10 pulses/second) was used and 50% energy was set to produce $\sim 4.00 \text{ J/cm}^2$ fluence or energy density at the target. A laser dwell time for each spot of 1s, and a mass dwell time of 30 ms for each element was used. A warmup time of 30s and a delay of 5s were used bringing the run time to 61s per line, however, it was observed that the peak signal was being abruptly truncated so the duration was extended to 71s per line for the sample analyses and 61s for the reference materials.

Pressed pellet standard reference material MASS-1 was used for chalcophile/siderophile elements and glass standard reference material GSE-1 was used for lithophile elements. Two identical lines of spots were completed on both reference materials before and after session sample analyses. The New Wave UP-213 laser ablation system can only hold one thin section and one standard reference material at a time. Because of the need for an additional standard, GSE-1 was analyzed first and then the sample was placed in the cell with MASS-1. To reduce analyses time, the line which feeds the sample aerosol in a He stream to the plasma torch was disconnected and then reconnected following the sample switch. This must be done quickly to

avoid an introduction of atmospheric air to reach and extinguish the torch which happened on the final GSE-1 switch. For future analyses, parafilm should be placed over the line to prevent this.

Data reduction was completed using Iolite v3. The mass spectrometer data was imported into Iolite but could not be coupled with a laser log file because this laser system does not produce one. Baseline, reference material, and output (sample data) integrations were applied and the linear fit between the standard runs was checked. GSE-1 showed slightly higher baseline signal counts for the first run and even higher counts for the final run. This is potentially caused by disconnecting the aerosol line, however, GSE-1 was ran first and last so if the increased baseline was caused by the sample switch, an increase would be observed in the MASS-1 analyses immediately following the first switch. Regardless, if this method is used for future analyses, a longer wait period should be applied to stabilize the system. 'Trace Elements_IS' was selected as a data reduction scheme and was ran separately for GSE-1 (lithophile maps) and MASS-1 (chalcophile/siderophile maps), however, a standard reference material for Cl is not available and Cl is difficult to ionize in the plasma torch. A Fe concentration of 5% was used as an internal standard.

Following data reduction, images from the selection were created in Iolite and these images are available in Appendix F. Because the images from selection builds the maps using the mass spectrometer data vs. time, and a laser log file is not available, any spacing issues with using the manually placed repetition of spots will not be revealed in the maps themselves. If there is any offset, Iolite will not recognize this and it will produce perfectly equidimensional maps every time. Following ablation, the area was examined and the spacing set in the software was not accurate. Despite the careful placement of the lines, some gaps between the lines were visible. Furthermore, variability in the sample topography was noted. This is caused by having to use the individual spots rather than a smooth scan. A square aperture is not available on this laser system so spots must be overlapped to prevent even further gaps in the grid. The area that is overlapped receives 2x the ablation and is therefore ablated twice as deep creating a repetitive crescent shape bore into the sample surface. This causes issues with sampling potentially coming from two separate horizons of material and due to the heterogeneity that has already been determined in this material, this is a huge concern. Additionally, the resulting unevenness in the sample surface rendered the area off limits for future mapping.

The issue with the inability to complete line scans using the laser software was resolved and additional areas were mapped using individual line scans compiled into a single mapped image. These additional maps were ran using the same operating conditions described above. The spacing between each line still had to be manually estimated and following analyses, offset between the individually placed lines was visible.

3.2.3 Thermo iCapQs – Trinity College, Dublin, Ireland

Following the previous unsuccessful attempts at mapping additional elements, final element mapping was completed using a Thermo Elemental iCapQs housed at Trinity College, Dublin. The mapping included ^{57}Fe , ^{63}Cu , ^{67}Zn , ^{73}Ge , ^{75}As , ^{107}Ag , ^{111}Cd , ^{121}Sb , ^{202}Hg , ^{205}Tl , and ^{208}Pb as a chalcophile element suite and ^{23}Na , ^{27}Al , ^{29}Si , ^{43}Ca , ^{57}Fe , ^{85}Rb , and ^{88}Sr were mapped secondary as a lithophile element suite. Initially, ^{66}Zn was used and then switched to ^{67}Zn which has a lower abundance, however, Zn was still difficult to map due to the very high counts. Iron was also added to the lithophile scan to compare with Fe mapped during the chalcophile run. The lithophile suite was ran secondary as an attempt to remove any potential lithophile element contamination on the sample surface.

The iCapQs was coupled with a Teledyne Photonmachines G2 193 mm excimer ArF laser operated using Chromium 2 software and a HelEx II 2-volume cell. The aerosol delivery system was modified with a Teledyne Cetar aerosol rapid induction system (ARIS) which allows for rapid delivery of the sample aerosol to the plasma torch. This modification involves a thinner, shorter peek tube as well as ultra-pure N injected into the aerosol just before the plasma torch which allows for a much faster washout, increased sensitivity, and improved map spatial resolution. These improvements also allow for extremely fast line scan speeds which preserves sample material and provides the user with the ability to run multiple map experiments of the same area.

Tuning was completed each morning on NIST612 glass to ensure instrument sensitivity, minimal molecular oxide production, and minimal doubly charged ions present. This was done by completing line scans across the NIST612 standard reference material.

A total of 15 sample areas were mapped and areas averaged $\sim 400 \times 400 \mu\text{m}$ in size. For chalcophile maps, a $5 \mu\text{m}$ square spot size was used with a scan speed of $40 \mu\text{m/s}$. All maps were obtained with a very low laser fluence of 1.0 J/cm^2 and an increased repetition rate of 50 Hz.

After initial mapping of lithophile elements proved challenging, the spot size was increased to a 20 µm square aperture which was scanned at 10 µm/s. All elements were set at a mass dwell time of 20ms with the exception of Rb and Sr which were increased to 40ms when the spot size was also adjusted. This was done to improve detection of Rb and Sr. A washout of 10s was inserted between each of the individual line scans and >30s of background was also captured at the beginning and the end of each element run.

Following initial mapping of the 15 areas, two large areas (~900x8000 µm) were selected to map the distribution of chalcophile elements across multiple stages and textures of sphalerite. This was done with a 20 µm square aperture scanned at 80 µm/s. An initial pause of 10s was used and then changed to 20s because of an issue with Hg washout. The chalcophile element suite for these areas was modified slightly by switching ²⁰⁵Tl for ¹¹⁵In.

Data reduction was initially completed in Iolite v2.5 and key areas were later reduced again in v3.32 which has added CellSpace features (allows for the use of a log scale as well as square image pixel if a square laser aperture was used). In order for the software to recognize the square aperture, the laser log file must be manually edited so that 'wheel' is changed to 'still' and the spot size is changed from '5' to '5x5'. The baselines were selected at the beginning and end of every run as well as the 10-20s pause in between individual line scans. These baselines were subtracted and the data was reduced using the 'Trace Elements' data reduction scheme in semi quantitative mode. Once the data was reduced, the map images were produced in CellSpace using a cell stage scan image (captured in Chromium 2) as the mapped image to overlay the map on. The semi-quantitative Thermo iCapQs CellSpace images are available in Appendix F.

The CellSpace images are produced by an interpolation using the coordinates in the laser log file. The software creates a spot for each location and divides each spot into a series of pixels which are assigned values (Iolite 3 User's Manual, 2015). The number of spots per second is a factor of the laser pulse rate and the total sweep time of the mass spectrometer. The amount of pixels within each spot is determined by the resolution of mapped image that was created by the laser software. Overlapping pixels between the spots are averaged with a slight bias toward the later spots and this creates a smoothing effect in the image. Because of this smoothing effect, inclusions which are smaller than a couple of spots may be completely smoothed out. The lack of complete correlation between inclusions bearing Rb with additional elements such as Si and Al in this study could be due to the CellSpace smoothing effect.

When the CellSpace image is produced, Iolite assigns an initial lower and upper limit. These limits rarely capture the range where the majority of the data reside, and therefore the limits must be manually adjusted. By lowering the upper limit, some features become apparent in the images (Figure 3a-c). Using a log scale is also sometimes helpful in illustrating areas which were previously not visible (Figure 3d).

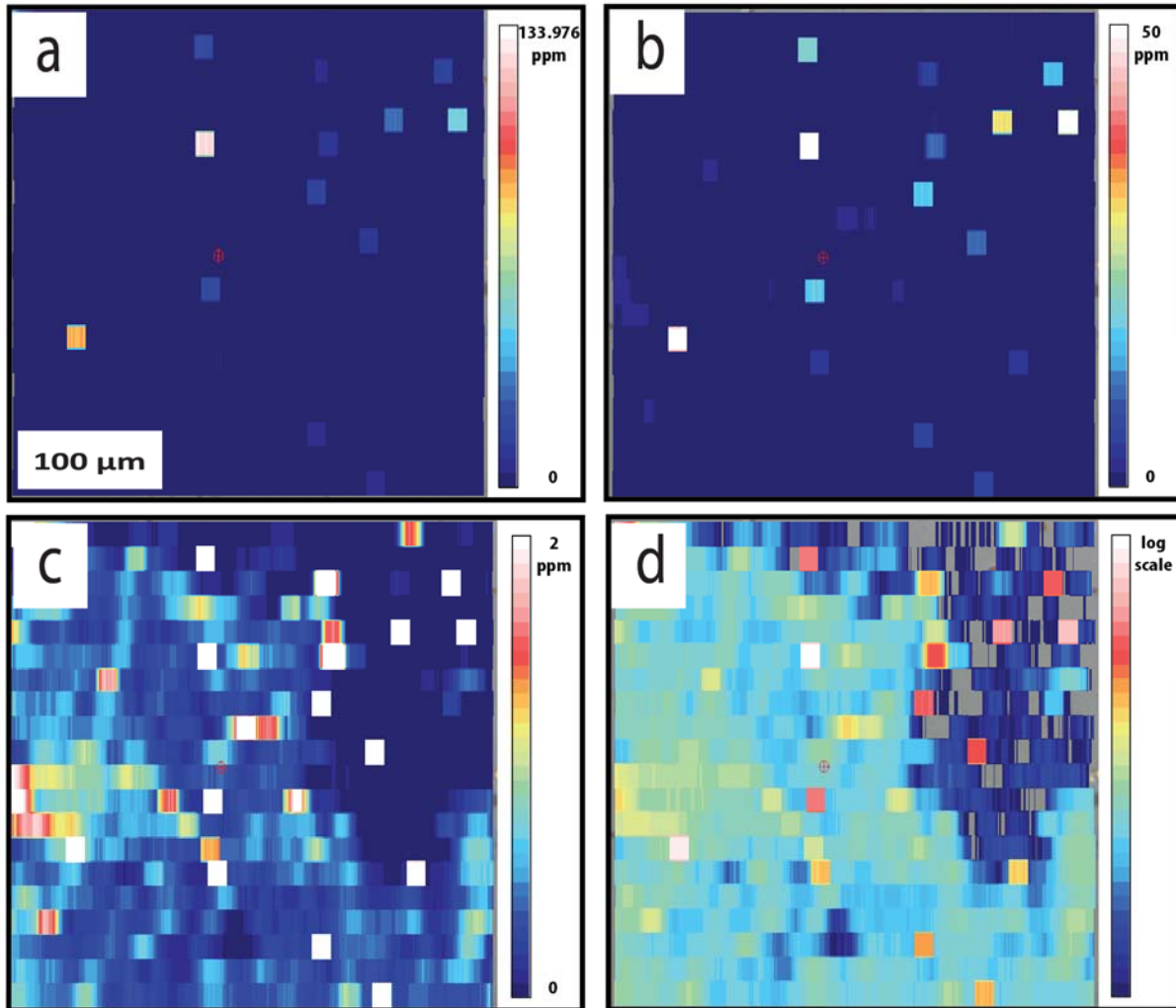


Figure 3. CellSpace images of Rb in sample 923-2277a area 3. (a) CellSpace image with automatically calculated upper limit compared to manually lowered limits (b) and (c) which begin to show additional features in the images. (d) A log scale image is also sometimes helpful at illustrating distinct groups of concentration in the image.

A comparison of the X-ray and LA-ICPMS maps shows that the element distributions are very similar, however, the spatial resolution for LA-ICPMS mapping is significantly lower (Figure 4a, 4b). The semi quantitative LA-ICPMS map concentrations from the chalcophile

experiment are comparable to the EPMA quantitative data for Fe (Figure 4b, 4e), however, in the lithophile experiment, the Fe concentration is not comparable to the EPMA data (Figure 4d, 4e). To investigate the impact of the standard reference material, the data from the lithophile experiment was reduced using MASS-1 instead of NIST610. This map shows a concentration more similar to the EPMA data than the Fe map produced using NIST610, however, the concentrations are still higher than the chalcophile experiment Fe map (Figure 4c). The cause of this could be the increase in spot size from 5 μm in the chalcophile experiment to 20 μm in the lithophile experiment. Notwithstanding the calibration issues, the spatial distributions conveyed in the elemental maps focus on the relative distributions of the different elements.

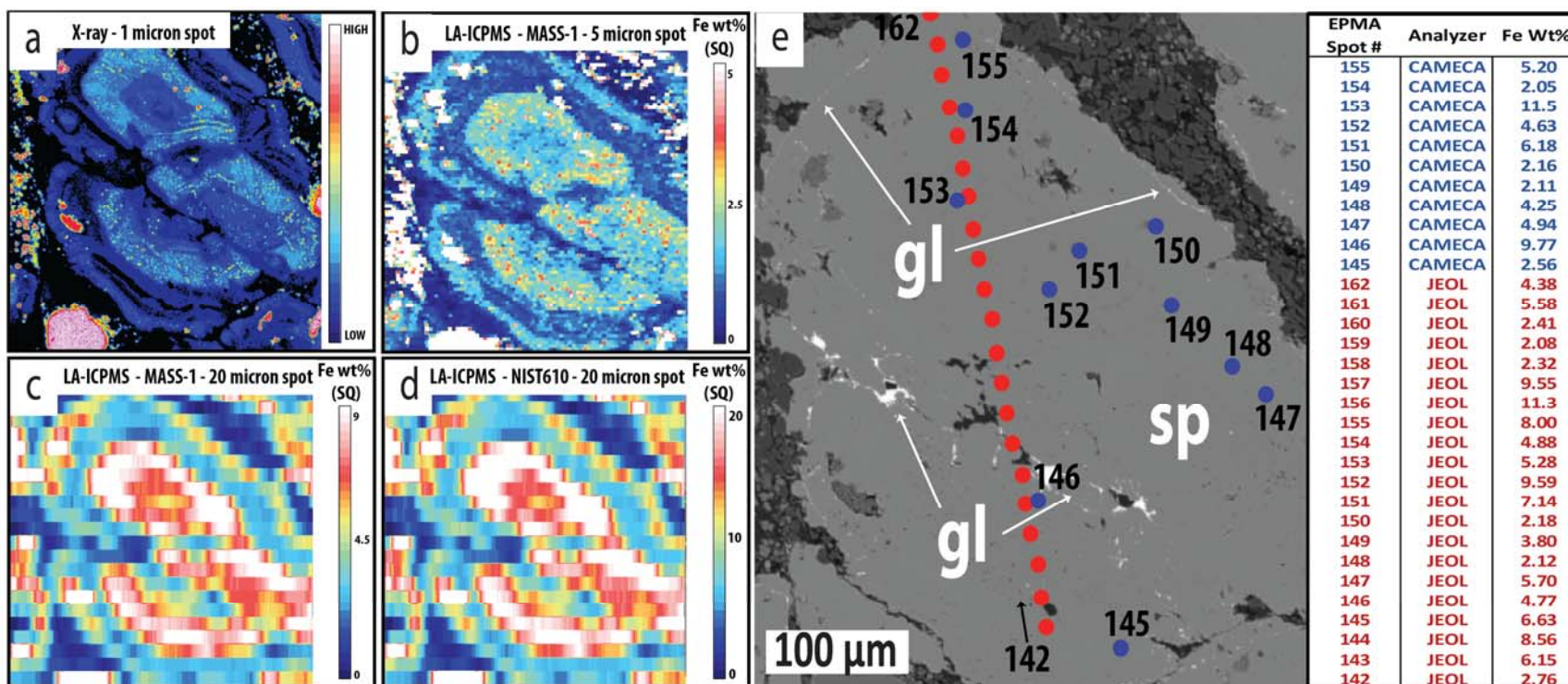
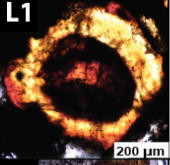
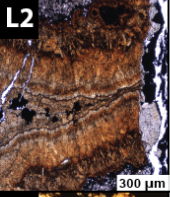
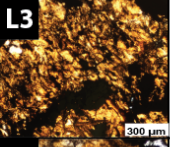
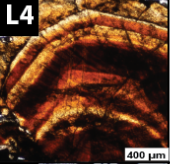
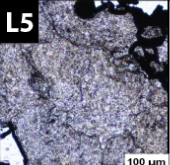
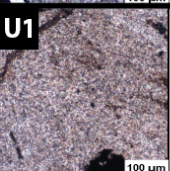


Figure 4. A comparison of qualitative X-ray element mapping, quantitative EPMA spot analyses, and semi-quantitative LA-ICPMS element mapping on the same sphalerite L1 area. (a) Iron X-ray element map using a 1 μm /pixel resolution. (b) LA-ICPMS Fe map using a 5 μm laser aperture and MASS-1 standard. (c) LA-ICPMS Fe map using a 20 μm laser aperture and MASS-1 standard. (d) LA-ICPMS Fe map using a 20 μm laser aperture and NIST610 standard. (e) BSE image with locations of EPMA spot analyses. The spot locations are accompanied by Fe wt% data for each location.

4 Results

Within the context of textures previously described by M. Reynolds (unpublished), the Anarraaq sphalerite has been further divided into 6 main generations based on morphology (Table 4). The 6 generations have been subdivided into 15 groups based on the textural and color variations present. Five of the 6 main generations are restricted to the lower ore zone, while the upper ore zone hosts a single generation. The timing of the 5 generations within the lower ore zone has been determined using relationships observed in colloform banding, banded veins, and cross-cutting relationships. The timing between lower and upper ore zone sphalerite cannot be determined. The data presented here includes detailed petrographic observations that define the sphalerite textures present, quantitative EPMA analyses, qualitative X-ray element mapping, and semi quantitative LA-ICPMS mapping to illustrate the presence and spatial distribution of minor and trace elements.

Table 4. Summary of Anarraaq sphalerite stages, textural variation, spatial occurrence, and trace element distribution determined using LA-ICPMS mapping

Ore Zone	Sphalerite Stage	Textural Description	Sample Occurrence	Spatial Distribution of Trace Elements															
				Fe	Cd	Hg	Pb	Cu	Ge	As	Ag	Sb	Tl	Na	Rb	Sr	Si	Al	Ca
Lower	 L1 L1a - dark reddish brown to black core or rim of spherical sphalerite L1b - white to light yellow brown inner rim of spherical sphalerite L1c - bright burnt orange core or outer rim of spherical sphalerite 200 μm	L1a - dark reddish brown to black core or rim of spherical sphalerite	923-2277.6	▲	▲	▲	△	△	△	△	△	△	△	○	○		○	○	
		L1b - white to light yellow brown inner rim of spherical sphalerite	923-2277.6	▲	▲	▲	△	△	△	△	△	△	△	○	○		○	○	
		L1c - bright burnt orange core or outer rim of spherical sphalerite	923-2277.6	▲	▲	▲	△	△	△	△	△	△	△	○	○		○	○	
	 L2 L2a - dark brown; fibrous to bladed L2b - light to dark burnt orange; non-fibrous L2c - light to dark burnt orange; fibrous L2d - light brown to light cream outer zone; variably fibrous 300 μm	L2a - dark brown; fibrous to bladed	923-2373.4	▲	▲	○	○			○	○	○	○	○	○	○	○	○	○
		L2b - light to dark burnt orange; non-fibrous	923-2277.6, 923-2373.4, 923-2251.2, 923-2284.9, 923-2292.9, 923-2307.9	▲	▲		▲	○	○	○	▲	▲	○	○	○	○	○	○	○
		L2c - light to dark burnt orange; fibrous	923-2373.4, 923-2292.9, 923-2307.9, 923-2376.6		○	○	◐	○	○	○	○	○	○	○	○	○	○	○	○
		L2d - light brown to light cream outer zone; variably fibrous	923-2373.4, 923-2292.9	△		△	△	△	△	△	▲		○	△	△	○		○	
	 L3 L3 - bright golden yellow; mottled texture 300 μm	L3 - bright golden yellow; mottled texture	923-2277.6	◐	◐	◐	○	○	○	○	○	○	○	○	○	○	○	○	○
		 L4 L4a - dark ruby red to dark red brown zone L4b - bright to light orange brown zone L4c - bright cream to light brown zone 400 μm	L4a - dark ruby red to dark red brown zone	923-2277.6, 923-2251.2, 923-2284.9, 923-2292.9, 923-2307.9, 1161-2209.2, 1714-2471.2	▲	▲	○	○	○	○	○	○	○	○	○	○	○	○	○
			L4b - bright to light orange brown zone	923-2277.6, 923-2251.2, 923-2284.9, 923-2292.9, 923-2307.9, 1161-2209.2, 1714-2471.2	▲	▲	○	△	○	○	○	○	○	○	○	○	○	○	○
L4c - bright cream to light brown zone	923-2277.6, 923-2251.2, 923-2284.9, 923-2292.9, 923-2307.9, 1161-2209.2		▲	△	○	△	△	△	△	△	△	△	△	△	△	△	△	△	
 L5 L5 - bright to light gray; patchy variability in color; pyrite, quartz vein association present 100 μm	L5 - bright to light gray; patchy variability in color; pyrite, quartz vein association present	923-2373.4, 1714-2471.2, 923-2292.2	▲	▲	□	△	△	△		△	△	△	△	△	○	○	○	○	
Upper	 U1 U1a - sphalerite dominant; light cream color; abundant opaque inclusions U1b - mix of U1a and U1c U1c - quartz matrix dominant; brown color 100 μm	U1a - sphalerite dominant; light cream color; abundant opaque inclusions	809-2332.7	○	●	●	◐	○	●	◐	○	○	●	●	◐	◐	○	○	
		U1b - mix of U1a and U1c	809-2332.7																
		U1c - quartz matrix dominant; brown color	809-2332.7	○	●	●	○	○	○	○	○	○	○	○	○	○	○	○	○

● = homogeneous ○ = heterogeneous ▲ = oscillatory zoning similar to color zoning ▲ = both □ = irregular zoning
 ◐ = both △ = oscillatory zoning independent of color zoning

4.1 Lower Ore Zone

The lower ore zone is characterized by 5 distinct generations of sphalerite which exhibit textural and color variability (Table 4). These 5 generations have been further subdivided, described, and analyzed in order to investigate how the geochemistry varies throughout the textural and color variability.

4.1.1 Sphalerite L1

4.1.1.1 Petrography and Texture

Sphalerite L1 is a less abundant type of sphalerite found in thin sections from sample 923-2277.6'. This sphalerite replaces pyrite spheres (ranging in size from 50 to 200 μm) as well as a fine grained ($\sim 10 \mu\text{m}$) pyrite (Figure 5a). In reflected light, the sphalerite appears as a homogenous crystal (Figure 5a, 5c, 5e), however, when viewed in transmitted light, the sphalerite has a spherical texture similar in scale to the spherical pyrite, as well as a distinct color zonation (Figure 5b, 5d, 5f). The cores of the sphalerite crystals are typically 20 to 50 μm in diameter and range in color from dark reddish brown to black (sphalerite L1a) to a bright burnt orange (sphalerite L1c; Figure 5d). These cores are surrounded by a white to light yellow-brown rim (sphalerite L1b) which is roughly 10 to 50 μm thick and occasionally an outer, thinner, bright orange, sphalerite L1c rim (Figure 5d, 5f).

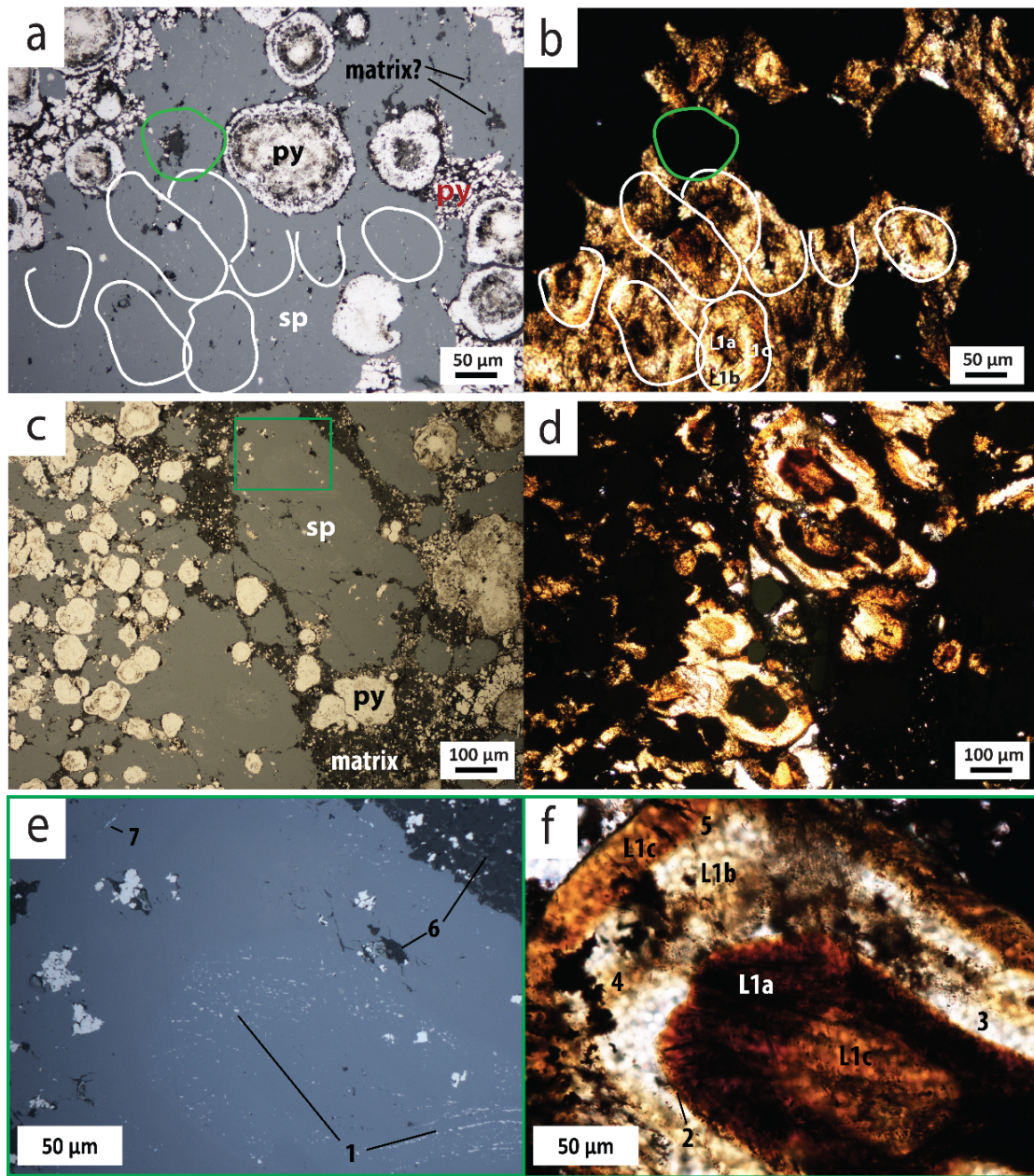


Figure 5. (a) Reflected light image from sample 923 - 2277.6a showing homogenous sphalerite (sp) replacing spherical pyrite (labeled as black 'py') and fine grained pyrite (labeled as red 'py'). (b) Transmitted light image illustrating spherical sphalerite which has a core and rim structure. Individual spherical sphalerites have been outlined (in white) in both images to emphasize how the spherical structures change in size at depth. An opaque spherical feature only visible in transmitted light is shown in green and is likely a subsurface pyrite feature. (c) Coarser spherical sphalerite surrounded by a dark, non-metallic matrix which is mostly opaque in transmitted light (d). Green box indicates locating of (e) and (f). Dark sphalerite L1a contains abundant very fine pyrite inclusions (e-1). The dark sphalerite is followed by a slight color change in the rim (f-2). Dark sphalerite is followed by a rim of white to light tan sphalerite L1b (f-3). Within the light rim, a lineation of color is seen which follows the shape of the oscillatory zoning (f-4). The light colored rim is followed by a bright orange L1c sphalerite and an area of darker L1b occurs at the transition (f-5). The matrix material later fills in around and cuts the sphalerite (e-6). Very fine galena later cuts the sphalerite (e-7).

Comparison of the spherical features visible on the surface of the thin section (Figure 5a, 5b; shown as white lines) in transmitted light and reflected light show that the spherical features change in size at depth through the 30 μm thin section and are truly 3-dimensional.

In reflected light, many submicron inclusions of pyrite are present (Figure 5e-1) which makes sphalerite L1a opaque in transmitted light (Figure 5f). In some areas of the sphalerite, an opaque circle can be seen in transmitted light (Figure 5a, 5b; outlined as green line); this may be due to an opaque spherical feature located below the surface of the thin section.

The L1 sphalerite is associated with a very fine grained and dark matrix material (Figure 5a, 5c, 5e). This material is dominated by sulfides (pyrite, sphalerite, and galena) along with quartz and organic material (Figure 5e, 5f). In some cases, the material appears to be cutting the sphalerite (Figure 5c, 5e-6), however, in other areas, it appears that the material has been incorporated into the sphalerite during precipitation (Figure 5a). Submicron grains of galena are also seen crosscutting sphalerite L1 (Figure 5e-7).

4.1.1.2 Composition determined by EPMA and LA-ICPMS

4.1.1.2.1 *Chalcophile (+Fe) elements*

Major element analyses by EMPA indicates that L1 sphalerite does not have a theoretical end member ZnS composition (Figure 6a). The Zn concentration ranges from 51.9 to 65.6 wt% and S concentration ranges from 32.0 to 33.7 wt% (Figure 7; Table 5). There is also compositional variability between the different L1 subgroups. Sphalerite L1a and L1c have the widest range in Zn data, whereas stage L1b has a restricted range in Zn concentrations (Figure 7; Table 5). Additionally, sphalerite L1b has the highest mean Zn concentrations (Figure 7; Table 5).

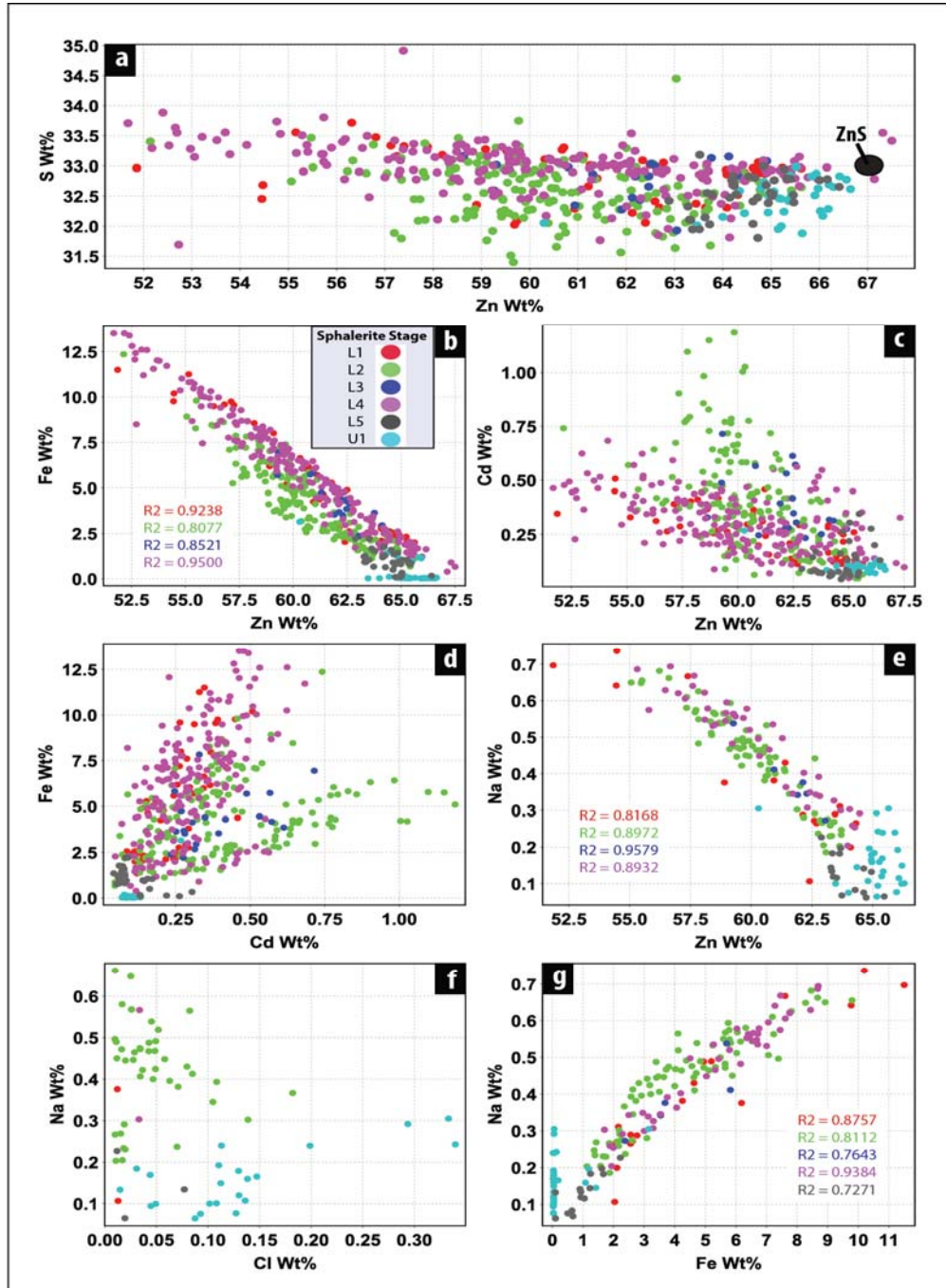


Figure 6. Combined JEOL and CAMECA analyses. (a) Zinc wt% versus S wt% plot showing range in Zn and S concentrations relative to pure ZnS (67% Zn, 33% S; shown as black dot). The later stage sphalerite L5 as well as the upper ore zone (U1) plot closest to the ZnS whereas the earlier stages vary significantly from the ZnS. (b) Plot of Zn wt% and Fe wt% showing a strong negative correlation in sphalerite stages L1-L4. R² values reported are the calculated coefficient of determination (R²). (c) Plot of Zn wt% and Cd wt% which does not show a strong negative correlation, however, a negative trend is observed. Sphalerite L2 strays furthest from the trend. (d) Iron wt% and Cd wt% show a positive trend which is also not a strong correlation. (e) Zinc and Na stages L1-L4 also show a strong negative correlation. (f) Sodium and Cl are not related. (g) Sodium and Fe indicate a variably strong positive correlation which supports the Zn and Na relationship observed.

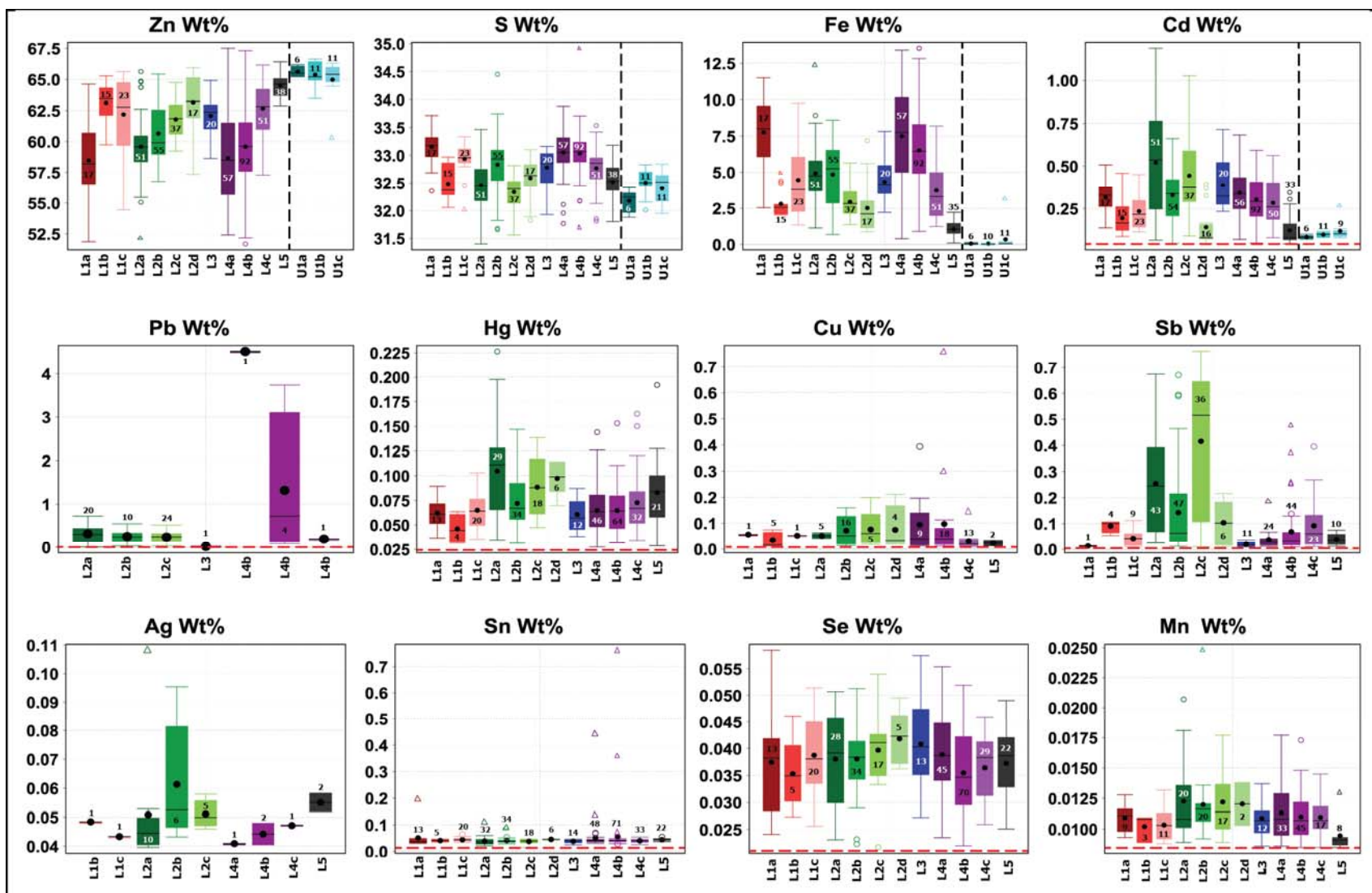


Figure 7. Box plots showing distribution of major and minor elements throughout the sphalerite textures. Red dashed line = LOD. Black dashed line = divide between lower and upper ore zone generations. Filled box represents range in data from first quartile to third quartile. Whiskers represent minimum and maximum in data. Black line = median. Black dot = mean value. Outliers are represented as individual symbols.

Table 5. Descriptive statistics of combined weight percent (Wt%) data of 13 elements obtained from 322 electron probe microanalyses (EPMA) using the wave dispersive spectrometer (WDS) on the JEOL JXA-8900 Superprobe and 18 elements obtained from 189 electron probe microanalyses (EPMA) using the wave dispersive spectrometer (WDS) on the Cameca SX100.

<i>Sphalerite Texture</i>	<i>Statistic</i>	<i>Zn</i>	<i>S</i>	<i>Cd</i>	<i>Fe</i>	<i>Pb</i>	<i>Hg</i>	<i>Cu</i>	<i>Sb</i>	<i>Ag</i>	<i>Sn</i>	<i>Se</i>	<i>Mn</i>	<i>As</i>	<i>Rb</i>	<i>Sr</i>	<i>Na</i>	<i>Cl</i>	<i>Si</i>	<i>Al</i>	<i>Ca</i>	<i>Ba</i>
L1a	Count	17	17	17	17	0	13	1	2	0	13	13	9	0	0	0	4	1	0	1	0	0
	Min	51.86	32.36	0.136	2.540	blid	0.037	0.056	0.012	blid	0.031	0.024	0.009	blid	blid	blid	0.376	0.012	blid	0.227	blid	blid
	Max	64.63	33.72	0.507	11.50	blid	0.089	0.056	0.015	blid	0.198	0.059	0.013	blid	blid	blid	0.737	0.012	blid	0.227	blid	blid
	Mean	58.47	33.16	0.316	7.770	blid	0.062	0.056	0.013	blid	0.051	0.037	0.011	blid	blid	blid	0.619	0.012	blid	0.227	blid	blid
	Median	58.19	33.18	0.330	8.003	blid	0.061	0.056	0.013	blid	0.037	0.038	0.011	blid	blid	blid	0.682	0.012	blid	0.227	blid	blid
	St Dev	3.163	0.322	0.092	2.429	blid	0.014	0.000	0.002	blid	0.045	0.009	0.001	blid	blid	blid	0.165	0.000	blid	0.000	blid	blid
L1b	Count	15	15	15	15	0	4	5	4	1	5	5	3	0	0	0	10	1	0	0	1	0
	Min	59.74	32.06	0.086	2.038	blid	0.032	0.011	0.053	0.048	0.036	0.027	0.009	blid	blid	blid	0.107	0.013	blid	blid	0.007	blid
	Max	65.28	32.97	0.458	4.945	blid	0.064	0.074	0.106	0.048	0.046	0.046	0.011	blid	blid	blid	0.488	0.013	blid	blid	0.007	blid
	Mean	63.11	32.48	0.194	2.800	blid	0.046	0.034	0.090	0.048	0.041	0.035	0.010	blid	blid	blid	0.287	0.013	blid	blid	0.007	blid
	Median	63.45	32.38	0.166	2.557	blid	0.044	0.016	0.101	0.048	0.042	0.035	0.011	blid	blid	blid	0.280	0.013	blid	blid	0.007	blid
	St Dev	1.645	0.311	0.098	0.937	blid	0.015	0.029	0.025	0.000	0.004	0.007	0.001	blid	blid	blid	0.101	0.000	blid	blid	0.000	blid
L1c	Count	23	23	23	23	0	20	1	9	1	20	20	11	0	0	0	3	0	0	0	1	0
	Min	54.45	32.03	0.113	1.351	blid	0.035	0.052	0.010	0.043	0.034	0.026	0.009	blid	blid	blid	0.430	blid	blid	blid	0.031	blid
	Max	65.62	33.34	0.450	9.767	blid	0.103	0.052	0.112	0.043	0.064	0.051	0.013	blid	blid	blid	0.642	blid	blid	blid	0.031	blid
	Mean	62.19	32.94	0.234	4.460	blid	0.065	0.052	0.042	0.043	0.045	0.039	0.010	blid	blid	blid	0.520	blid	blid	blid	0.031	blid
	Median	62.77	32.96	0.217	3.805	blid	0.064	0.052	0.042	0.043	0.044	0.038	0.010	blid	blid	blid	0.489	blid	blid	blid	0.031	blid
	St Dev	3.033	0.271	0.104	2.554	blid	0.018	0.000	0.033	0.000	0.008	0.008	0.001	blid	blid	blid	0.109	blid	blid	blid	0.000	blid
L2a	Count	51	51	51	51	20	29	5	43	10	32	28	20	0	0	0	21	11	2	0	2	0
	Min	52.14	31.40	0.064	1.126	0.009	0.035	0.041	0.025	0.040	0.021	0.023	0.009	blid	blid	blid	0.410	0.011	0.010	blid	0.008	blid
	Max	65.63	33.47	1.187	12.36	0.721	0.226	0.063	0.675	0.108	0.112	0.051	0.021	blid	blid	blid	0.650	0.049	0.013	blid	0.010	blid
	Mean	59.59	32.46	0.521	4.921	0.313	0.105	0.051	0.254	0.051	0.039	0.038	0.012	blid	blid	blid	0.518	0.032	0.011	blid	0.009	blid
	Median	59.57	32.45	0.536	4.742	0.300	0.111	0.051	0.245	0.045	0.035	0.039	0.011	blid	blid	blid	0.506	0.028	0.011	blid	0.009	blid
	St Dev	2.485	0.423	0.291	1.958	0.212	0.045	0.009	0.201	0.021	0.017	0.009	0.003	blid	blid	blid	0.067	0.012	0.002	blid	0.001	blid
L2b	Count	55	55	54	55	10	34	16	47	6	34	34	20	0	0	0	21	10	3	1	5	0
	Min	56.76	31.66	0.046	0.679	0.031	0.032	0.014	0.012	0.043	0.029	0.022	0.009	blid	blid	blid	0.203	0.010	0.014	0.040	0.006	blid
	Max	65.42	34.45	0.662	8.611	0.547	0.147	0.160	0.671	0.095	0.091	0.051	0.025	blid	blid	blid	0.626	0.108	0.050	0.040	0.021	blid
	Mean	60.65	32.83	0.329	4.845	0.250	0.072	0.072	0.142	0.061	0.042	0.038	0.012	blid	blid	blid	0.437	0.042	0.032	0.040	0.012	blid
	Median	59.90	32.93	0.339	5.244	0.239	0.067	0.052	0.062	0.053	0.039	0.038	0.012	blid	blid	blid	0.472	0.027	0.033	0.040	0.009	blid
	St Dev	2.171	0.507	0.138	2.111	0.166	0.026	0.052	0.168	0.020	0.014	0.006	0.003	blid	blid	blid	0.134	0.035	0.018	0.000	0.006	blid
L2c	Count	37	37	37	37	24	18	5	36	5	18	17	17	0	0	0	19	18	0	0	0	0
	Min	59.23	31.56	0.089	1.367	0.032	0.047	0.019	0.010	0.046	0.016	0.022	0.009	blid	blid	blid	0.205	0.010	blid	blid	blid	blid
	Max	64.76	32.82	1.027	5.649	0.517	0.139	0.198	0.763	0.058	0.047	0.054	0.018	blid	blid	blid	0.475	0.182	blid	blid	blid	blid
	Mean	61.79	32.34	0.444	2.936	0.236	0.089	0.076	0.416	0.051	0.038	0.040	0.012	blid	blid	blid	0.370	0.057	blid	blid	blid	blid
	Median	61.85	32.40	0.375	2.829	0.242	0.088	0.060	0.516	0.050	0.039	0.041	0.011	blid	blid	blid	0.400	0.048	blid	blid	blid	blid
	St Dev	1.417	0.310	0.216	1.023	0.121	0.030	0.072	0.255	0.005	0.008	0.007	0.003	blid	blid	blid	0.090	0.046	blid	blid	blid	blid
L2d	Count	17	17	16	17	0	6	4	6	0	6	5	2	0	0	0	11	2	1	0	3	0
	Min	57.34	31.83	0.046	0.873	blid	0.070	0.019	0.011	blid	0.043	0.036	0.010	blid	blid	blid	0.145	0.020	0.007	blid	0.009	blid
	Max	65.94	33.10	0.392	7.194	blid	0.114	0.211	0.216	blid	0.047	0.050	0.014	blid	blid	blid	0.610	0.070	0.007	blid	0.011	blid
	Mean	63.15	32.59	0.141	2.518	blid	0.097	0.075	0.103	blid	0.046	0.042	0.012	blid	blid	blid	0.303	0.045	0.007	blid	0.010	blid
	Median	63.25	32.63	0.078	2.121	blid	0.099	0.034	0.101	blid	0.046	0.042	0.012	blid	blid	blid	0.259	0.045	0.007	blid	0.010	blid
	St Dev	2.428	0.343	0.115	1.858	blid	0.017	0.091	0.092	blid	0.001	0.005	0.002	blid	blid	blid	0.160	0.035	0.000	blid	0.001	blid
L3	Count	20	20	20	20	1	12	0	11	0	14	13	12	0	0	0	6	0	0	1	0	0
	Min	58.63	31.93	0.234	2.207	0.018	0.038	blid	0.10	blid	0.024	0.027	0.009	blid	blid	blid	0.273	blid	blid	0.028	blid	blid
	Max	64.91	33.16	0.715	7.834	0.018	0.087	blid	0.036	blid	0.046	0.058	0.014	blid	blid	blid	0.538	blid	blid	0.028	blid	blid
	Mean	62.08	32.78	0.387	4.334	0.018	0.061	blid	0.019	blid	0.038	0.041	0.011	blid	blid	blid	0.381	blid	blid	0.028	blid	blid
	Median	62.38	32.85	0.324	4.153	0.018	0.057	blid	0.018	blid	0.041	0.040	0.011	blid	blid	blid	0.361	blid	blid	0.028	blid	blid
	St Dev	1.672	0.338	0.143	1.464	0.000	0.016	blid	0.009	blid	0.007	0.009	0.001	blid	blid	blid	0.090	blid	blid	0.000	blid	blid

Table 5. Continued

<i>Sphalerite Texture</i>	<i>Statistic</i>	<i>Zn</i>	<i>S</i>	<i>Cd</i>	<i>Fe</i>	<i>Pb</i>	<i>Hg</i>	<i>Cu</i>	<i>Sb</i>	<i>Ag</i>	<i>Sn</i>	<i>Se</i>	<i>Mn</i>	<i>As</i>	<i>Rb</i>	<i>Sr</i>	<i>Na</i>	<i>Cl</i>	<i>Si</i>	<i>Al</i>	<i>Ca</i>	<i>Ba</i>
L4a	Count	57	57	56	57	1	46	9	24	1	48	45	33	0	0	0	10	0	0	1	0	0
	Min	52.40	31.77	0.069	0.396	4.520	0.028	0.012	0.012	0.041	0.031	0.024	0.009	blid	blid	blid	0.363	blid	blid	0.008	blid	blid
	Max	67.50	33.88	0.683	13.40	4.520	0.144	0.394	0.186	0.041	0.444	0.055	0.018	blid	blid	blid	0.694	blid	blid	0.008	blid	blid
	Mean	58.65	33.05	0.343	7.503	4.520	0.065	0.094	0.037	0.041	0.052	0.039	0.011	blid	blid	blid	0.601	blid	blid	0.008	blid	blid
	Median	58.49	33.06	0.338	7.757	4.520	0.064	0.039	0.028	0.041	0.040	0.039	0.011	blid	blid	blid	0.621	blid	blid	0.008	blid	blid
	St Dev	3.821	0.407	0.141	3.340	0.000	0.024	0.126	0.035	0.000	0.060	0.007	0.002	blid	blid	blid	0.097	blid	blid	0.000	blid	blid
L4b	Count	92	92	92	92	4	64	18	44	2	71	70	45	0	0	0	21	1	0	0	0	
	Min	51.68	31.69	0.047	0.905	0.090	0.032	0.012	0.010	0.041	0.028	0.022	0.009	blid	blid	blid	0.349	0.010	blid	blid	blid	blid
	Max	67.32	34.92	0.593	13.53	3.736	0.153	0.760	0.478	0.048	0.763	0.052	0.017	blid	blid	blid	0.687	0.010	blid	blid	blid	blid
	Mean	59.59	33.04	0.303	6.517	1.317	0.065	0.097	0.068	0.044	0.055	0.035	0.011	blid	blid	blid	0.539	0.010	blid	blid	blid	blid
	Median	59.63	33.07	0.291	6.453	0.721	0.064	0.039	0.033	0.044	0.041	0.035	0.011	blid	blid	blid	0.545	0.010	blid	blid	blid	blid
	St Dev	3.202	0.373	0.119	2.680	1.687	0.023	0.178	0.097	0.005	0.093	0.008	0.002	blid	blid	blid	0.083	0.000	blid	blid	blid	blid
L4c	Count	51	51	50	51	1	32	13	23	2	33	29	17	0	0	0	19	2	0	0	1	
	Min	57.29	31.81	0.079	1.228	0.191	0.034	0.008	0.011	0.047	0.026	0.026	0.009	blid	blid	blid	0.204	0.033	blid	blid	0.007	blid
	Max	66.16	33.54	0.562	8.194	0.191	0.163	0.146	0.395	0.047	0.054	0.046	0.015	blid	blid	blid	0.606	0.034	blid	blid	0.007	blid
	Mean	62.67	32.77	0.283	3.741	0.191	0.073	0.031	0.092	0.047	0.041	0.036	0.011	blid	blid	blid	0.381	0.033	blid	blid	0.007	blid
	Median	62.82	32.86	0.261	3.302	0.191	0.067	0.020	0.060	0.047	0.040	0.038	0.011	blid	blid	blid	0.343	0.033	blid	blid	0.007	blid
	St Dev	2.199	0.339	0.137	1.963	0.000	0.030	0.036	0.094	0.000	0.007	0.006	0.001	blid	blid	blid	0.114	0.000	blid	blid	0.000	blid
L5	Count	38	38	33	35	0	21	2	10	2	22	22	8	0	0	0	15	3	0	0	2	
	Min	62.89	31.81	0.042	0.101	blid	0.029	0.013	0.012	0.052	0.037	0.025	0.009	blid	blid	blid	0.062	0.012	blid	blid	0.007	blid
	Max	66.41	33.18	0.345	2.221	blid	0.192	0.034	0.074	0.058	0.055	0.049	0.013	blid	blid	blid	0.227	0.077	blid	blid	0.007	blid
	Mean	64.51	32.52	0.122	1.061	blid	0.083	0.023	0.039	0.055	0.044	0.037	0.009	blid	blid	blid	0.129	0.036	blid	blid	0.007	blid
	Median	64.63	32.53	0.079	1.044	blid	0.084	0.023	0.036	0.055	0.044	0.039	0.009	blid	blid	blid	0.132	0.019	blid	blid	0.007	blid
	St Dev	0.862	0.322	0.081	0.549	blid	0.037	0.015	0.021	0.004	0.004	0.006	0.001	blid	blid	blid	0.052	0.036	blid	blid	0.001	blid
U1a	Count	6	6	6	6	0	0	0	0	0	0	0	0	0	0	0	6	6	0	0	0	
	Min	65.21	31.88	0.070	0.032	blid	blid	blid	blid	blid	blid	blid	blid	blid	blid	blid	0.100	0.049	blid	blid	blid	blid
	Max	66.19	32.42	0.100	0.132	blid	blid	blid	blid	blid	blid	blid	blid	blid	blid	blid	0.305	0.340	blid	blid	blid	blid
	Mean	65.62	32.18	0.083	0.056	blid	blid	blid	blid	blid	blid	blid	blid	blid	blid	blid	0.187	0.183	blid	blid	blid	blid
	Median	65.51	32.25	0.083	0.040	blid	blid	blid	blid	blid	blid	blid	blid	blid	blid	blid	0.176	0.134	blid	blid	blid	blid
	St Dev	0.410	0.200	0.010	0.038	blid	blid	blid	blid	blid	blid	blid	blid	blid	blid	blid	0.077	0.122	blid	blid	blid	blid
U1b	Count	11	11	11	10	0	0	0	0	0	0	0	0	0	0	0	8	11	4	3	0	
	Min	63.47	32.01	0.080	0.027	blid	blid	blid	blid	blid	blid	blid	blid	blid	blid	blid	0.065	0.025	0.008	0.049	blid	blid
	Max	66.65	32.83	0.117	0.065	blid	blid	blid	blid	blid	blid	blid	blid	blid	blid	blid	0.184	0.130	0.010	0.516	blid	blid
	Mean	65.37	32.50	0.097	0.038	blid	blid	blid	blid	blid	blid	blid	blid	blid	blid	blid	0.127	0.068	0.009	0.244	blid	blid
	Median	65.21	32.50	0.100	0.034	blid	blid	blid	blid	blid	blid	blid	blid	blid	blid	blid	0.125	0.052	0.010	0.168	blid	blid
	St Dev	1.033	0.245	0.013	0.011	blid	blid	blid	blid	blid	blid	blid	blid	blid	blid	blid	0.049	0.037	0.001	0.243	blid	blid
U1c	Count	11	11	9	11	0	0	0	0	0	0	0	0	0	0	0	10	9	9	3	0	
	Min	60.30	31.95	0.078	0.028	blid	blid	blid	blid	blid	blid	blid	blid	blid	blid	blid	0.077	0.015	0.012	0.008	blid	0.026
	Max	66.29	32.84	0.268	3.149	blid	blid	blid	blid	blid	blid	blid	blid	blid	blid	blid	0.305	0.294	0.147	0.041	blid	0.026
	Mean	64.97	32.40	0.118	0.345	blid	blid	blid	blid	blid	blid	blid	blid	blid	blid	blid	0.178	0.132	0.036	0.023	blid	0.026
	Median	65.40	32.51	0.102	0.047	blid	blid	blid	blid	blid	blid	blid	blid	blid	blid	blid	0.149	0.127	0.019	0.021	blid	0.026
	St Dev	1.655	0.288	0.058	0.931	blid	blid	blid	blid	blid	blid	blid	blid	blid	blid	blid	0.084	0.081	0.044	0.016	blid	0.000

In addition to the major elements, several minor elements were also detected in significant quantities. Iron is the most abundant of the minor elements analyzed and was detected in all 55 of the L1 EPMA analyses (Figure 7; Table 5). Iron is present in all 3 of the L1 textures and ranges in concentration from 1.35 to 11.5 wt% (Figure 7; Table 5). The association between color in L1 sphalerite and the Fe content is best observed in Fe X-ray and LA-ICPMS element maps (Figure 8, 9). A plot of Zn versus Fe concentrations shows that the EPMA data is strongly negatively correlated (i.e. Fe wt% increases in concentration as Zn wt % decreases; Figure 6b) in L1 sphalerite.

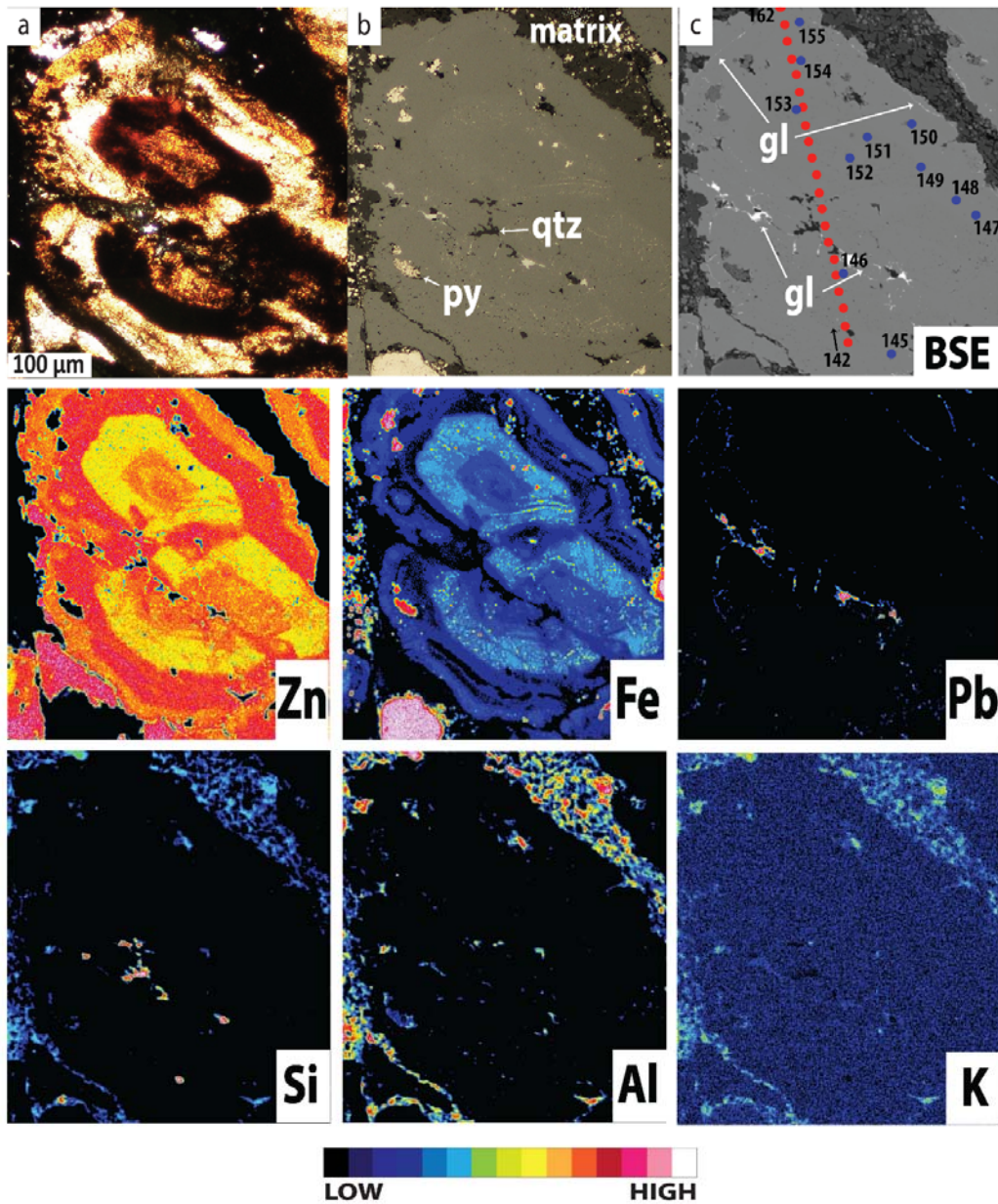


Figure 8. (a) Transmitted light photomicrograph of oscillatory zoned sphalerite L1 in sample 923 2277.6a. (b) Reflected light photomicrograph showing locations of pyrite and quartz within the sphalerite as well as matrix material which is surrounding the sphere of sphalerite. (c) BSE image of sphalerite stage L1 shows cross cutting galena and locations of spot analyses. Zinc (Zn) X-ray map of sphalerite L1 shows a variation in Zn concentration. Oscillatory zoning is seen in the Fe X-ray map and correlates with the sphalerite color and Zn spatial distribution. Lead (Pb) X-ray map illustrates spatial distribution of cross cutting galena. Silicon (Si), Al, and K X-ray maps show a presence in the matrix as well as cross cutting the sphalerite.

Cadmium was also detected in all 55 L1 EPMA analyses (Figure 7; Table 5) with concentrations that range from 0.09 to 0.51 wt%. There is also a broad negative trend between Zn and Cd values in sphalerite L1, however, a wide scatter is observed (Figure 6c). Element mapping of Cd by LA-ICPMS shows that the zonation in Cd content differs slightly from that of the zoning denoted by the color and Fe concentration (Figure 9). The Fe rich core has been outlined in red and overlaid on the Cd map and photomicrograph to illustrate that the Cd concentration extends into the Fe poor rim (Figure 9).

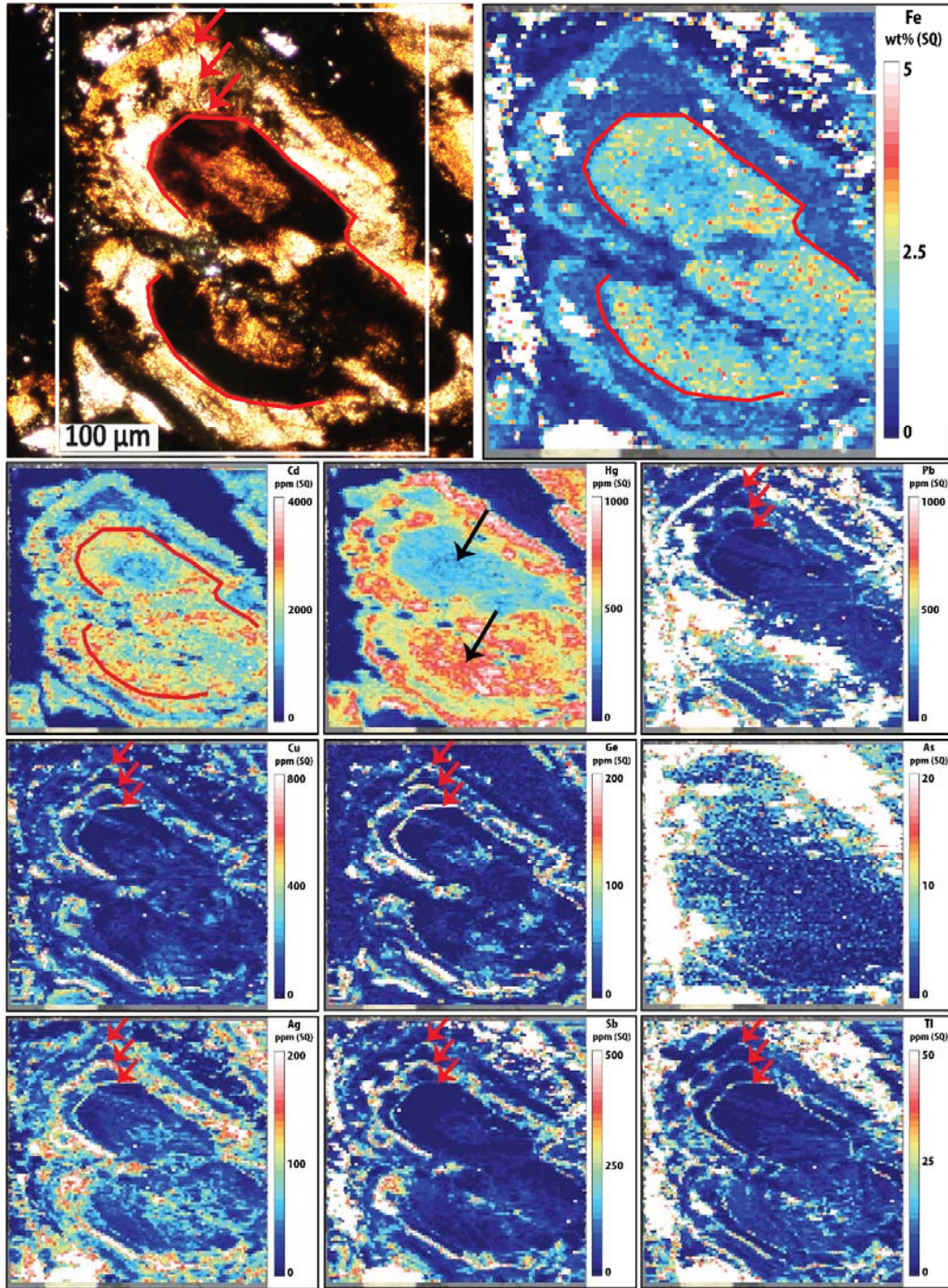


Figure 9. Quadrupole laser ablation element mapping of sphalerite L1. The white box represents the area that was mapped. The red lines were traced along the rim of the Fe rich zone and then overlaid on the photomicrograph of the mapped area and the Cd map. Zinc (Zn) and Fe spatially correlate with the oscillatory color zonation, however, Cd and Hg appear independent of the color zonation. The Cd extends past the Fe rich-Fe poor transition (red lines). Mercury is variably present in the Fe rich cores (black arrows). The additional trace element maps show a narrow oscillatory zoning pattern (red arrows) which is independent from the zoning seen in the Fe concentration and L1 color. The innermost zone (lower red arrow) occurs along the rim of the Fe rich L1b sphalerite. An additional

narrow band is present within the Fe poor L1b stage of sphalerite (middle red arrow). A third zone is present along the rim of the L1b sphalerite (upper red arrow).

Mercury was determined to be quantitatively present in 37 L1 analyses ranging from 0.03 to 0.10 wt% (Figure 7; Table 5). The data indicate that Fe poor L1b has a slightly lower Hg concentration (Figure 7; Table 5), however, the LA-ICPMS element map presented in Figure 9 shows that the spatial distribution of Hg is decoupled from the zoning evident in color, Fe, and Cd concentrations.

Lead was not quantitatively present in the stage L1 sphalerite above the EPMA LOD (Table 2, 3 for EPMA LOD; Figure 7; Table 5). However, a very fine scale oscillatory zoning of low concentration Pb (ppm levels) is evident in the L1 sphalerite (Figure 9, red arrows). The zoning is similar in shape and orientation to that defined by the color variation, however, in detail, it does not mirror the color (and major element) zoning precisely. The innermost zone of high Pb concentrations occurs along the rim of Fe rich L1a (Figure 9, bottom arrow). An additional narrow band is present within the Fe poor L1b stage of sphalerite and under high magnification, can be seen as a dark lineation in this sphalerite (Figure 5f-4, 9). Furthermore, the Pb zone within the light colored L1b zone occurs along the boundary between Cd rich L1b and Cd poor L1b (Figure 9, top arrow).

Copper, Ge, As, Ag, Sb, and Tl were also detected and mapped in trace quantities by the LA-ICPMS and have zoning similar to the Pb (Figure 9). Of these elements, only Cu, Ag, and Sb were quantitatively present above the EPMA LOD (Ge and Tl were not quantitatively analyzed) in very few analyses (7 Cu, 2 Ag, and 15 Sb) and in trace concentrations (typically <0.10 wt %) (Figure 7; Table 5).

Several additional chalcophile elements were present in the L1 sphalerite, but were not mapped. Manganese was detected in 23 EPMA analyses and had values averaging 0.01 wt% (Figure 7; Table 5). Selenium and Sn were detected in 38 EPMA spots (0.02 to 0.06 wt% and 0.03 to 0.20 wt%, respectively; Figure 7, Table 5).

4.1.1.2.2 *Lithophile elements*

Lithophile elements were also analyzed in sphalerite L1. Sodium was detected in 17 quantitative EPMA analyses at concentrations ranging from 0.11 to 0.74 wt% (Figure 10; Table 5). Similarly to Fe, L1a has the highest mean Na value whereas L1b has low values (Figure 7,

10; Table 5). The Na wt% increases in concentration as Zn wt % decreases (Figure 6e) and there is a significant negative correlation between the Zn and Na data (Figure 6e). Additionally, Na and Fe are positively correlated (Figure 6g). The spatial distribution of the Na in the sphalerite L1 LA-ICPMS map is difficult to determine because of the high concentration of Na in the surrounding material (Figure 11).

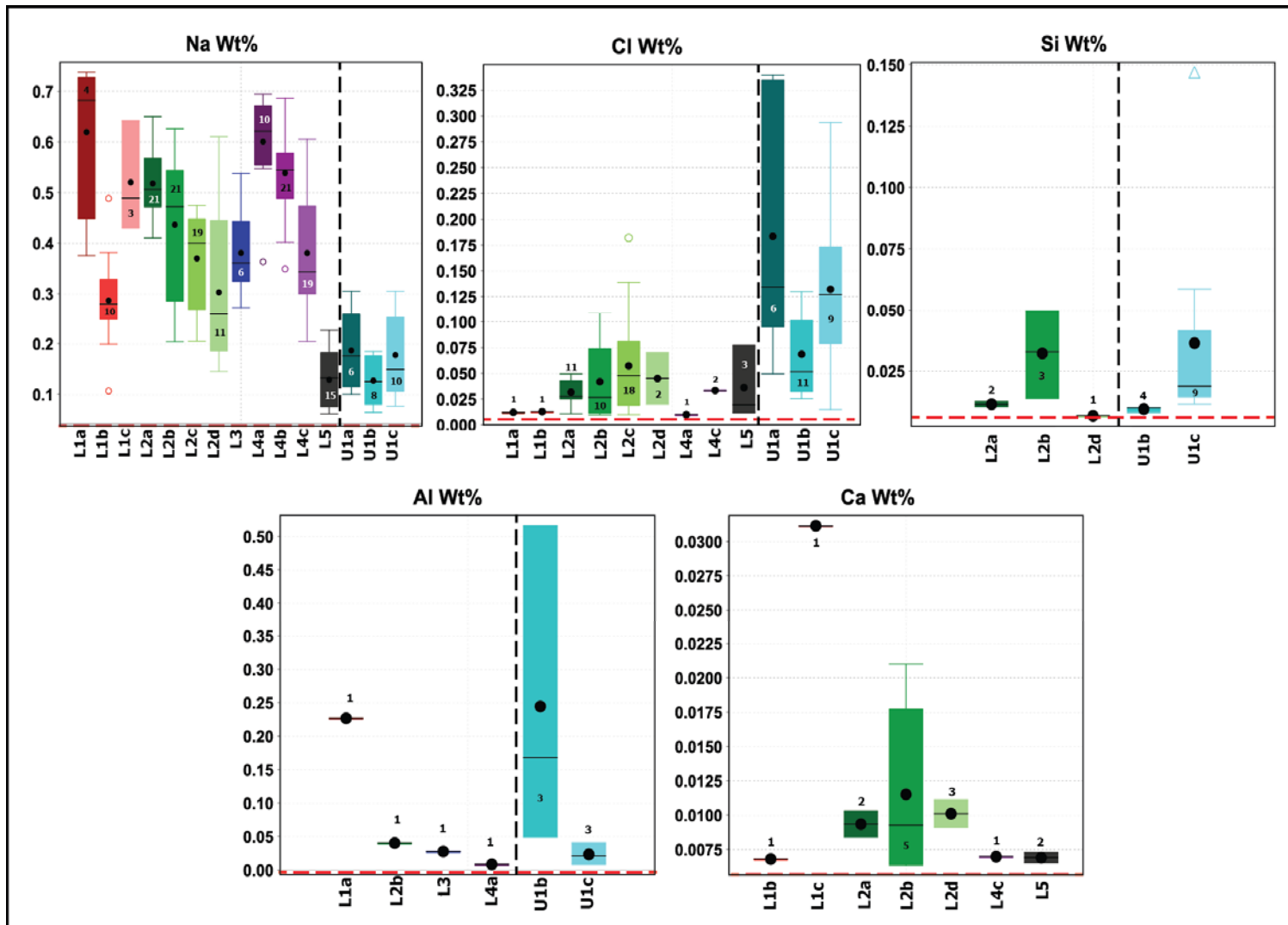
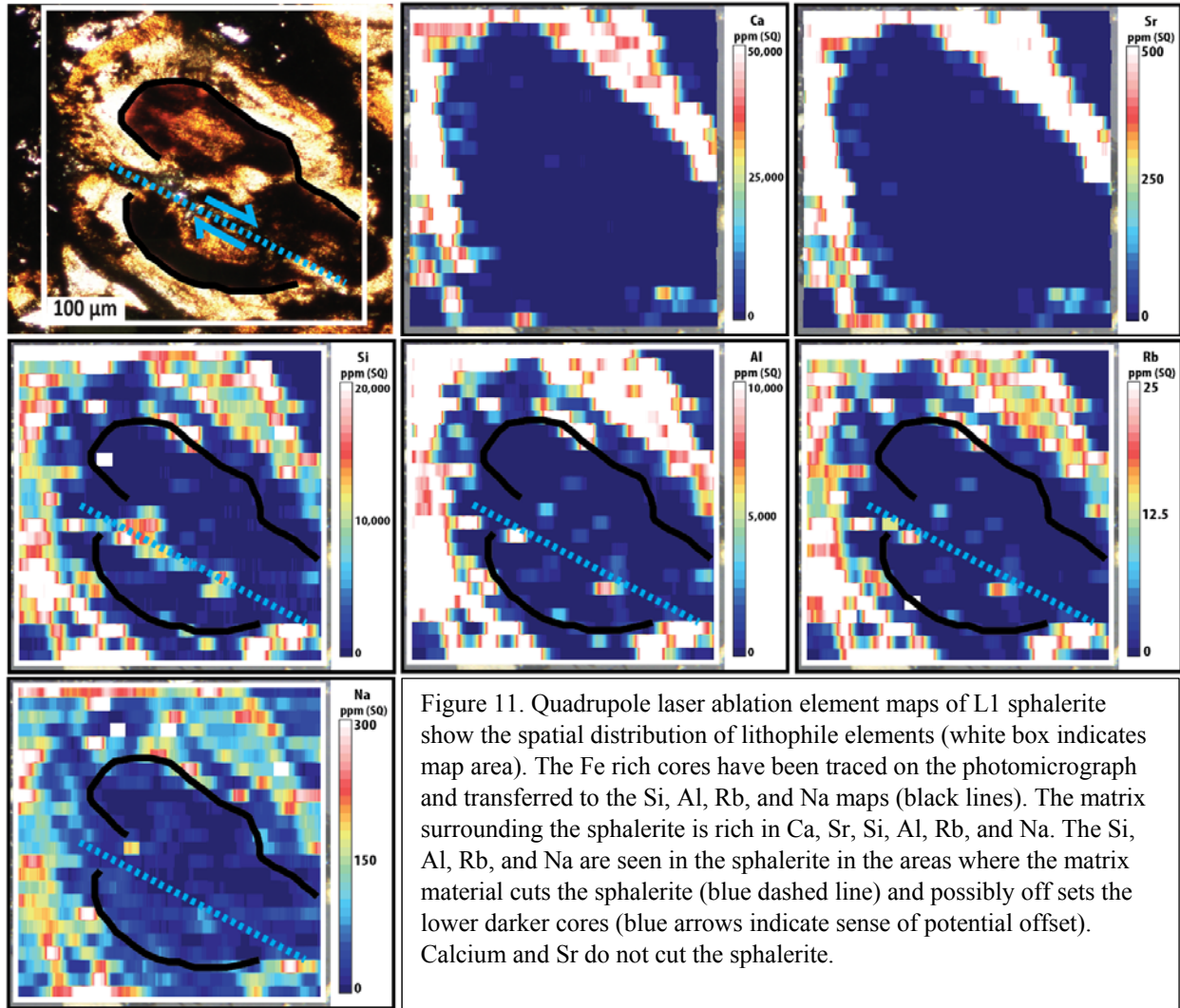


Figure 10. Combined JOEL and CAMECA box plots showing spatial distribution of lithophile elements through the sphalerite generations. Red dashed line = LOD. Black dashed line = divide between lower and upper ore zone generations. Box represents range in data from first quartile to third quartile. Whiskers represent minimum and maximum in data. Black line = median. Black dot = mean value. Outliers are represented as individual symbols.



Chlorine was only detected in 2 EPMA spots (Figure 10; Table 5), and is present in much lower concentrations (<0.02 wt%).

Silicon, Al, and Rb are present in significant concentrations in the matrix material and not in the sphalerite itself (Figure 8, 11). Calcium and Sr are also present in the matrix material that surrounds the L1 grain in Figure 11, however, these elements are not seen in the matrix material which cross cuts the sphalerite unlike Si, Al, and Rb (Figure 11, blue dashed line). The matrix material rich in these elements may have even offset the lower Fe rich sphalerite core (Figure 11, blue arrows).

4.1.2 Sphalerite L2

4.1.2.1 Petrography and Texture

Sphalerite L2 is abundant in the Anarraaq thin sections and is one of the two dominant types of sphalerite (Table 4) in this study. Sphalerite L2 is dominated by variably fibrous to bladed textures which exhibit distinct color zonation. Veins of sphalerite L2 are cut by later sphalerite L5 (Figure 12a, 12b, 12c) and have a dark brown fibrous to bladed texture (sphalerite L2a) with individual blades as long as 150 μm (Figure 12b). Aligned inclusions of pyrite (or marcasite) and quartz in sphalerite L2a are seen in reflected light (Figure 12a) and are similar in scale to the sphalerite blades (Figure 12b).

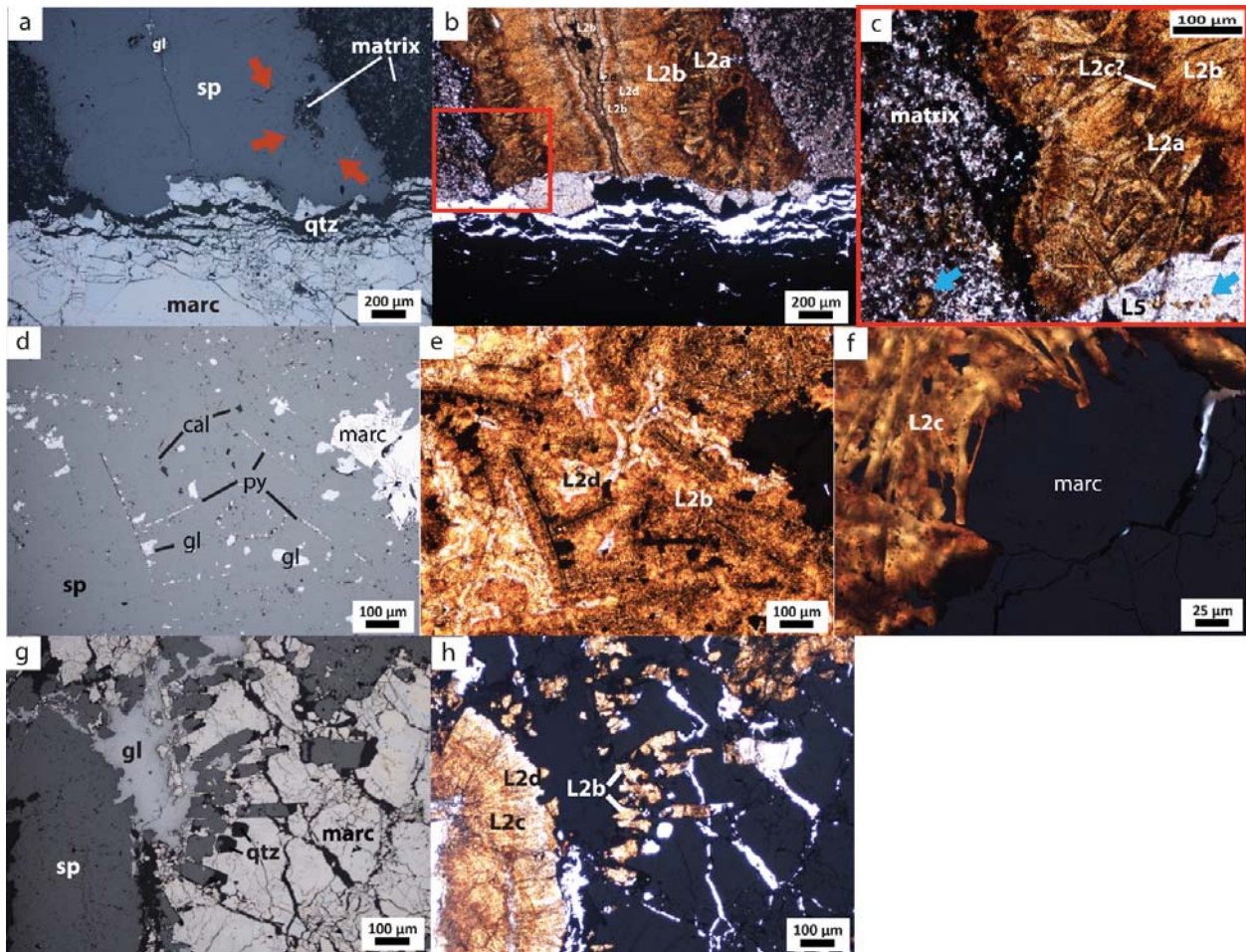


Figure 12. (a) Reflected light and (b, c) transmitted light photomicrographs of sample 923 – 2373.4a showing matrix material surrounding sphalerite L2 vein. (a) Sphalerite L2a contains linear inclusions (shown with red arrows). Galena (gl) is located at the center of the banded vein. (a, b) L2 and the matrix are cut by later sphalerite L5, quartz, and marcasite. (c) A closer look at (b) (shown with a red box) shows a rim of dark material which commonly occurs along the sphalerite L2 margin and sphalerite is sparse along this margin. Sphalerite L2 is hosted in L5 and the

matrix (blue arrows). (d) Reflected light and (e) transmitted light photomicrograph of sample 923 - 2251.2a showing bladed sphalerite L2b and sphalerite L2d (bright cream zone). The L2b sphalerite is seen as replacing large (up to 600 μm in length) blades. Inclusions of calcite (cal), pyrite (py), and galena (gl) are seen throughout the L2b sphalerite. (f) Transmitted light photomicrograph of fibrous L2c replacing marcasite. (g) Reflected light and (h) transmitted light photomicrographs of fibrous sphalerite L2c and bladed L2b replacing marcasite. Quartz is occasionally present in the bladed replacement and fibrous L2d rims the L2c.

Where spherical sphalerite L1 is present, sphalerite L1 gradually grades into sphalerite L2b (Figure 13, far right). Sphalerite L2b lacks a fibrous texture, is typically a burnt orange color, and was observed following sphalerite L2a in banded sphalerite veins (Figure 12b, 12c). In addition, sphalerite L2b also occurs as coarse (~ 50 to $100\mu\text{m}$ in width) blades (Figure 12e, 12h) which sometimes contain aligned inclusions (Figure 12d), similar to that of sphalerite L2a (Figure 12a). In some areas, the sphalerite blades clearly replace marcasite (Figure 12g). In these areas, sphalerite L2b is sometimes heavily mottled by opaque submicron grains (Figure 12e).

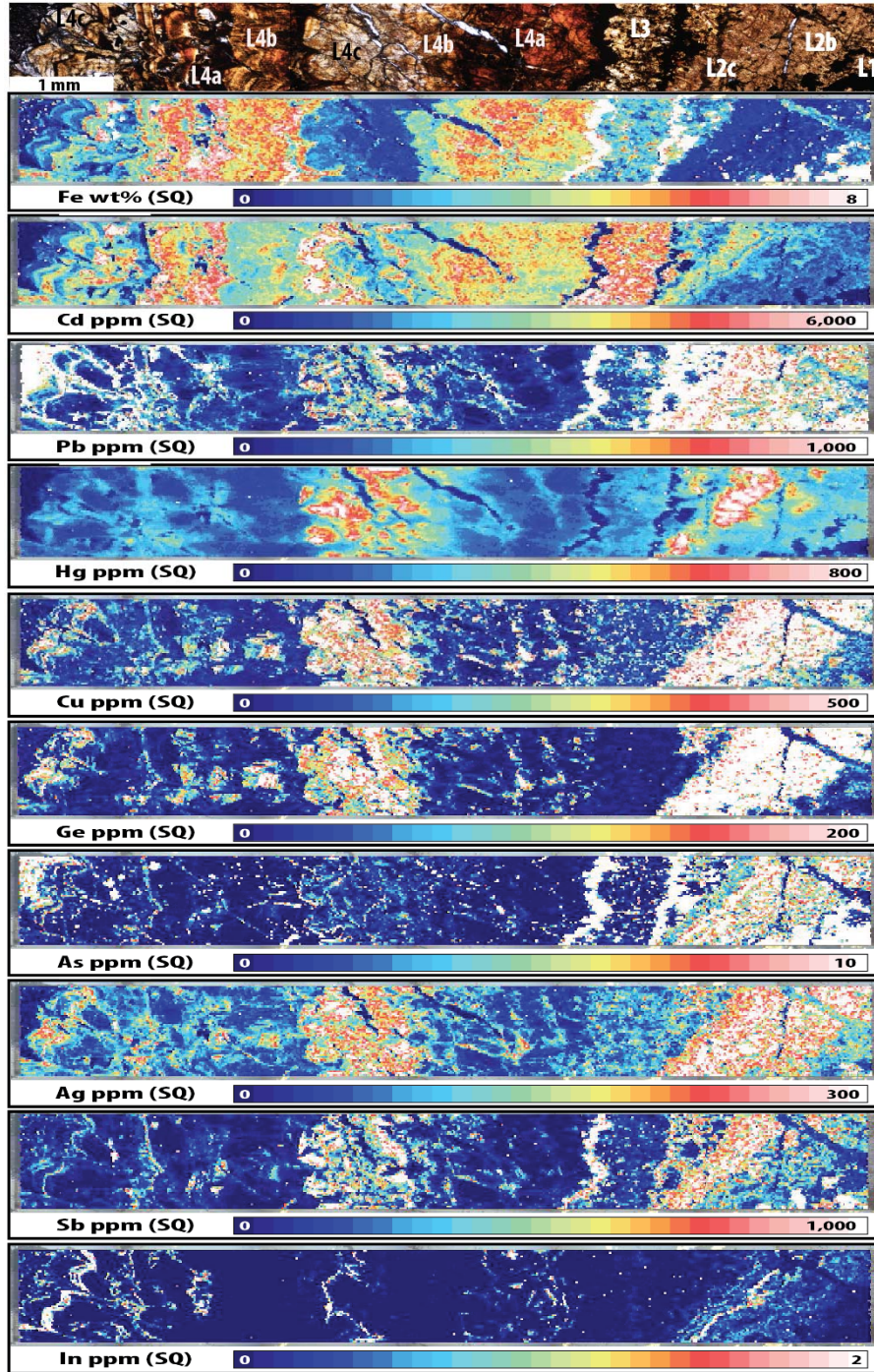


Figure 13. Mosaic of transmitted light photomicrographs showing the relationship between the colloform banded sphalerite textures in sample 923 – 2277.6a. Corresponding quadrupole laser ablation maps show the spatial distribution of trace elements throughout the sphalerite generations. Sphalerite L2 contains Cd, Pb, Hg, Ce, Ge, As, Ag, Sb, and In. Cadmium, Hg, and Sb are more concentrated in the later L2c sphalerite. Sphalerite L3 contains low Fe, Hg, and Ag and increased Cd. Patches of Pb, Cu, As, and Sb are minimally present in L3. Earlier sphalerite L4a and L4b preferentially contain increased Fe and Cd concentrations, however, Pb, Hg, Cu, Ge, Ag, and Sb are concentrated in later sphalerite L4c. Lead is also seen in the matrix material and cutting into L4. Sphalerite L2 and L4c show decreased Fe and increased Pb, Hg, Cu, Ge, As, Ag, and Sb.

Sphalerite L2b sometimes grades into sphalerite L2c (Figure 13). Sphalerite L2c is a very fine fibrous variant of sphalerite L2b (Figure 12f, 12h) with similar burnt orange colors. In L2 veins, sphalerite L2b and L2c are interchangeably present following sphalerite L2a depending on the presence of the L2c fibrous texture which is sometimes difficult to determine (Figure 12c).

The sphalerite L2 generation ends with a white to light cream colored zone (sphalerite L2d; Figure 12b, 12e, 12h). In areas where bladed sphalerite L2b is present, sphalerite L2d occurs as a thin rim on the same texture (Figure 12e). In areas where non-fibrous sphalerite L2b and fibrous sphalerite L2c are present, sphalerite L2d still occurs as a thin zone, however, it can be fibrous with a texture similar to that of sphalerite L2c (Figure 12h).

In thin sections from sample 923-2373.4', the sphalerite is surrounded by a matrix of sphalerite, pyrite, galena, quartz, and organic material (Figure 12a, 12b, 12c). The sphalerite grains appear similar in color to the sphalerite L2 veins. Thin section 923-2373.4b shows sphalerite hosted in the matrix material with some apparent flow textures (Figure 14).

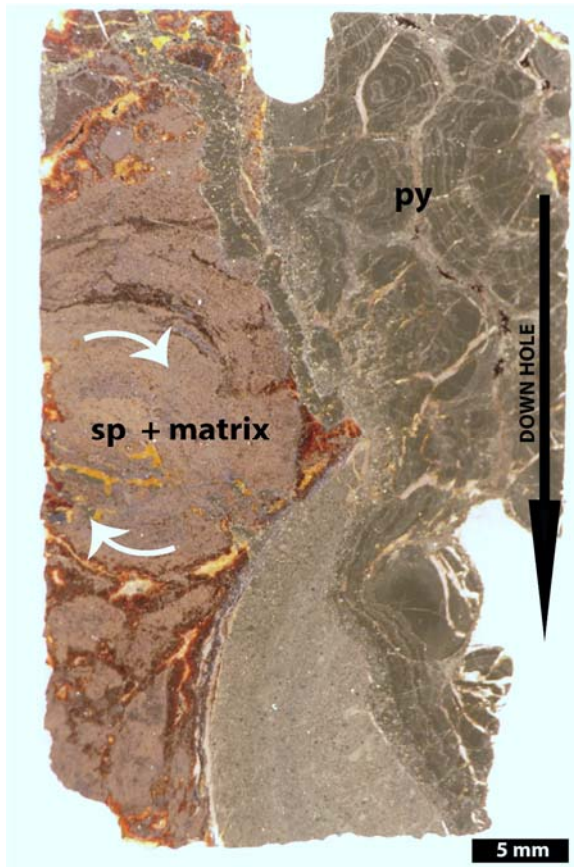


Figure 14. Thin section photograph of sample 923-2373.4b which contains sphalerite and matrix material distributed in a circular pattern which appears to mimic fluid-like flow. The sphalerite and matrix material is later cut by coarse pyrite/marcasite.

4.1.2.2 Composition determined by EPMA and LA-ICPMS

4.1.2.2.1 Chalcophile (+Fe) elements

Sphalerite L2 Zn and S concentrations determined by the EMPA range from 52.1 to 65.9 wt% and 31.4 to 34.5 wt%, respectively (Figure 6a, 7; Table 5). The mean Zn concentration increases through the paragenesis and agrees with the spatial distribution seen in LA-ICPMS Zn maps (Figure 7, 15; Table 5). Interestingly, the mean S data does not systematically vary with Zn (Figure 7; Table 5).

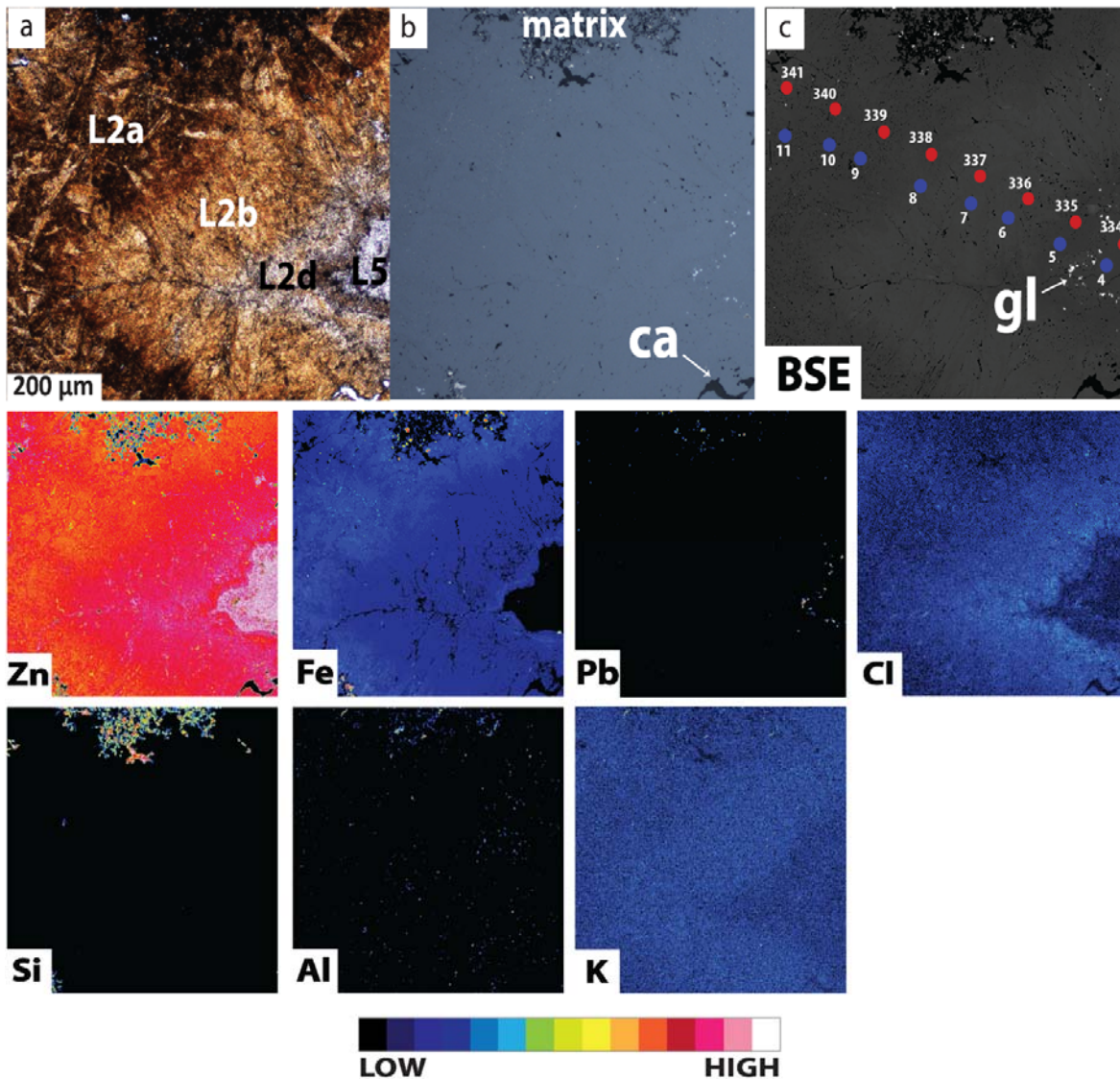


Figure 15. (a) Transmitted light photomicrograph of oscillatory zoned sphalerite L2 in sample 923 - 2373.4a. (b) Reflected light photomicrograph showing locations of cross cutting calcite and matrix material (c) BSE image of sphalerite stage L2 and inclusions of galena near the contact with later sphalerite L5. JOEL spot analyses are shown in red, CAMECA in blue. Zinc X-ray map of sphalerite shows zoning in Zn concentration. Oscillatory zoning is

faintly seen in the Fe X-ray map and correlates with the color and Zn zoning. Lead X-ray map illustrates spatial distribution of galena in the matrix and in late sphalerite L5. Chlorine X-ray map shows that Cl is not significantly concentrated in stage L2 and the zoning observed is possibly caused by X-ray continuum. Silicon X-ray map shows Si in matrix material and rare inclusions in the sphalerite. Aluminum X-ray map shows Al present in the matrix and throughout the sphalerite. Potassium X-ray map shows that K rarely occurs in the matrix.

Similar to L1 sphalerite, the minor element geochemistry in sphalerite L2 is dominated by Fe. Iron is present in all 160 of the L2 quantitative EPMA analyses (Figure 7; Table 5) and ranges in concentration from 0.68 to 12.4 wt% (Figure 7; Table 5). Sphalerite L2a and L2b have similar, higher EPMA Fe concentrations, despite their differences in color (Figure 7; Table 5). Later sphalerite textures, L2c and L2d, have lower Fe concentrations (Figure 7; Table 5).

These variations in the Fe content of L2 are not well defined in the X-ray and LA-ICPMS maps (Figure 15, 16, 17), however, zones of increased Fe are visible within L2a and at the center of the L2d phase (Figure 17). Most notable is a darker rim on the L2d sphalerite which is associated with low Fe concentrations (Figure 17).

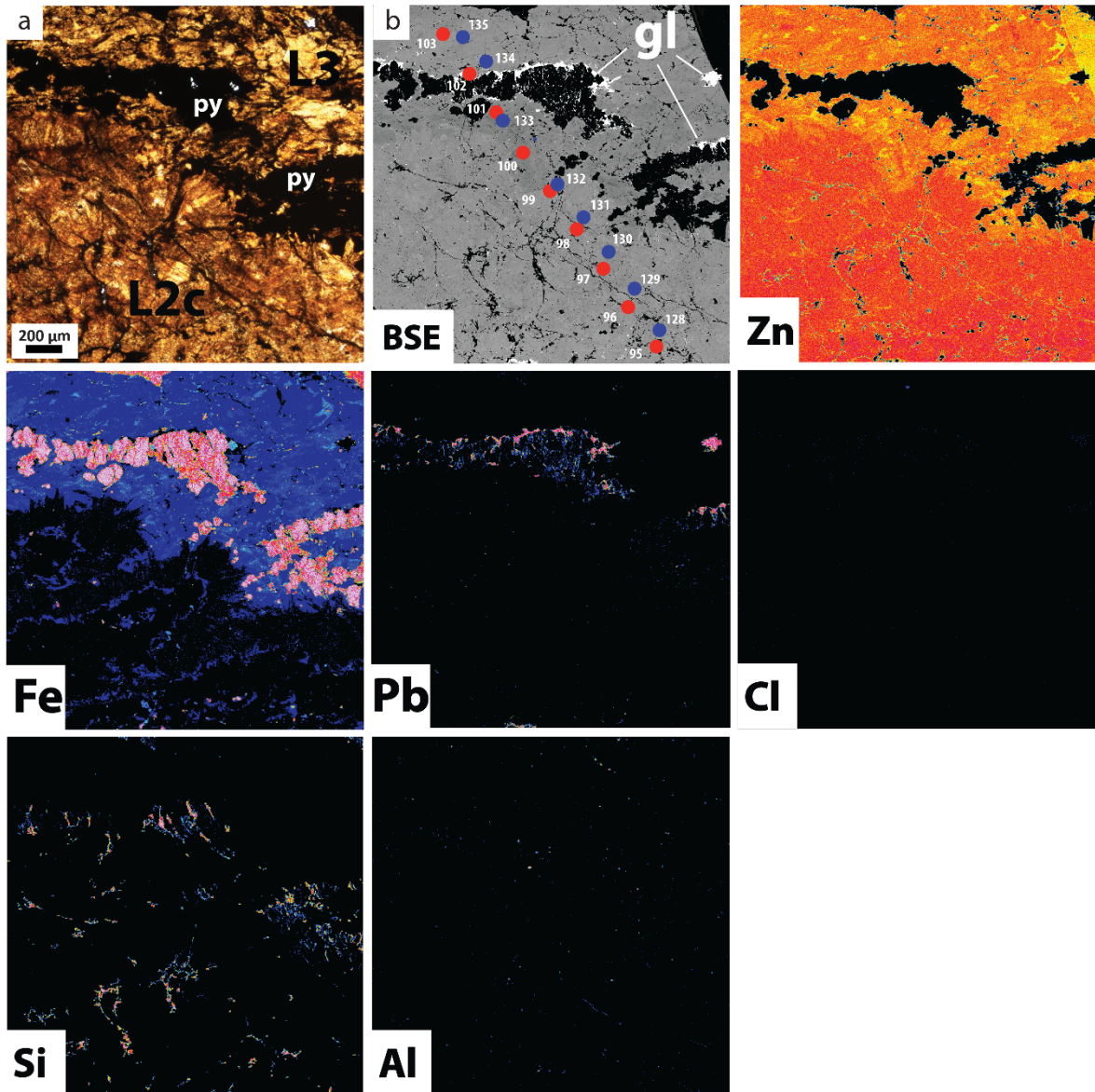


Figure 16. (a) Transmitted light photomicrograph of fibrous sphalerite L2c and patchy sphalerite L3 of sample 923 - 2277.6a which is being cut by late pyrite. A complex array of opaque micro veinlets is also seen in the sphalerite. (b) BSE image of sphalerite which shows late pyrite (black) is associated with galena (bright white). JOEL spot analyses are shown in red, CAMECA in blue. Zinc spatial distribution shows that Zn is higher in the later L3 sphalerite. Iron concentrations are higher in L3 and heterogeneously distributed in the L2c sphalerite. A fibrous texture is also seen in the L2c Fe map. Lead X-ray map also shows that galena is associated with late pyrite. Chlorine X-ray map shows that Cl is potentially present as a single fluid inclusion. Aluminum map shows rare, very fine Al. Silicon X-ray map showing significant abundance of Si micro veinlets, sometimes associated with late pyrite.

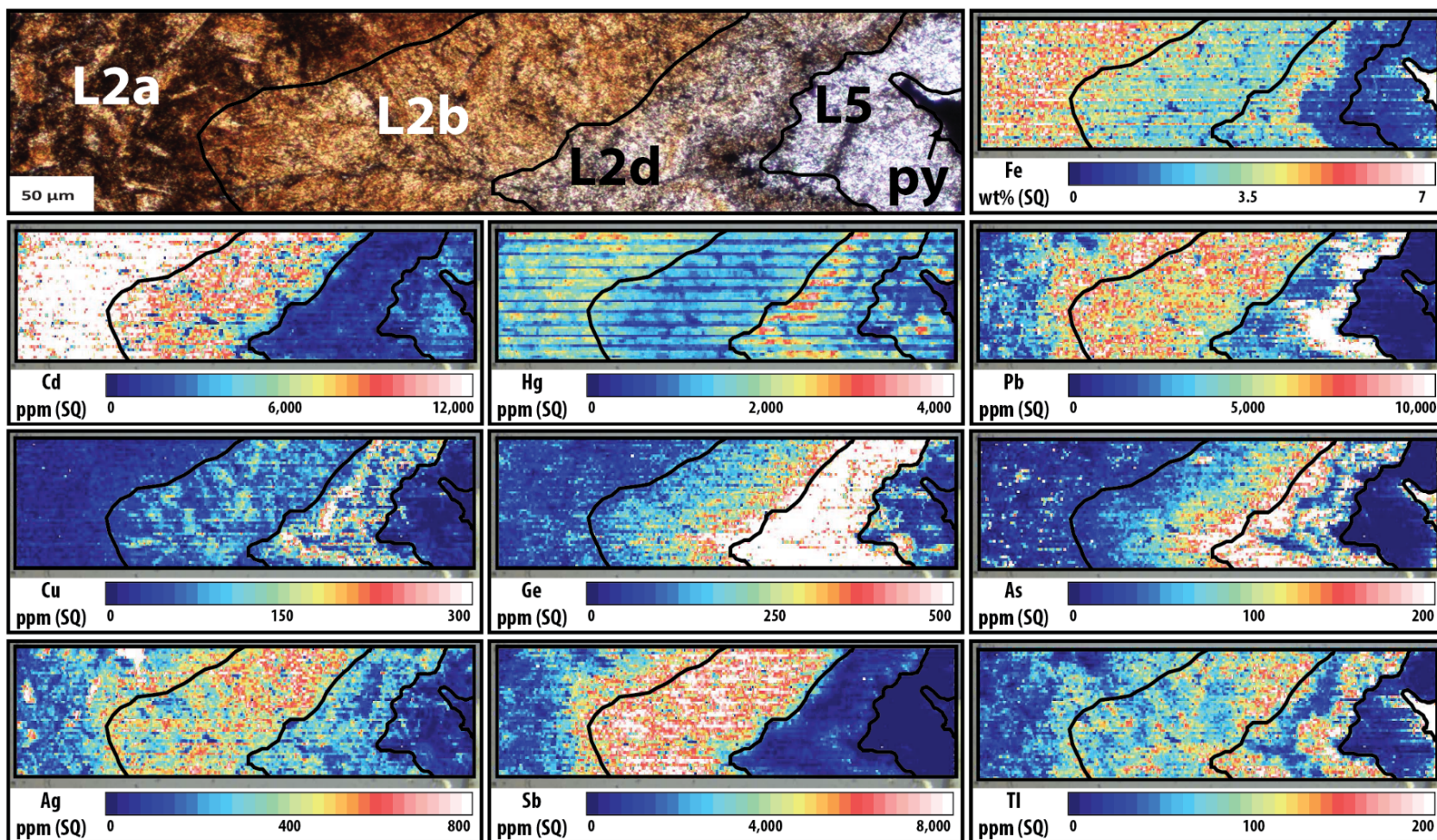


Figure 17. Quadrupole laser ablation maps of sphalerite L2 and L5 in sample 923 – 2373.4a show the spatial distribution of elements throughout the variable textures and generations. The spatial distributions have been traced out on the element maps and then overlaid on the transmitted light photomicrograph to observe the pattern of spatial distribution (shown as black lines). Earlier sphalerite L2a is rich in Fe, Cd, and Hg. It also contains patchy Ag. Sphalerite L2b contains less Fe and Cd, and is rich in Pb, Ag, Sb, and patchy Cu and Tl. Sphalerite 2d is rich in Cu, Ag, and As, however zoning is present along the contact between lighter and darker L2d. The lighter zone preferentially contains Fe, Hg, and As. The darker tips of L2d are richer in Pb and Tl. Sphalerite L5 contains minimal trace elements in relation to earlier L2, however, patchy Cd, Hg, and Ge are present.

Iron and Zn concentrations in the L2 sphalerite are weakly negatively correlated (Figure 6b). This relationship is confirmed by the maps of the two elements (Figure 15h, 16c, 17).

Cadmium was detected in 158 of the 160 L2 EPMA analyses (Figure 7; Table 5) and ranges in concentration from 0.05 to 1.19 wt%. The Zn and Cd data are negatively correlated for some analyses from this phase, however, a subset of the data has much higher Cd concentrations which are decoupled from this systematic relationship with Zn (Figure 6c, 7). The quantitative data and LA-ICPMS maps show that the higher Cd values are mostly hosted in sphalerite L2a with high values in L2c (Figure 7, 17, 18; Table 5). Cadmium concentrations are very low in L2d (Figure 7, 17; Table 5).

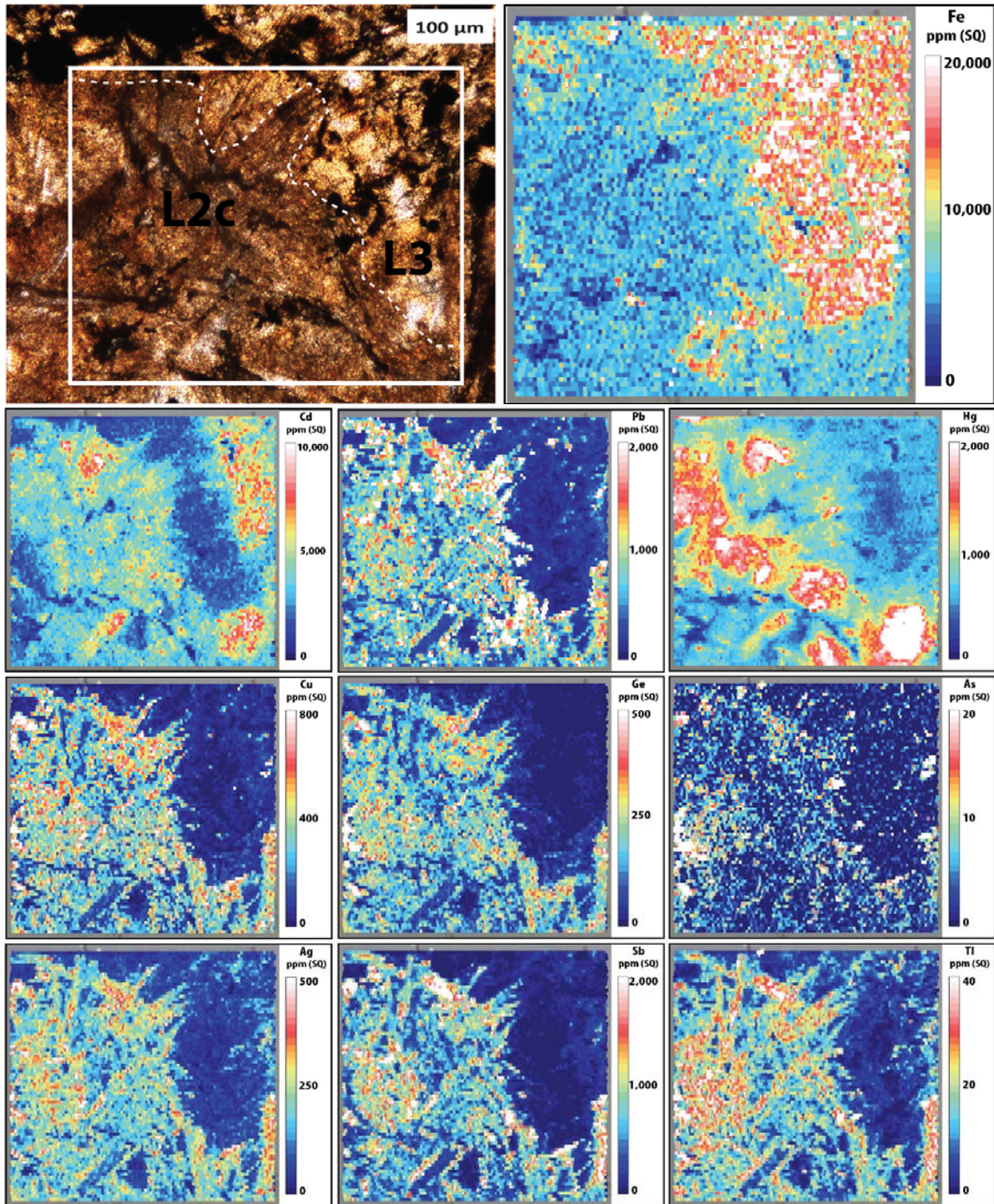


Figure 18. Quadrupole laser ablation element maps show the spatial distribution of elements present in fibrous sphalerite L2c and later sphalerite L3 in sample 923 – 2277.6a. The white box on the photomicrograph shows the mapped area. Lead, Cu, Ge, Ag, Sb, and Tl are preferentially distributed in L2c and the fibrous texture is evident in these maps. Cadmium displays heterogeneity and is present in both textures, but absent along the boundary between the two stages. Mercury is also heterogeneous and preferentially is located in the earlier L2 sphalerite. Arsenic is heterogeneous and is likely associated with very fine pyrite inclusions in L2c.

Overall, sphalerite L2 has higher Hg concentrations (Figure 7). Like Cd, Hg is found in higher concentrations in sphalerite L2a and the 87 EPMA analyses have a range from 0.03 to 0.23 wt% (Figure 7; Table 5). Mercury is preferentially present in the lighter L2d area in LA-ICPMS maps and the Hg and Fe spatial distributions in L2 are in strong agreement (Figure 17). The heterogeneity of Hg present in LA-ICPMS maps of L2c is very similar to the spatial distribution of Cd also seen in this texture (Figure 18).

Visible galena inclusions are present in sphalerite L2, are commonly hosted in the matrix material (Figure 15), late stage bands of L2 veins (Figure 12a, 15), and are associated with late stage pyrite in L2c (Figure 16). Lead is frequently (n=54) quantitatively present in the earlier L2 sphalerite at concentrations from <0.01 to 0.72 wt% (L2a, L2b, and L2c; Figure 7; Table 5). Element mapping shows that Pb is mostly present in L2b, L2c, and the darker rim of L2d (although this may be saturation caused by the galena inclusions; Figure 17, 18). The spatial distribution of Pb in L2d is the opposite to that of the Fe and Hg distribution (Figure 17). The spatial distribution of Tl in L2 mirrors the behavior of Pb in all of the textures including the variability in L2d and the fibrous nature of L2c (Figure 17, 18).

Copper is quantitatively present at very low concentrations ranging from 0.01 to 0.21 wt% (n=30) in concentration in sphalerite L2 EPMA analyses (Figure 7; Table 5). The Cu maps show that Cu is present in L2b, L2c, and L2d (Figure 17, 18). The Cu spatial distribution in sphalerite L2b is heterogeneous but mimics a fibrous texture similar to sphalerite L2c (Figure 17, 18). Copper present throughout L2d seems to have a weak zonation (Figure 17).

Antimony was quantitatively analyzed in 132 L2 EPMA spots, occurs in higher concentrations in L2 than any other generation of sphalerite, and ranges from 0.01 to 0.76 wt% (Figure 7; Table 5). The Sb maps show that Sb is more abundant in the L2b and L2c textures (Figure 17, 18).

Silver was detected in 21 EPMA analyses of L2 and was not present in the EPMA data for L2d (Figure 7; Table 5). Trace element mapping reveals that Ag is mostly present in L2b and L2c sphalerite, however, inclusions of Ag are present in L2a and L2d (Figure 17, 18).

Arsenic was not present above the EPMA LOD in any of the Anarraaq sphalerite textures, however, in the elements map, high As values are observed in L2d in growth zones similar to those seen in Cu and Ag (Figure 17).

4.1.2.2.2 *Lithophile elements*

Sodium was detected in 72 quantitative spots by EPMA and mapped by LA-ICPMS. It decreases in concentration through the four L2 textures (Figure 10, 19, 20; Table 5). Although high Na inclusions (likely fluid inclusions) are present in the maps, there also appears to be a homogenous spatial distribution of Na in the sphalerite (Figure 19, 20). This can be better observed in log scale maps of Na (Figure 19, 21). There is also a strong negative correlation between the Zn and Na concentrations and strong positive correlation of Na and Fe evident in the quantitative data (Figure 6e, 6g).

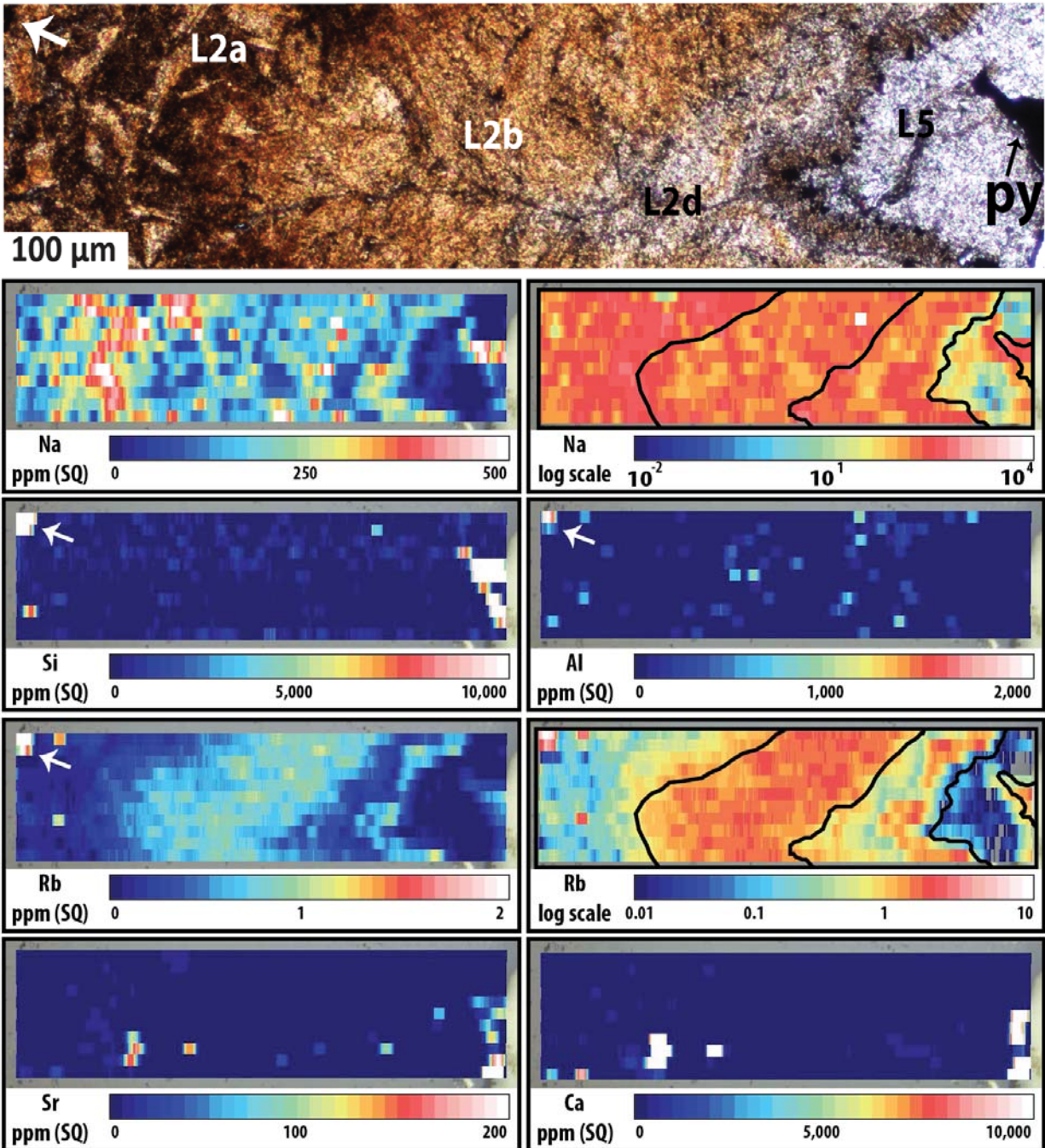


Figure 19. Quadrupole laser ablation trace element maps of lithophile elements distributed in sphalerite L2 and L5. Sodium appears homogeneous throughout the L2 textures but is not present in later L5 sphalerite. Silicon and Al are less common and an area in the top left corner of the maps (white arrow) contains Si, Al, and Rb and appears similar to the opaque matrix material. The Rb map also shows a homogeneous spatial distribution in sphalerite L2b and the darker tips of L2d. This spatial distribution is better illustrated on a log scale map of Rb. Strontium and Ca are associated with the late pyrite and are also seen cross cutting the sphalerite along a micro veinlet. Sodium, Si, and Rb are also associated with the pyrite.

Chlorine was quantitatively present in 41 EPMA spots (0.01 – 0.18 wt%; Figure 10; Table 5), and was not significantly present in X-ray maps (Figure 15, 16). There is no systematic relationship between Na and Cl concentrations in this stage of sphalerite (Figure 6f).

The spatial distribution of Rb in this stage is very similar to that of Na. Abundant spots of relatively high Rb concentrations are present in the L2 LA-ICPMS maps (Figure 19, 20, 21). Many of these spots also have higher Si and Al values (e.g. sphalerite L2a in the top left corner of the Rb, Si, and Al maps in Figure 19). More homogeneously distributed Rb is present in sphalerite L2b, L2c, and in the dark growth zone of L2d (Figure 19, 20, 21). Rubidium is also seen present in the late pyrite (Figure 19).

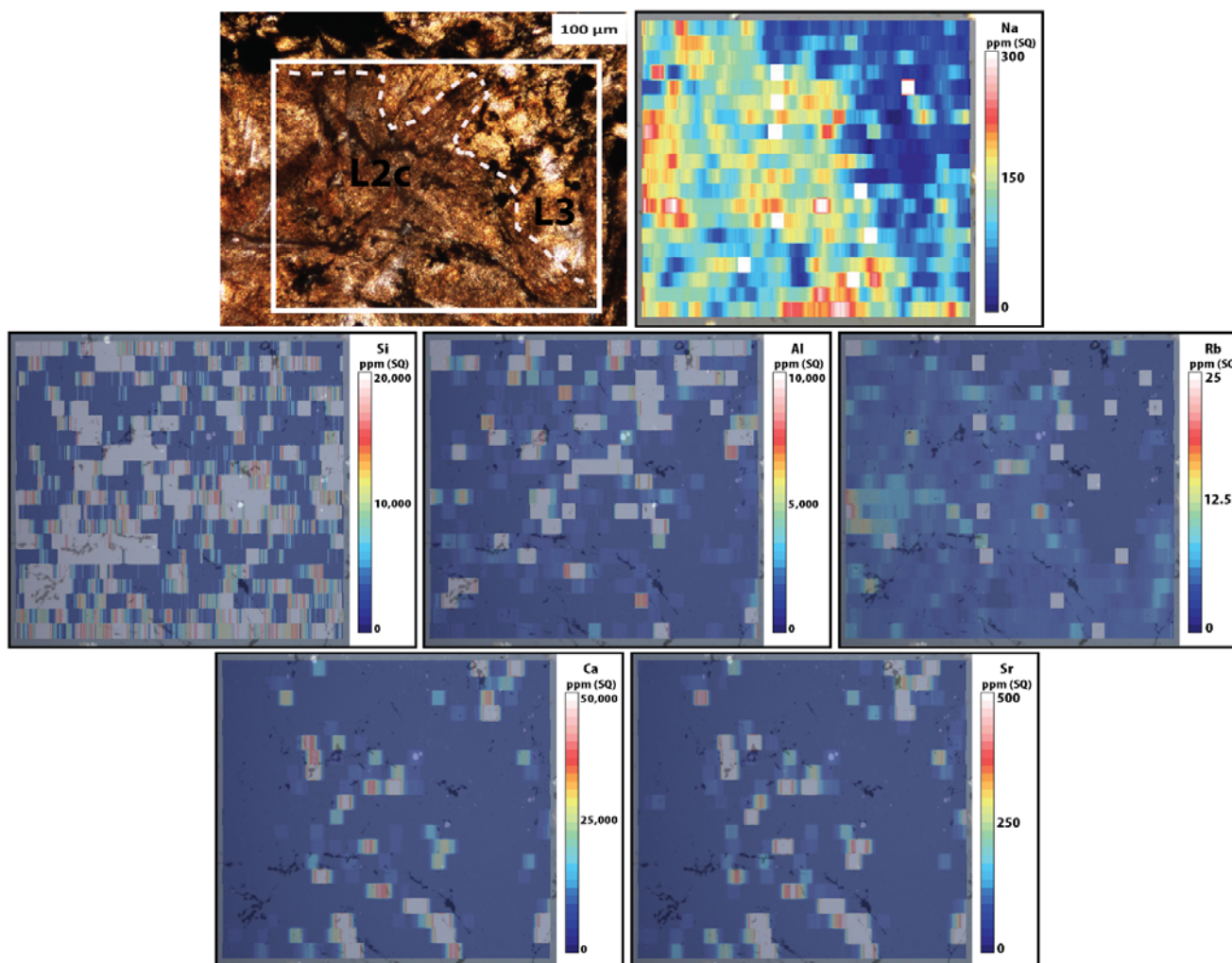


Figure 20. Quadrupole laser ablation element map show the spatial distribution of lithophile elements present in sphalerite L2c and L3. The white box on the photomicrograph shows the mapped area. The maps have been overlaid on a reflected light photomicrograph of the area which was taken prior to the mapping. Sodium is preferentially located in L2c and appears homogeneous in this sphalerite. Silicon is heterogeneous and abundant in both textures. Aluminum, Rb, Ca, and Sr are heterogeneous and Ca shows an identical spatial distribution to Sr present.

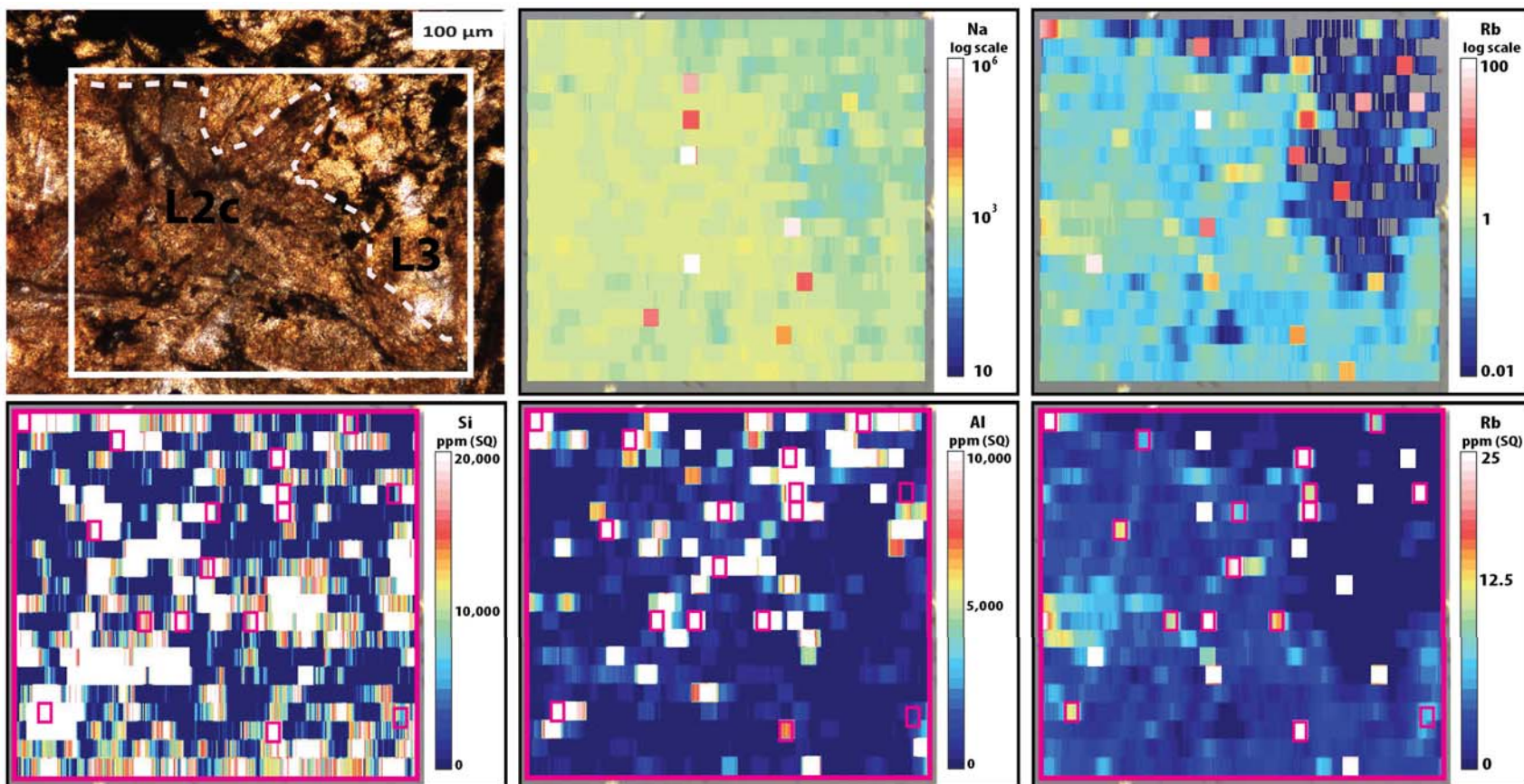


Figure 21. Sphalerite L2c lithophile LA-ICPMS maps continued. The white box on the photomicrograph shows the mapped area. A log scale view of Na and Rb from Figure 20 shows the homogenous spatial distributions in the fibrous L2c texture. Additionally, a comparison of spots in the Si, Al, and Rb maps show that roughly half of the Rb spots spatially correlate with Al and Si also present (the pink boxes are where spots are present amongst all three of the maps).

With the exception of a few spots, Si typically does not spatially correlate with the other lithophile elements, which suggests that the high values may come from quartz inclusions (Figure 16, 19, 20, 21).

The spatial distribution of Sr is decoupled from Rb and the areas of relatively high concentration spatially correlate with Ca (Figure 19, 20). Calcium is quantitatively present in EPMA spot analyses more in sphalerite L2 than any other texture (10 of 15 spots in which Ca was detected above the LOD; Figure 10; Table 5).

4.1.3 Sphalerite L3

4.1.3.1 Petrography and Texture

Sphalerite L3 is a less abundant type of sphalerite at Anarraaq and has a golden yellow color and a patchy texture which is mottled with opaque inclusions (Figure 13, 22). The majority of sphalerite L3 is represented by a colloform band typically 600-800 μm in width which postdates fibrous sphalerite L2c (Figure 13, 16a, 22).

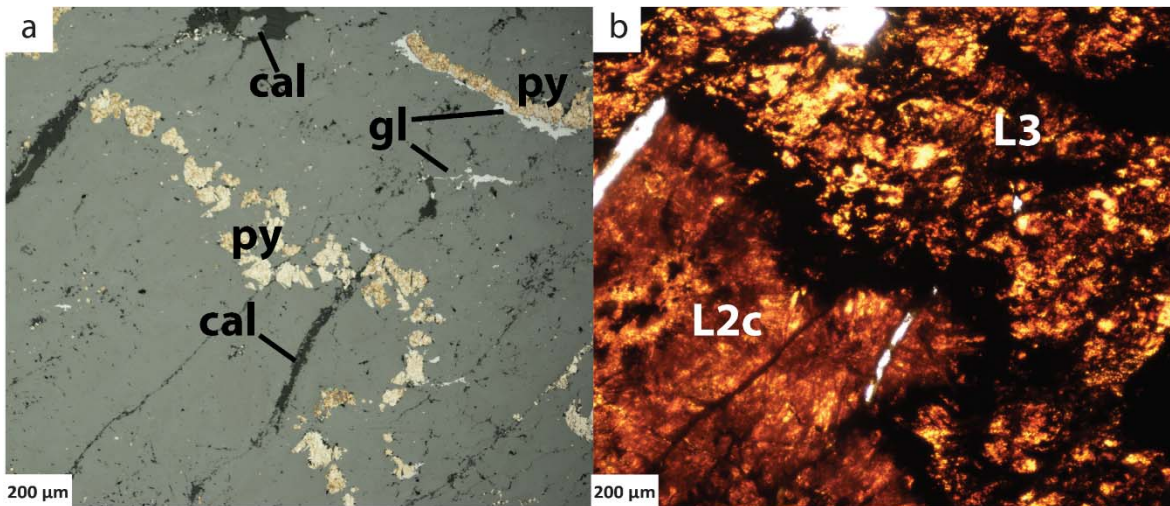


Figure 22. (a) Reflected light photomicrograph shows pyrite, galena, and calcite in the L3 sphalerite. The calcite veins post-date the sphalerite. (b) Transmitted light photomicrograph showing the patchy nature of sphalerite L3. White box represents the area of Figure 23, 24, and 25.

4.1.3.2 Composition determined by EPMA and LA-ICPMS

4.1.3.2.1 Chalcophile (+Fe) elements

Zinc and S were analyzed by EMPA in 20 sphalerite L3 spots and concentrations range from 58.6 to 64.9 and 31.9 to 33.2 wt%, respectively (Figure 7, Table 5).

Iron was detected in all 20 analytical spots and has a higher concentration than in the L2c texture despite the fact that L2c is darker in color in transmitted light (Figure 7, 13, 16a, 18, 22b; Table 5). Sphalerite L3 Zn and Fe EPMA data are negatively correlated (Figure 6b). An increase in Fe concentration is also seen in lighter, brighter areas which are free of the abundant inclusions in the element maps (Figure 23, 24).

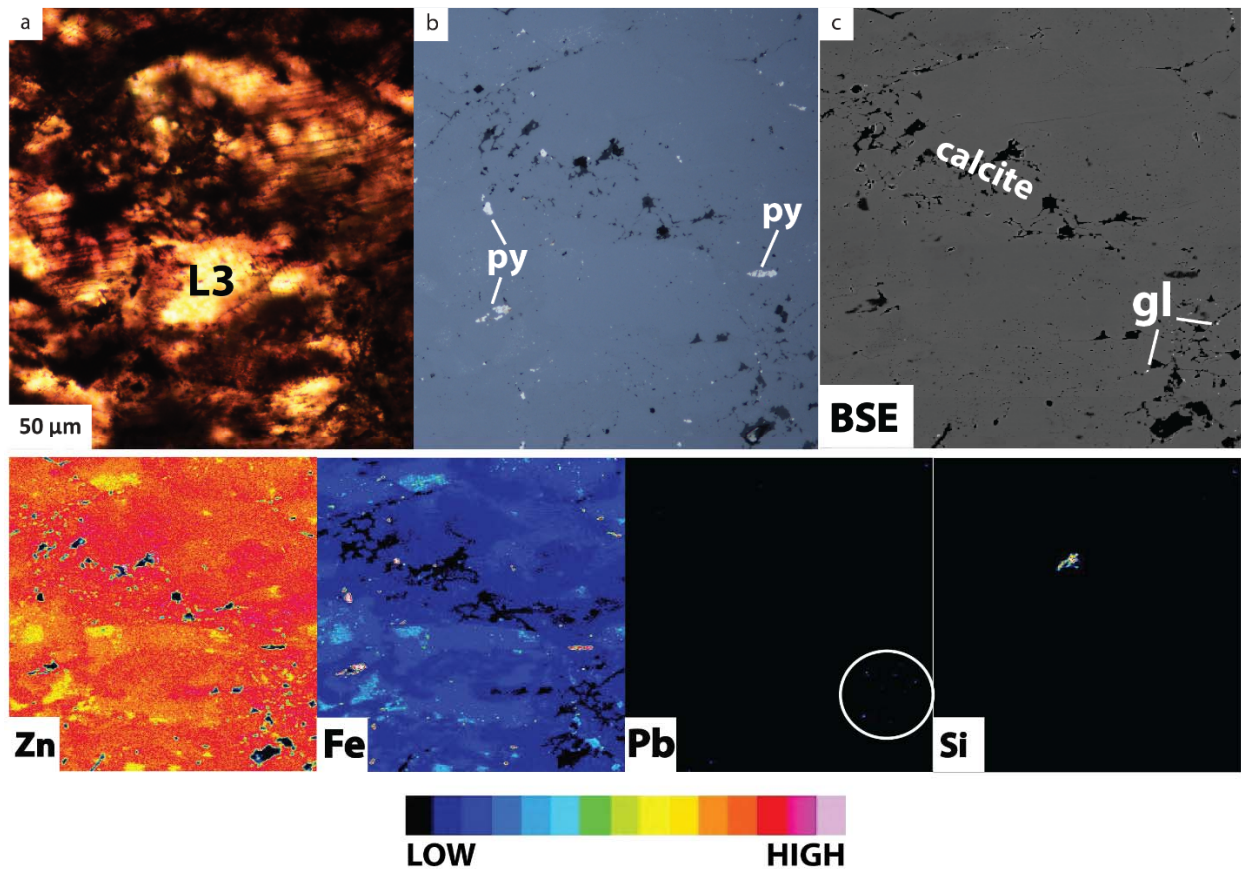


Figure 23. (a) Transmitted light and (b) reflected light photomicrograph of sphalerite L3 of sample 923 2277.6b. Opaque inclusions are present at depth in the sphalerite. (c) BSE image of sphalerite which shows calcite (black) spatially associated with the opaque areas. Galena (bright white) is also present and associated with the calcite. Zinc map shows that the Zn concentration is variable in L3 sphalerite. The Fe concentration is heterogeneously distributed in the L3 sphalerite and the increased Fe spatially correlates with the areas of decreased Zn. Pyrite inclusions appear as pink in the Fe map. Lead X-ray map shows that galena is only present in the same area identified in the BSE (white circle). Silicon x-ray map showing single inclusion of silicon associated with the calcite.

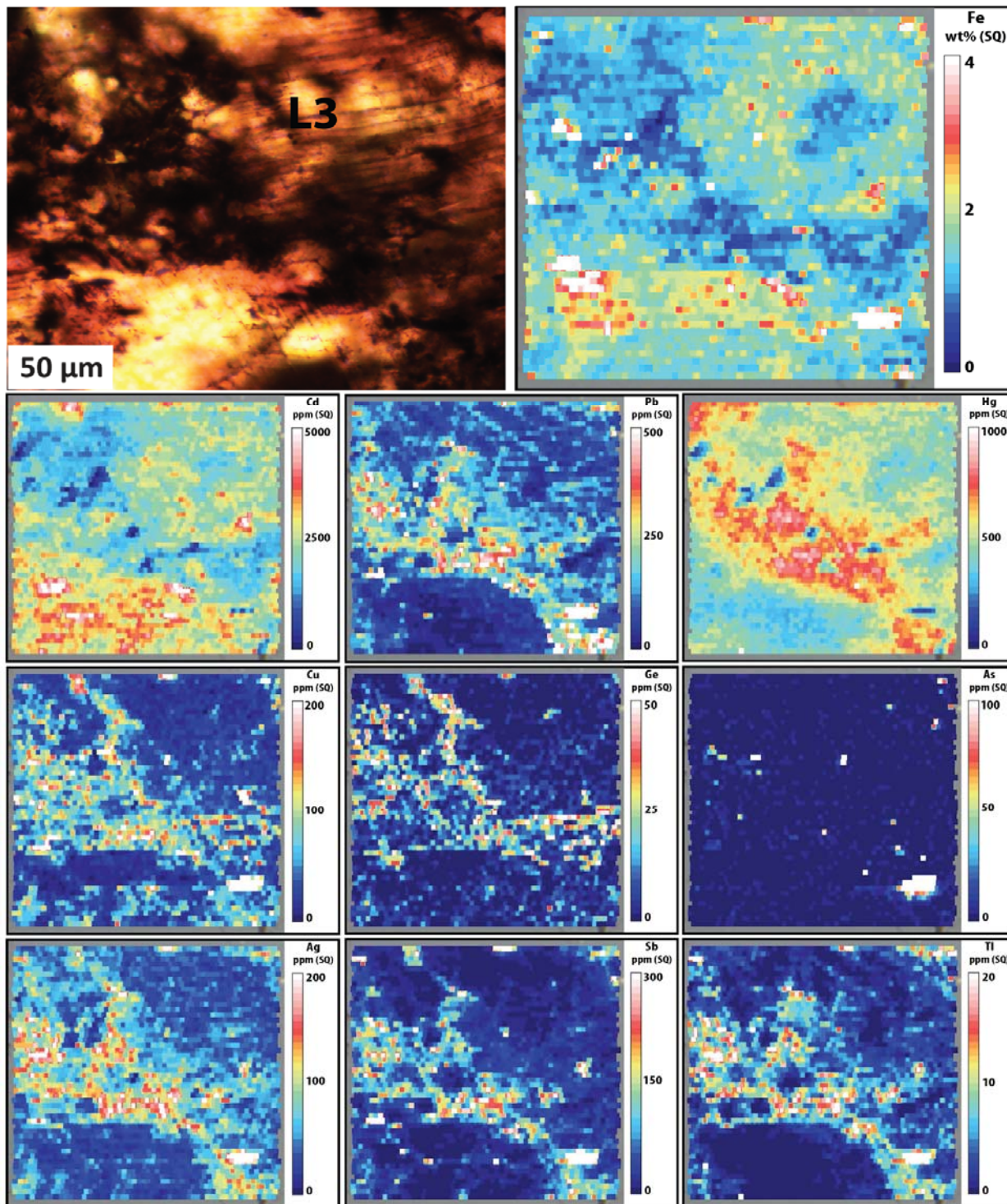


Figure 24. Quadrupole laser ablation maps of sphalerite L3 in sample 923 – 2277.6b show that the opaque inclusion area is lower in Fe and Cd content and higher in Pb, Hg, Cu, Ge, As, Ag, Sb, and Tl.

Like Fe, Cd was detected in all the quantitative spots and has lower concentrations than the L2 stage (Figure 7, 13; Table 5). In the maps, as with Fe, Cd is found in the areas of inclusion free, yellow sphalerite (Figure 24). Although the Zn and Cd EPMA data show a negative correlation and the Cd and Fe data show a positive correlation, the correlations are weak (Figure 6c, 6d).

Aside from Fe and Cd, trace element concentrations are lower in sphalerite L3 than the other generations of sphalerite (Figure 13). Although Pb was only present in 1 of the 20 EPMA spots, abundant galena is seen in the sphalerite which is associated with pyrite (Figure 16a, 22). Additionally, ~1 μm inclusions of galena are present in the sphalerite (Figure 23). Lead is also present in trace concentrations in inclusion rich sphalerite L3 (Figure 24).

Mercury was present in 12 of 20 L3 EPMA spots and although the concentrations are much lower than in L3 sphalerite, the concentration is higher in areas where Pb also increases and the Fe and Cd contents are lower (Figure 24).

Copper and Ag were not present in the EPMA analyses of this stage of sphalerite and Sb concentrations are also low (Figure 7; Table 5). Despite this, these elements display a trace concentration spatial distribution in the LA-ICPMS element maps which is very similar to the Pb and Hg previously discussed (Figure 24). Germanium was not analyzed by EPMA and has a spatial distribution similar to Pb, Hg, Cu, and Ag (Figure 24). Arsenic in this generation correlates with the presence of pyrite, which is easily identified by areas of high Fe concentrations (Figure 24).

4.1.3.2.2 *Lithophile elements*

Sodium is present in moderate to low levels (relative to other textures) <0.54 wt% and is also negatively correlated with Zn. Sodium, however, is only present above LOD in 6 of the 20 analytical spots (Figure 6e, 10). Aside from Na, lithophile elements were not detected in this stage using EPMA (Figure 10). In the LA-ICPMS element maps, Sr is spatially associated with calcite (Figure 23, 25). A few inclusions of Si, Al, and Rb are also present in the maps, however, these elements do not occur together (Figure 25). Silicon was identified in one quartz inclusion (Figure 23, 25).

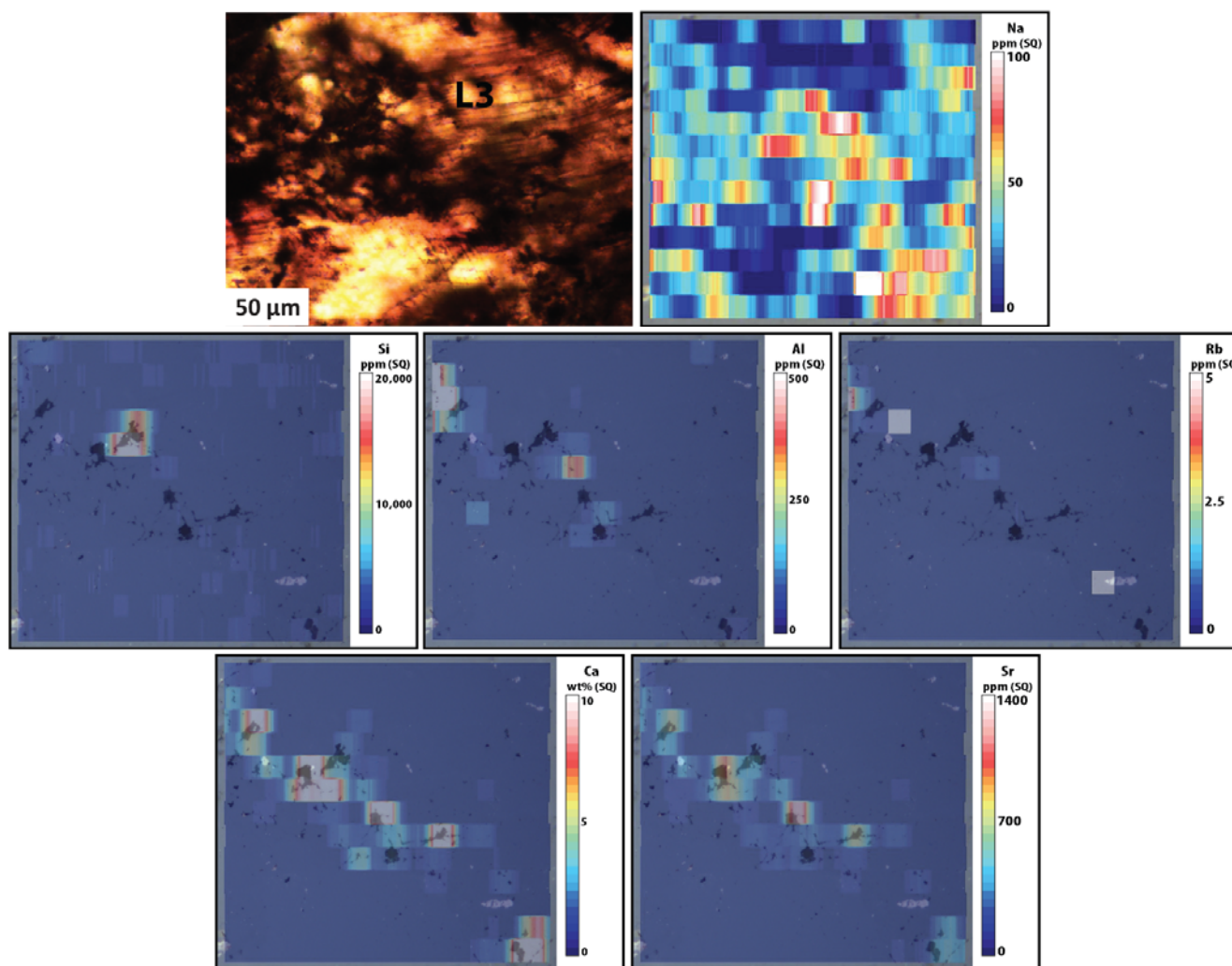


Figure 25. Quadrupole laser ablation element maps show the spatial distribution of lithophile elements present in sphalerite L3. The maps have been overlaid on a reflected light photomicrograph of the area which was taken prior to the mapping. Sodium is concentrated in the inclusion rich areas. Silicon is rarely present and associated with the calcite. Aluminum and Rb also show a similar orientation to the calcite and the two maps show little spatial correlation. Strontium is present in the calcite.

4.1.4 Sphalerite L4

4.1.4.1 Petrography and Texture

Along with sphalerite L2, the L4 stage is common in the lower ore zone of the Anarraaq deposit and it shows a wide range in texture (Figure 26). Sphalerite L4 occurs as oscillatory zoned colloform banded sphalerite, veins of banded sphalerite, and blades (~1mm in length) of sphalerite (Figure 13, 26). The colloform bands are sometimes associated with spherically zoned sphalerite (Figure 26f). When sphalerite L3 is present, sphalerite L4 overgrows L3 in the colloform banding sequence and the sequence usually begins with dark reddish brown sphalerite L4a (Figure 13, 26b, 27). Sphalerite L4 also occurs as discontinuous veins with a cream to light brown L4c sphalerite precipitating initially (Figure 26d). Sphalerite blades and spheroids sometimes initially precipitate as a bright to light orange brown zone of L4b sphalerite (Figure 26f, 26h). Within the sphalerite blades, submicron inclusions of pyrite/marcasite and galena are abundant (Figure 26i). A fibrous texture of sphalerite replacing marcasite is locally observed along the edge of a sphalerite blade (Figure 26i) which is texturally comparable to the fibrous tips of sphalerite L2c (Figure 12f).

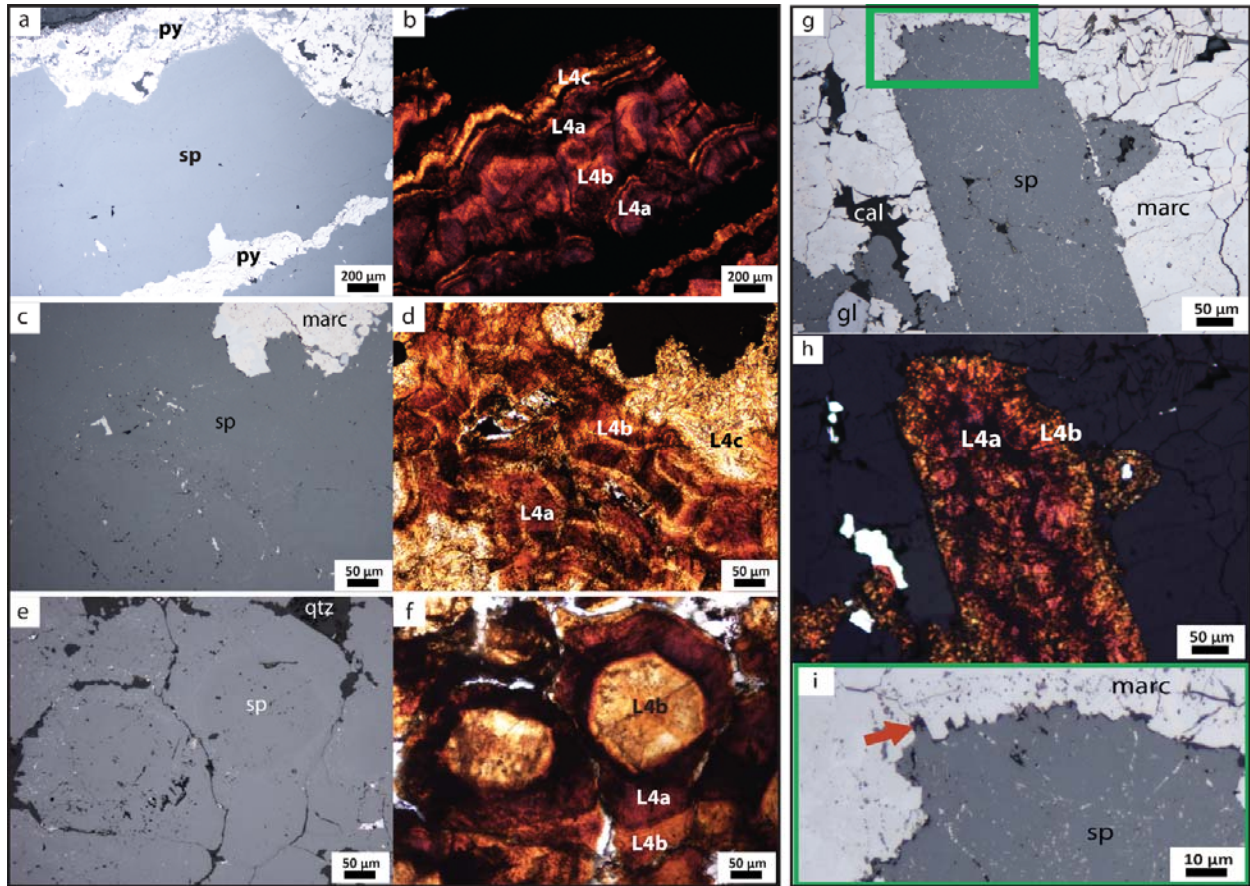


Figure 26. (a) Reflected light and (b) transmitted light photomicrograph of sample 923 – 2251.2b showing oscillating bands of sphalerite L4. The growth begins with dark reddish brown sphalerite L4a at the bottom of the sequence and ends with light tan sphalerite L4c. (c) Reflected light and (d) transmitted light photomicrograph of sample 923 – 2251.2a showing a banded vein of alternating L4a and L4b bands which is surrounded by an earlier L4c band and all of which are replacing marcasite. (e) Reflected light and (f) transmitted light photomicrograph of sample 923 – 2292.2a showing initial nucleation of a sphalerite L4b core which is then rimmed by L4a and lastly L4b. This sphalerite is associated with colloform banding and not the spherical pyrite as seen in Figure 5. (g) Reflected light and (h) transmitted light photomicrograph of sample 923 – 2251.2a showing a large (~1mm in length) sphalerite blade encased in marcasite (marc). The blade shows zoning from sphalerite L4b at the margins to sphalerite L4a in the center. (i) Higher magnification reflected light photomicrograph (exact area of image indicated in green on image (g)) shows submicron sulfide inclusions in the sphalerite. A fibrous texture is also seen along an edge of the blade (red arrow) which is texturally comparable to the fibrous texture of sphalerite L2c and indicates that the sphalerite blade is replacing the marcasite.

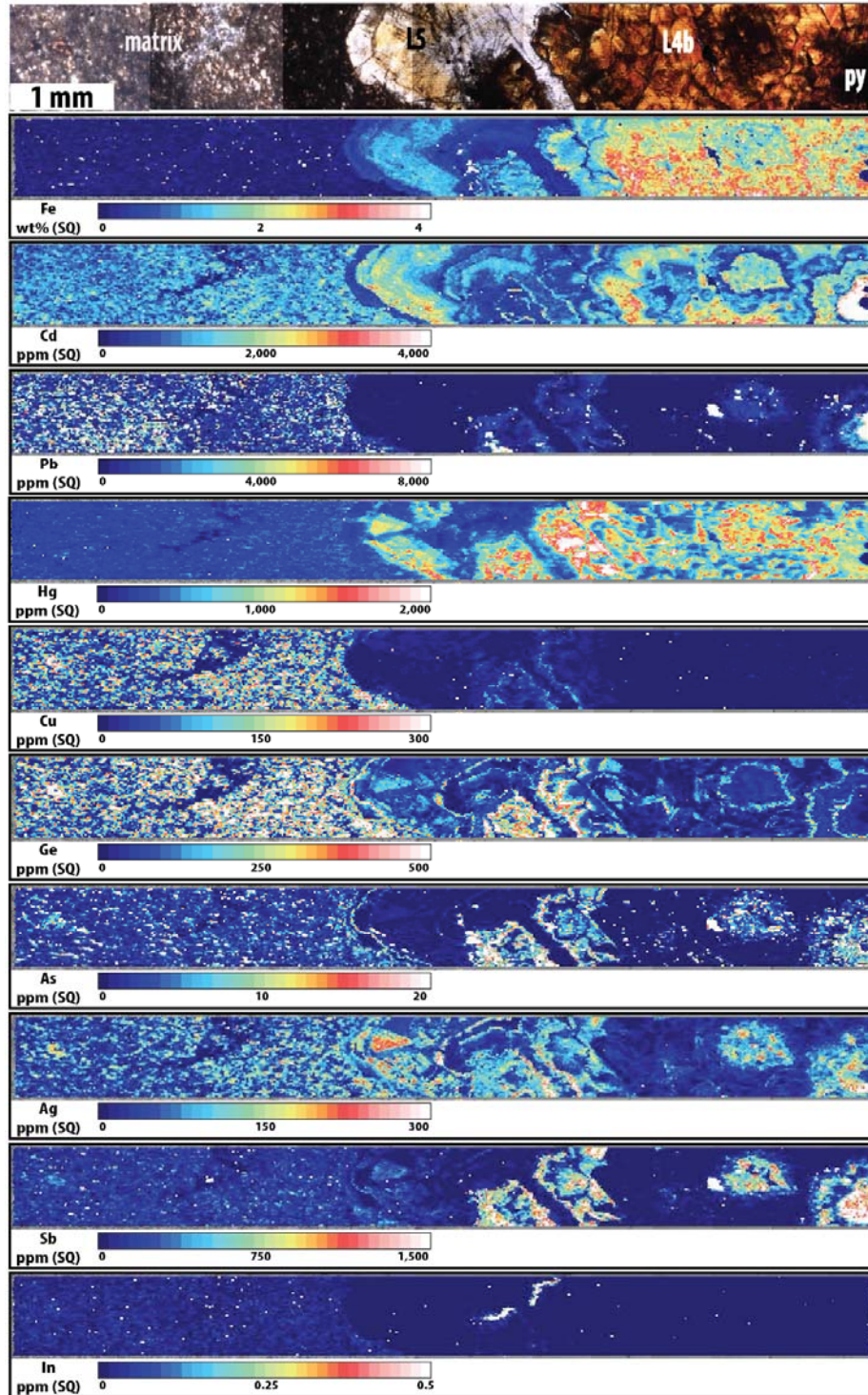


Figure 27. Mosaic of transmitted light photomicrographs show the relationship between the sphalerite L4 and L5 textures and the later matrix material. Corresponding laser ablation maps show the spatial distribution of trace elements throughout the sphalerite and matrix. Sphalerite L4 contains variable amounts Fe, Cd, Hg, As, Ag, and Sb. The majority of these elements increase toward the very end of the growth (near the L5 contact). Sphalerite L5 hosts Cd and Fe in the darker areas and Hg, Ge, and Ag also show heterogeneity in this texture. The later matrix material contains Pb, Cu, Ge, and Ag. Indium is seen along the boundary between sphalerite L4 and L5.

4.1.4.2 Composition determined by EPMA and LA-ICPMS

4.1.4.2.1 *Chalcophile (+Fe) elements*

Two hundred quantitative EPMA analyses were carried out on sphalerite L4. Sulfur has a range of values comparable to the other sphalerite generations (31.7 to 34.9 wt%), however, the Zn concentration is significantly lower (51.7 to 67.5 wt%) than in many of the other textures (Figure 6, 7). The Zn concentration increases from L4a and L4b to L4c (Figure 7, 28, 29; Table 5).

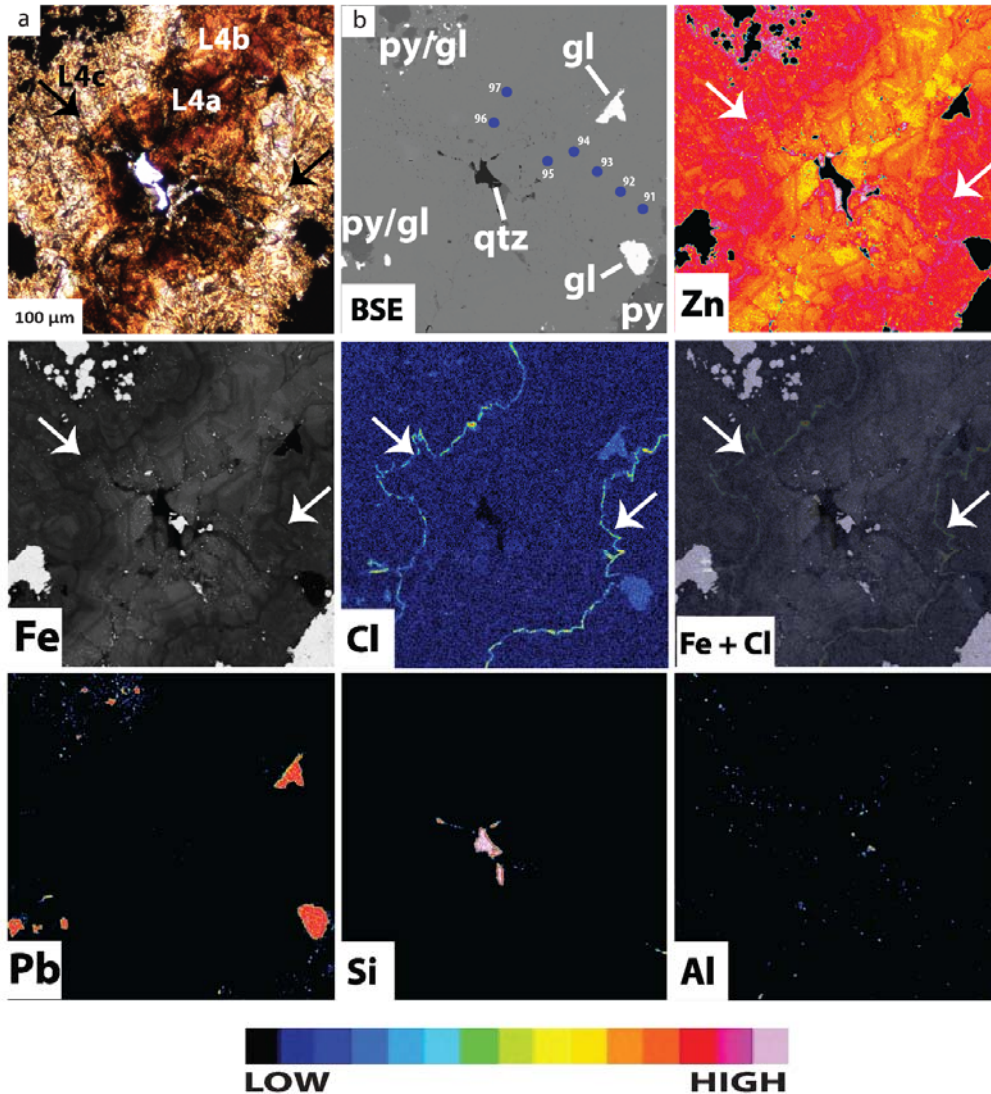


Figure 28. (a) Transmitted light photomicrograph of zoned sphalerite L4 of sample 923 - 2251.2a. (b) BSE image of sphalerite which shows partially replaced pyrite and galena as well as late quartz. CAMECA spot analyses are shown in blue. Zinc spatial distribution shows that Zn is higher in the later L4c sphalerite. Iron concentration correlates with the Zn concentration and a distinct dark zone is visible in the Fe map (white arrows). Pyrite appears as white in the Fe map. Chlorine X-ray map show that Cl is present where the dark zone appears in the Fe map (white arrows). This is better visualized when the images have been combined into a Fe + Cl image (zone shown with white arrows). The arrow location have been transferred to the photomicrograph (black arrows on (a)) to compare to the color of the sphalerite. This shows that the Cl is present along a zone that does not represent the boundary between Fe rich and Fe poor L4 sphalerite. Lead X-ray map shows that galena is mostly associated with pyrite. Silicon X-ray map showing quartz only occurs in the center of the vein. Aluminum map showing occasional Al bearing inclusions in the sphalerite.

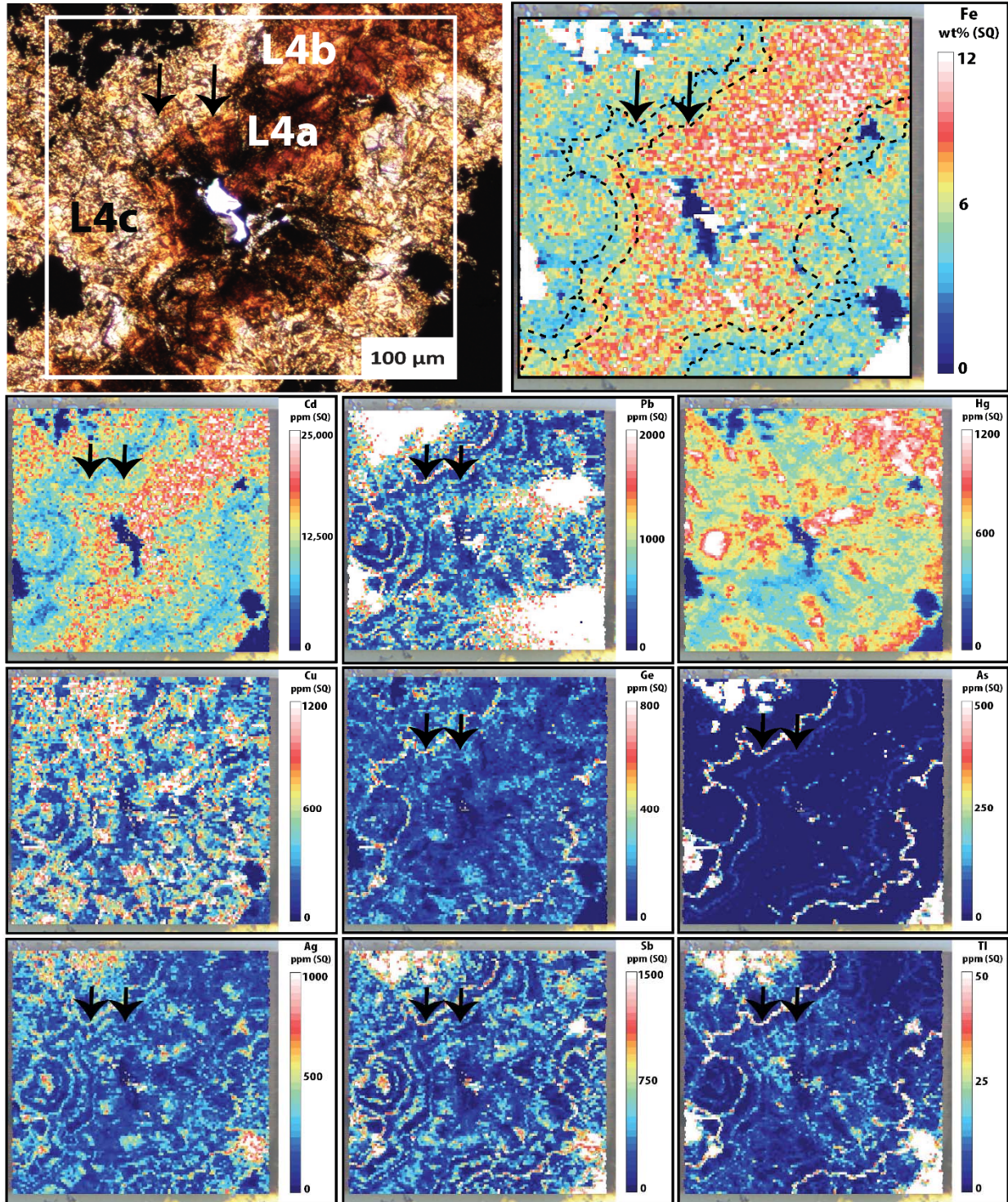


Figure 29. Quadrupole laser ablation element mapping shows the spatial distribution of elements present in a sphalerite L4 vein in sample 923 – 2251.2a. The white box on the photomicrograph shows the mapped area. The black arrows have been placed on the exact same location of the photomicrograph, the Fe map, and some of the trace element maps to show the correlation within the zones. The black lines on the Fe map represent the thin zones and have been traced out using the Sb map. Using the thin lines combined with the arrow location shows that Pb,

Ge, As, Ag, Sb, and Tl occur in the earlier (see left black arrow on these images) zone which also contains Cl (see Figure 28). Additionally, Pb, As, Ag, Sb, and Tl are also present in a less defined zone which is located at the transition from Fe poor L4c to more Fe rich L4a and L4b (see right black arrow on trace element maps, Fe map, and photomicrograph). The Cd concentration agrees with the Fe zoning. Mercury appear independent of the zoning and is heterogeneous. In addition to the zoning, Pb, Cu, Ge, Ag, Sb, and Tl are also heterogeneously distributed through the L4 sphalerite.

Contrarily, Fe concentrations decrease throughout the L4 paragenesis (Figure 7, Table 5). The relationship between Zn and Fe is best visualized in the maps of these elements (Figure 28, 29). In addition, the Fe map also shows a thin band (<10 μm) of decreased concentration which appears independent of the Zn concentration (Figure 28).

The concentrations of Cd as determined by EMPA also decrease through the L4 textures (Figure 7; Table 5), however, heterogeneity is present in the LA-ICPMS element maps (Figure 13, 29). Cadmium does have a weak negative correlation with Zn contents, however, abundant outliers are present in the EPMA data set (Figure 6c).

Similar to the other sphalerite generations, galena inclusions are present (Figure 28). The Pb LA-ICPMS map shows elevated Pb concentrations along two generations of bands (Figure 29). The outer band is more distinct and also contains lower Fe and Cd concentrations (Figure 28, 29). The inner band is less obvious and occurs near the boundary between the Fe rich L4a and L4c and the Fe poor L4c (Figure 28, 29). Lead was also found in the matrix material which is cutting sphalerite L4 (Figure 13).

Quantitative Hg was present in 142 of 200 EPMA analyses in sphalerite L4 (Figure 7; Table 5) and the maps show that Hg is elevated in L4c (Figure 13).

EMPA data on Cu in L4 sphalerite has quite a wide range with some outlying high concentration analyses (Figure 7; Table 5). The LA-ICPMS maps confirm that the Cu is very heterogeneous in the veins (Figure 29) but is more homogeneously distributed in colloform sphalerite L4c (Figure 13). High Cu values are also present in the Pb rich, Fe and Cd poor, zone within L4c (Figure 29).

In addition to the high Pb and Cu, Ge, As, Ag, Sb, and Tl are all present and elevated in the L4c growth zone (Figure 29). Arsenic, Ag, Sb, and Tl also have increased values in a zone located at the boundary between darker L4a and L4b with lighter L4c (Figure 29). Germanium, Ag, Sb, and Tl are heterogeneously distributed in all of the L4 textures (Figure 29). Arsenic is

mostly detected in the L4c band and the nearby pyrite (Figure 29). In colloform L4, Ge, Ag, and Sb appear to be preferentially found in Fe poor sphalerite L4c in addition to Pb, Hg, and Cu (Figure 13).

4.1.4.2.2 *Lithophile elements*

Similar to the trend in Fe, Na concentrations decrease throughout the L4 paragenesis (Figure 7, 10; Table 5). The Zn and Na concentrations are strongly negatively correlated and Na and Fe concentrations have the strongest positive correlation of all the sphalerite generations (Figure 6e, 6g). Sodium is present along the Fe poor L4c growth zone but is also found in isolated areas with higher concentrations (Figure 30). A log scale view of the spatial distribution shows that Na is also present in all the L4 textures at lower levels (Figure 30).

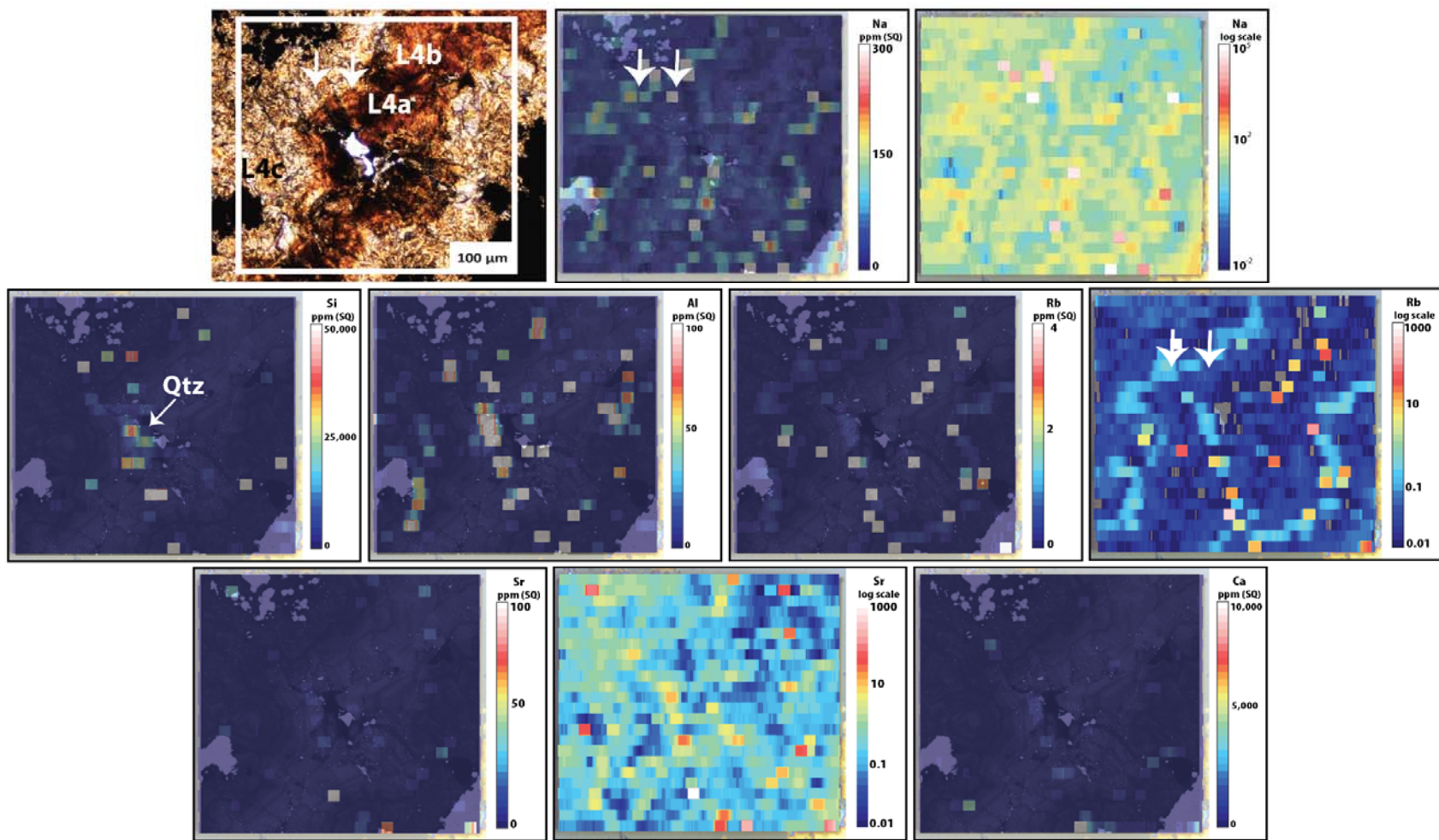


Figure 30. Quadrupole laser ablation element maps show the spatial distribution of lithophile elements present in a vein of sphalerite L4. The white box on the photomicrograph shows the mapped area. The maps (excluding the log scale images) have been overlaid on the Fe X-ray map to show presence of lithophile elements relative to the sphalerite zoning, pyrite (bright white), and quartz (dark). Sodium and Rb are also present in the thin outer zone which contains Cl, Pb, Ge, As, Ag, Sb, and Tl (see Figure 28, 29). Sodium and Rb are also present as inclusions and some of these inclusions also host Al, Si, Sr, and Ca. Additionally, Na, Rb, and Sr appear to be nearly homogeneous in log scale images.

Chlorine was not present in L4 above the EPMA LOD for spot analyses, however, is seen in EMPA maps in the growth zone in L4c which also has elevated Na, Pb, Cu, Ge, As, Ag, Sb, Tl (Figure 28, 29).

Silicon is present where quartz is present in the center of the vein (Figure 28, 30). Silicon is also sometimes present in colloform banded sphalerite L4b and L4c (Figure 31).

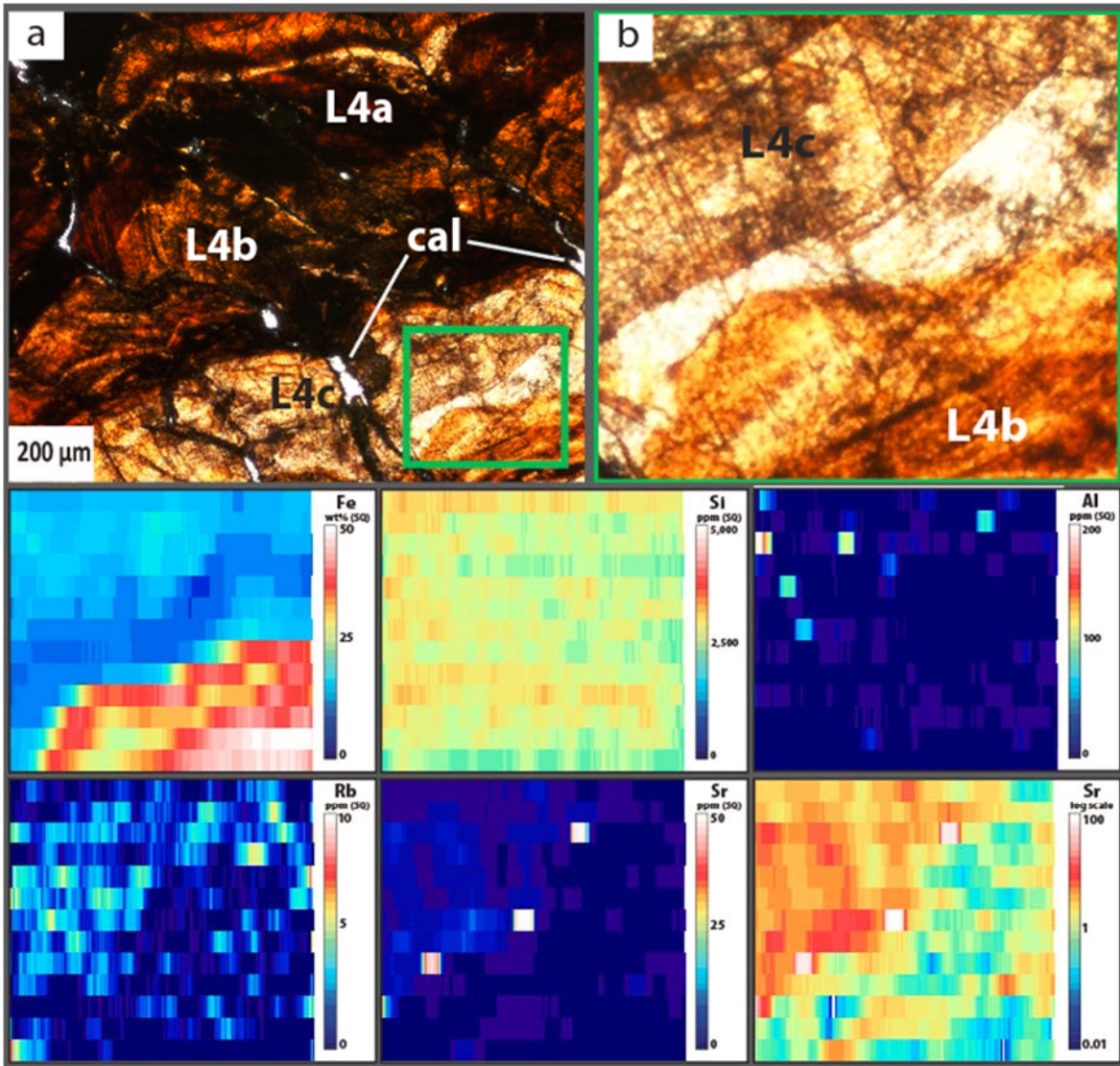


Figure 31. Sector field laser ablation maps showing the spatial distribution of Fe, Si, Al, Rb, and Sr in sphalerite L4c and more Fe rich L4b. (a) Transmitted light photomicrograph showing location of (b) the mapped area (green box). Silicon appears to be nearly homogeneous in the sphalerite L4. Aluminum is present in a few areas and is mostly located in the lighter, Fe poor L4c sphalerite. Abundant Rb is present and is also preferentially located in the L4c sphalerite. A few areas of Sr rich inclusions are located along the boundary between L4b and L4c and when viewed with a log scale, zonation is evident in the Sr spatial distribution which correlates with the textural zoning and the Sr is nearly homogeneous.

Aluminum only spatially correlates with some of the Si present as well as Rb in the LA-ICPMS maps (Figure 30). Additional Rb is seen in the L4c zone (Figure 30) and distributed throughout the L4c texture (Figure 31).

Some Sr inclusions spatially correlate with Ca and these two elements are also similar to Si, Al, and Rb (Figure 30). Also, Sr appears nearly homogenous in the L4c sphalerite (Figure 30, 31).

4.1.5 Sphalerite L5

4.1.5.1 Petrography and Texture

Sphalerite L5 is light gray to cream in color and locally exhibits a patchy texture which appears to be caused from crystal boundaries that can only be seen in transmitted light (Figure 32a, 32b). Sometimes areas of L5 appear light brown (Figure 27, 33a) and fluid and opaque inclusions can be seen at depth in some of these areas (Figure 33c). Sphalerite L5 cross cuts sphalerite L2 and L4 (Figure 12b, 12c, 27). Sphalerite L5 is sometimes found in veins containing quartz and pyrite (Figure 32b).

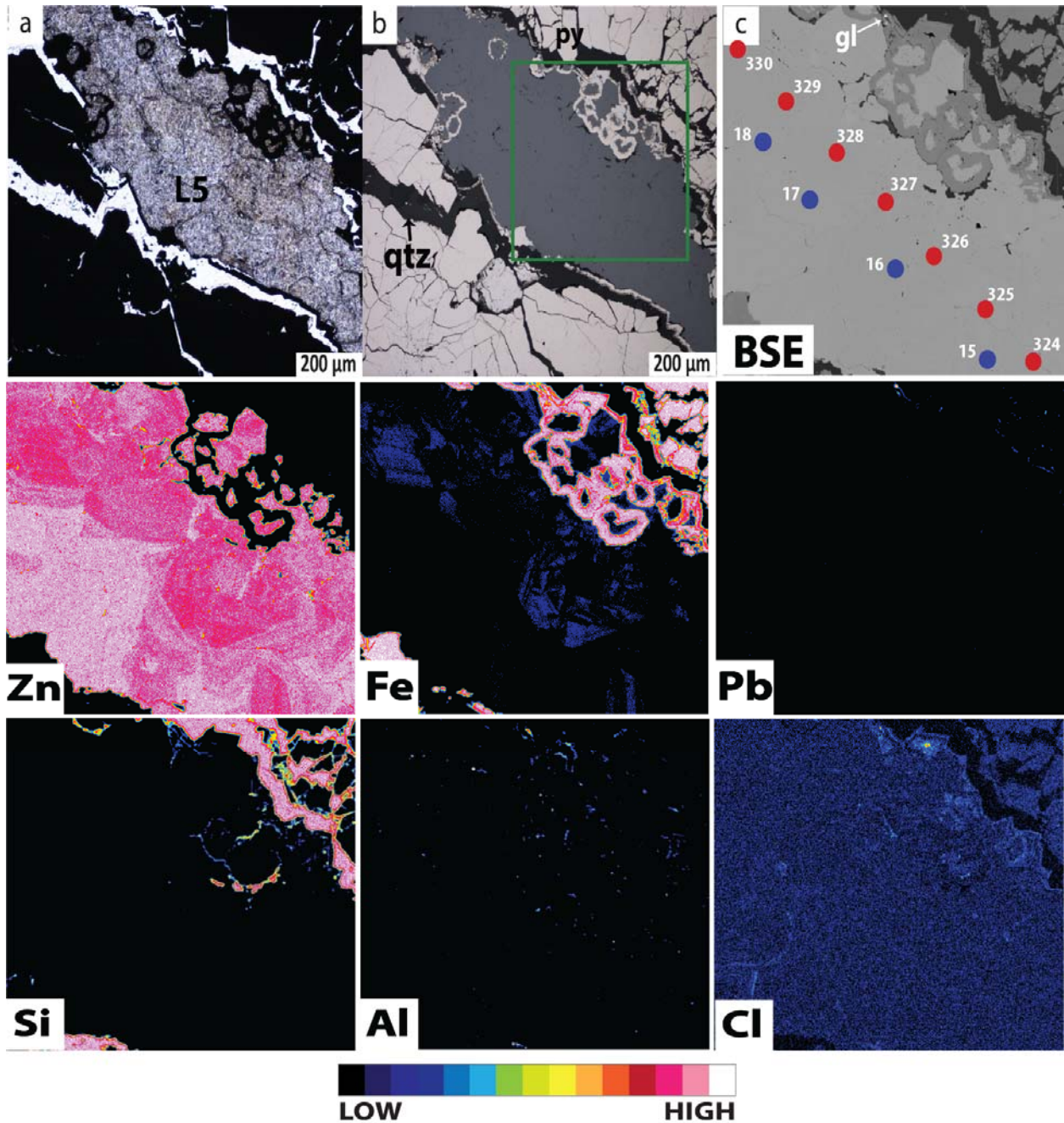


Figure 32. (a) Transmitted light and (b) reflected light photomicrograph of L5 sphalerite in sample 923 – 2373.4b. The sphalerite is located in a quartz and pyrite vein. (c) BSE image of sphalerite which shows rare galena present in the pyrite. JOEL spot analyses are shown in red and CAMECA are shown in blue. The Zn spatial distribution shows that a subtle zoning in the Zn concentration is present which negatively correlates with the Fe present in the sphalerite. The Pb X-ray map shows that galena is only associated with the quartz and pyrite and not in the sphalerite. The Si X-ray map highlights the vein quartz and is not present in the sphalerite. Aluminum appears as very fine inclusions distributed throughout some areas of the sphalerite as well as the pyrite and quartz. (f) Chlorine is only located in significant concentrations within the quartz and pyrite area (top of map).

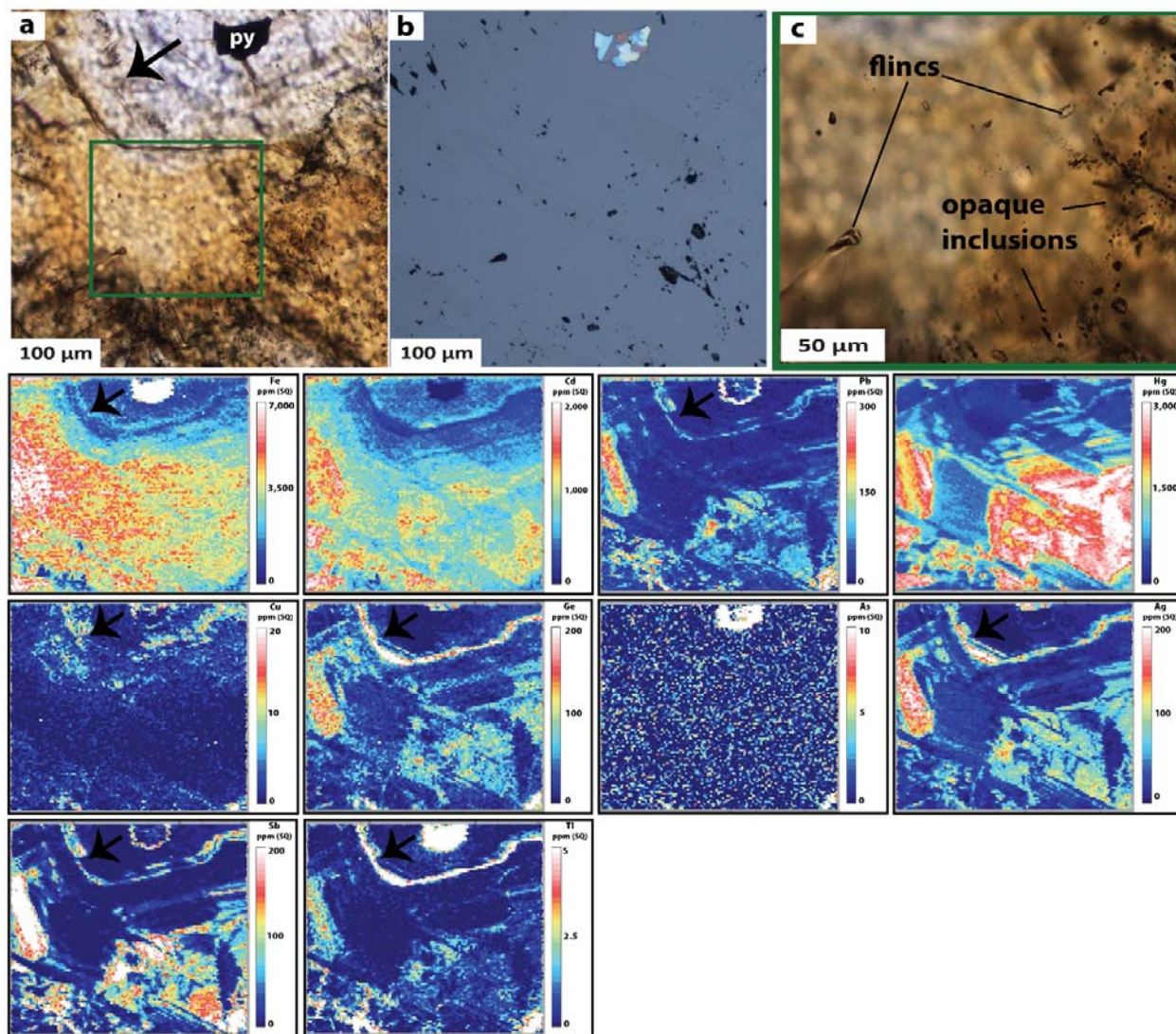


Figure 33. Quadrupole laser ablation element maps show the spatial distribution of elements present in sphalerite L5 of sample 1714 – 2471.2b. The zoning in Fe content correlates with the color zones observed in transmitted light (a). Fluid inclusions as well as inclusions of opaque minerals are visible as imperfections on the sphalerite surface (b) as well as at depth using a high magnification (c). The location of (c) is indicated with a green square in (a). The Cd also correlates with the color zones, however, some areas of higher concentration are present in irregular zones. Many of the other element maps (Pb, Hg, Ge, Ag, Sb, and Tl) also have this irregular zoning which is mostly present in the areas of abundant inclusions. In addition to the irregular zoning, a thin zone is present in the Fe, Pb, Cu, Ge, Ag, Sb, and Tl and spatially correlates with a thin zone of opaque inclusions in the sphalerite (see black arrows).

4.1.5.2 Composition determined by EPMA and LA-ICPMS

4.1.5.2.1 Chalcophile (+Fe) elements

Relative to L1 to L4 sphalerite, sphalerite L5 contains significantly lower Fe and Cd and has higher Zn concentrations (Figure 7, 17, 27; Table 5). Iron concentrations analyzed by EPMA

are much lower and range from 0.10 to 2.22 wt% (Figure 7; Table 5); the higher values are found in areas where L5 has a browner color (Figure 27, 32, 33). The Cd concentration ranges from 0.04 to 0.35 wt% in EPMA spot analyses (Figure 7; Table 5) and although the Cd spatial distribution is similar to the Fe spatial distribution in LA-ICPMS maps, it also agrees with many of the other trace element maps (Figure 33).

Within the areas of higher Fe, LA-ICPMS maps of Cd, Pb, Hg, Cu, Ge, Ag and Tl concentrations show they are concentrated in irregular zones (rather than oscillatory zones; Figure 27, 33). Additionally, a thin zone of Pb, Cu, Ge, Ag and Tl is located in the Fe poor zone and this occurrence correlates with opaque inclusions seen in the sphalerite (Figure 33).

4.1.5.2.2 *Lithophile elements*

In addition to the chalcophile elements present, Na, Rb, and Sr are also abundant in the inclusion rich area (Figure 34). Silicon and Al are present in a few of the inclusions and Ca is hosted in many of the inclusions (Figure 34). Rubidium, Sr, and Na are also present in the thin zone that contains Fe, Pb, Cu, Ge, Sb, Ag, and Tl (Figure 33, 34).

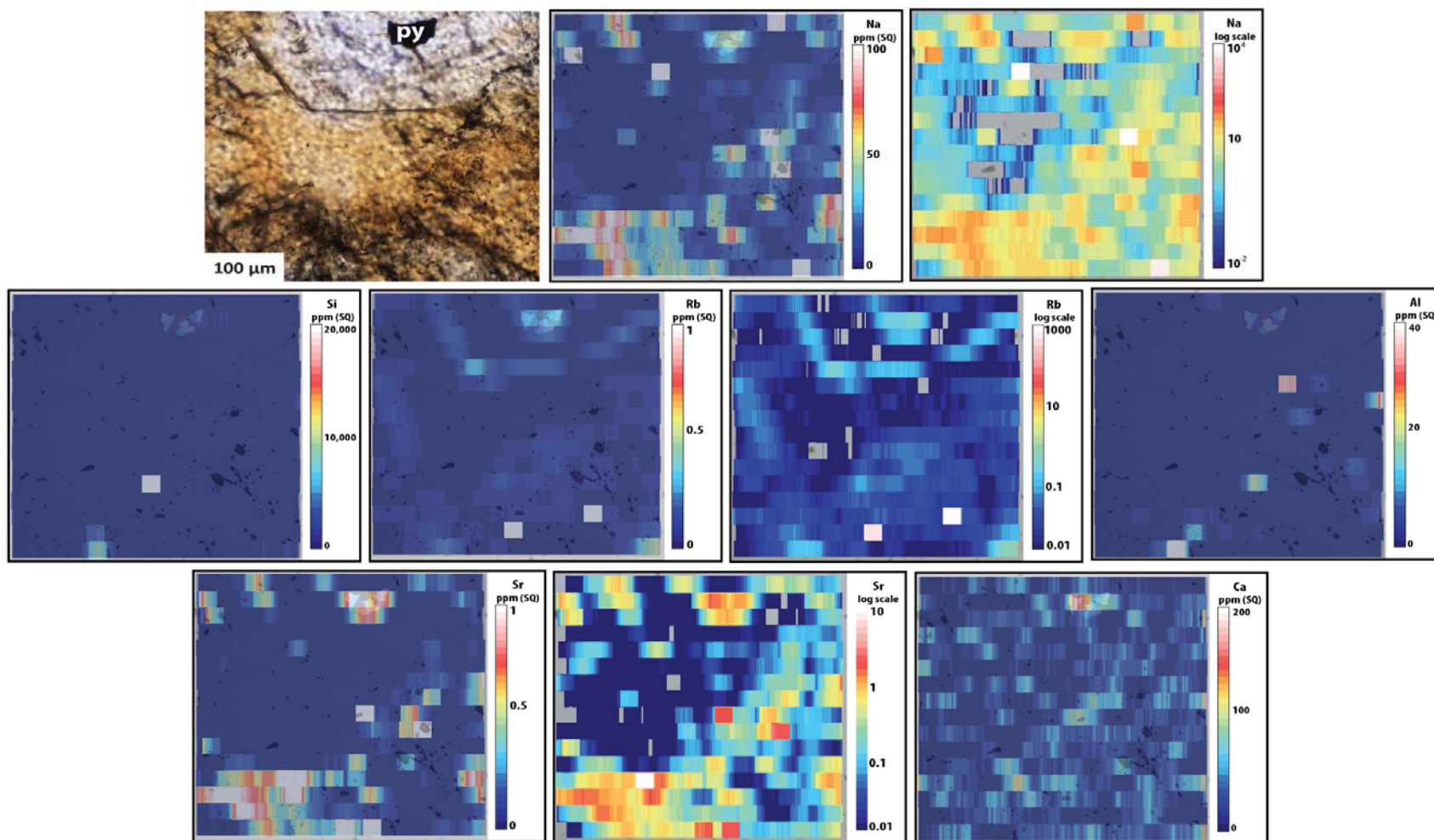


Figure 34. Quadrupole laser ablation element maps show the spatial distribution of lithophile elements present in sphalerite L5. The trace element maps have been overlaid on a reflected light photomicrograph that was taken prior to the analyses. Log scale maps show that Na, Rb, and Sr are also concentrated in areas containing abundant inclusions in the sample. A few of the inclusions in this area also contain Si and Al and Ca is abundant throughout the map. Rubidium and to a lesser degree, Na and Sr, are present in the thin zone which also hosts Fe, Pb, Cu, Ge, Ag, Sb, and Tl (shown in Figure 33).

4.2 Upper Ore Zone

Sphalerite within the upper ore zone consists solely of the sphalerite U1 generation (Table 3). Sample 809-2332.7 is dominated by this sphalerite. This generation varies in content, color, and texture and has been divided accordingly into 3 sphalerite subgroups.

4.2.1 Sphalerite U1

4.2.1.1 Petrography and Texture

Sphalerite within the upper ore zone consists entirely of sphalerite U1 and this sphalerite has been subdivided into 3 similar but distinct occurrences. Sphalerite U1a dominantly has a cream color (Figure 35a, 35f). Rare quartz and abundant nodular pyrite which ranges from $<20\ \mu\text{m}$ to $>10\ \text{mm}$ (Figure 35a) are observed within the sphalerite and this pyrite predates the sphalerite (Figure 35a, 35f). Areas of opaque material are also present in the U1a sphalerite and $<20\ \mu\text{m}$ acicular minerals are hosted in this opaque material (Figure 35g). This material is likely the mudstone host which was entrained during sphalerite precipitation.

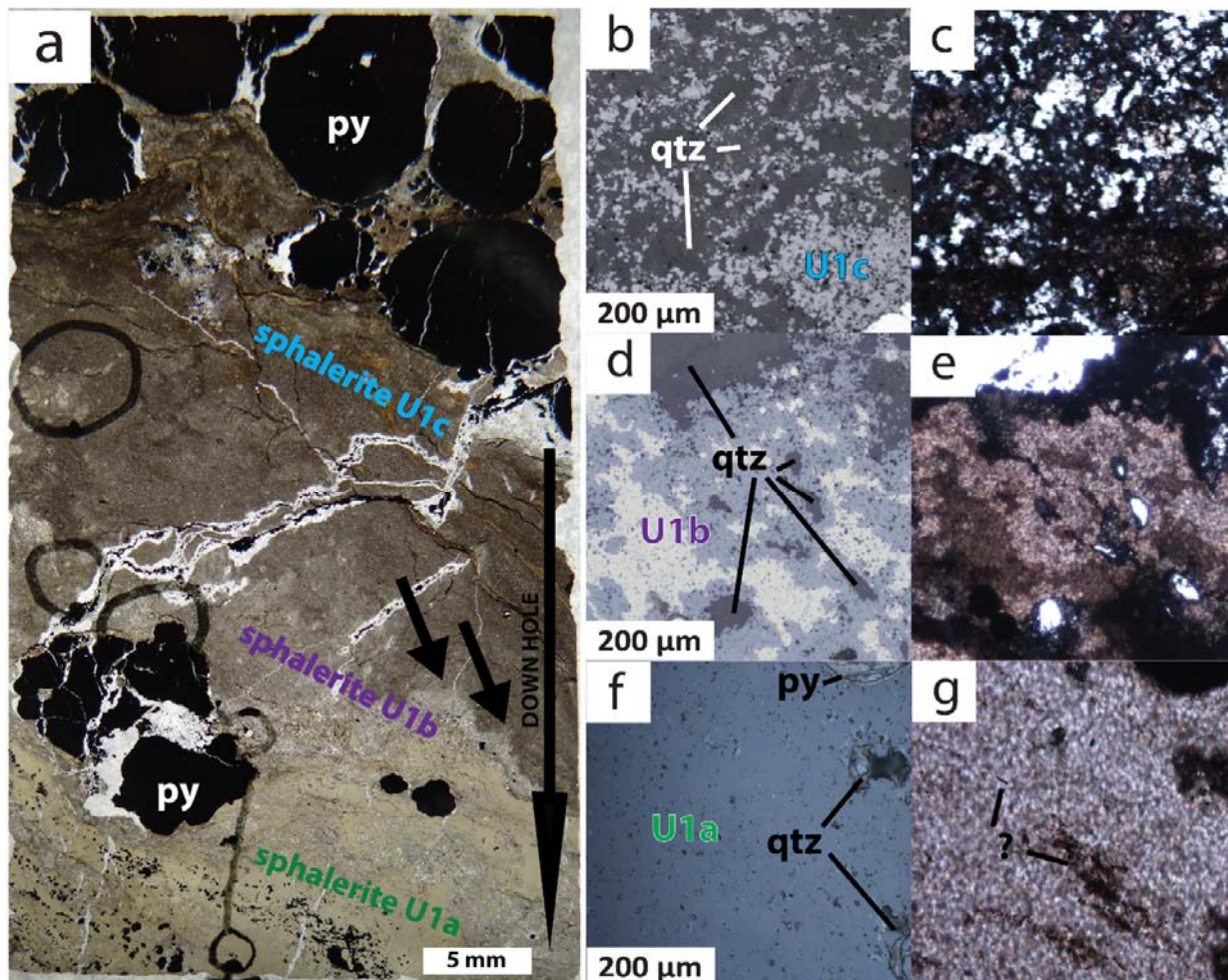


Figure 35. (a) Thin section image of sample 809 – 2332.7a which illustrates the relationship between sphalerite U1a, U1b, and U1c and the layering that is present in this sphalerite generation. The sphalerite has grown around earlier nodular pyrite. Soft sediment deformation features are most prominent between sphalerite U1a and U1b (black arrows). (b) Reflected light and (c) transmitted light image of dark brown sphalerite U1c showing sparse patches of sphalerite in a quartz dominated matrix. (d) Reflected light and (e) transmitted light image of sphalerite U1b showing variably colored sphalerite which is a mixture of U1c and U1a sphalerite. (f) Reflected light and (g) transmitted light image of sphalerite U1a showing dominant concentration of lighter cream colored sphalerite with inclusions of opaque material ((?) - likely mudstone host rock but not sure) and nodular pyrite. Quartz is less abundant in this lower texture of sphalerite.

Sphalerite U1b ranges from light cream (similar in color to U1a) to dark brown (Figure 35a, 35e). Quartz is more abundant in sphalerite U1b than U1a (Figure 35d, 35f). Sphalerite U1b has been determined to be a mixture of sphalerite U1a and U1c.

Sphalerite U1c of the upper ore zone consists of patches of sphalerite intergrown with abundant quartz (Figure 35b, 35c). The coarsest patches of sphalerite present are only ~200 µm on average and are dark brown (Figure 35c).

On a macro scale, the sphalerite U1 textures are clearly stratified and the layers grade from light tan U1a at the bottom of sample 809-2332.7 to dark brown U1c at the top of the sample (Figure 35a). The opaque material noted in sphalerite U1a is similar in orientation to the bedding visible in the thin section (Figure 35a, 35g).

4.2.1.2 Composition determined by EPMA and LA-ICPMS

4.2.1.2.1 *Chalcophile (+Fe) elements*

The major, minor, and trace element concentrations of the U1 textures agree with the observations noted on a micro and macro scale. Sphalerite U1 hosts the highest Zn values of all the sphalerite generations (60.3 to 66.7 wt%) as well as some of the lowest S values (31.9 to 32.8 wt%; Figure 6, 7; Table 5).

Iron and Cd concentrations in the upper ore zone sphalerite are significantly lower than sphalerite of the lower ore zone (Figure 7) and X-ray and LA-ICPMS element mapping reveals that Fe is only present as nodular pyrite and <5µm pyrite inclusions (Figure 36, 37). Cadmium was detected in all three sphalerite textures and concentrations increase up-hole (Figure 7, 37, 38; Table 5).

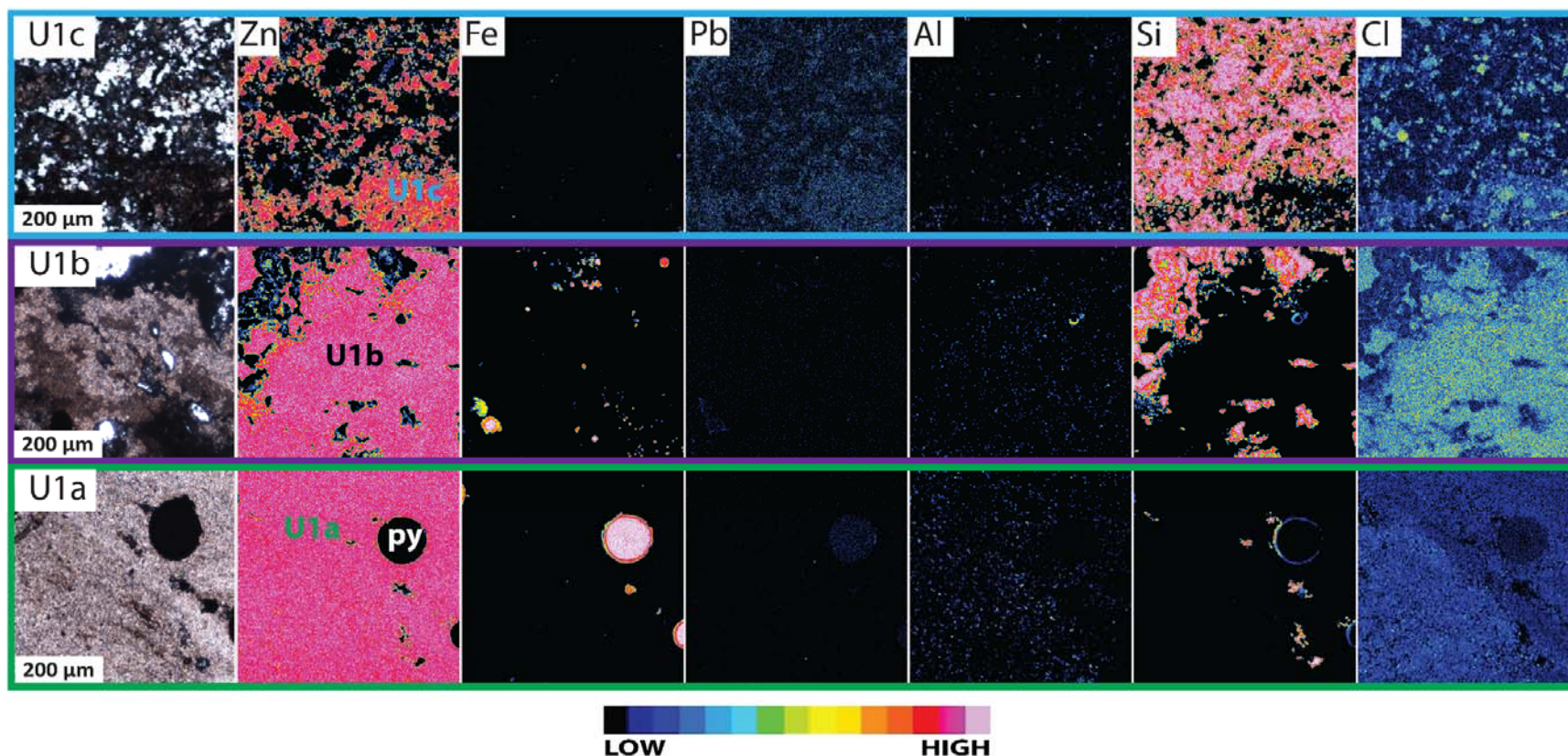


Figure 36. X-ray element maps of sphalerite U1c (top row), U1b (middle row), and U1a (bottom row) indicating the spatial distribution of elements present in each of the sphalerite textures. Pyrite is illustrated in the Fe maps and is rare in U1c. The pyrite concentration decreases up-hole and nodular pyrite is abundant in U1a. The concentration of Pb is very low and difficult to interpret using this analytical method, however, the Pb may be increasing in concentration up-hole. Aluminum indicated in the element maps is hosted in the sphalerite and not in the quartz or pyrite. The Si concentration supports the quartz observation made in photomicrographs and the quartz abundance is clearly increasing up-hole. Chlorine increases in concentration up-hole and bedding in the U1a sphalerite is visible in the Cl map, however, the U1a zoning observed is possibly caused by X-ray continuum.

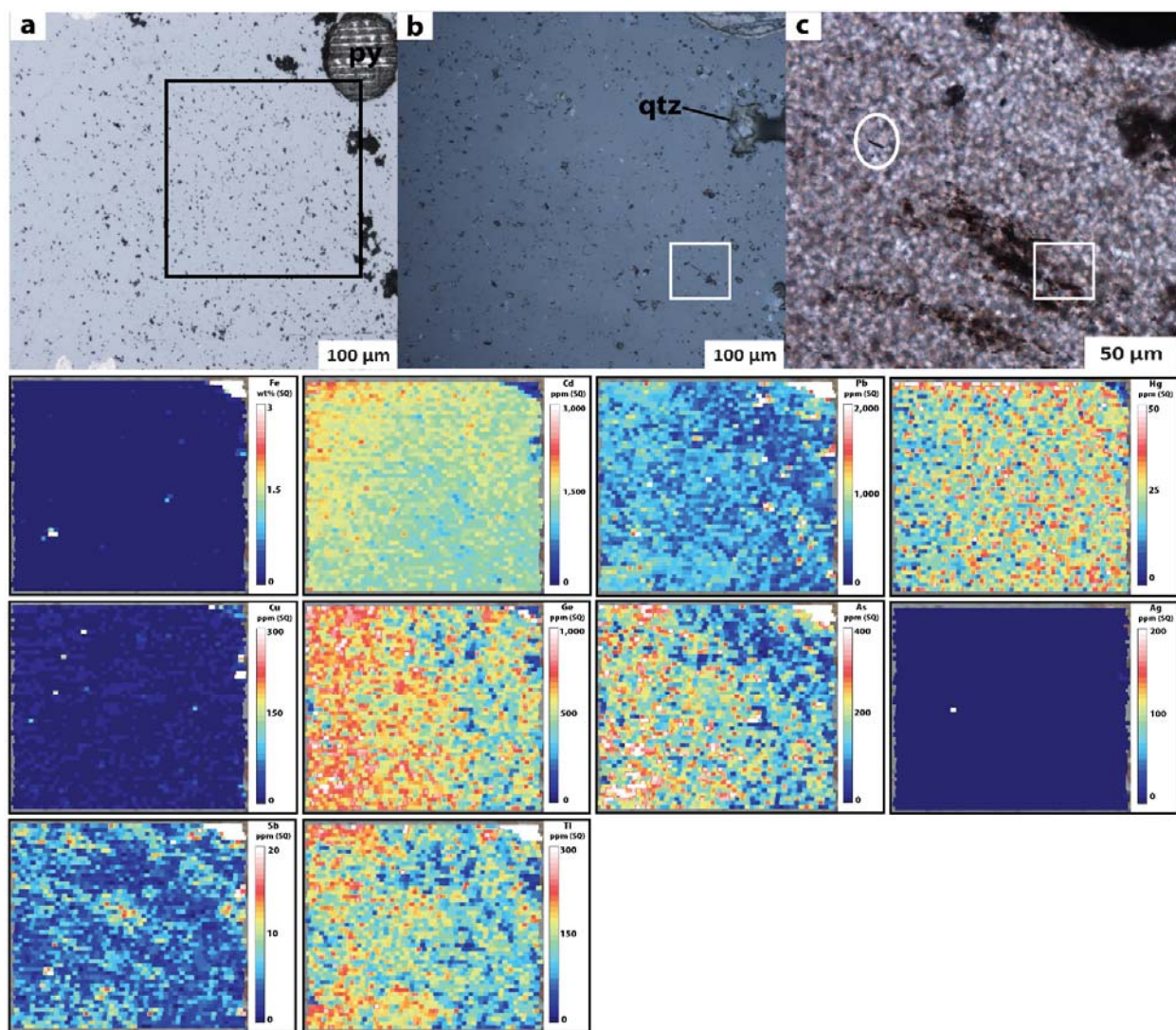


Figure 37. Quadrupole laser ablation element maps show the spatial distribution of trace elements in sphalerite U1a. (a) Reflected light photomicrograph show location of trace element mapping (black square). (b) Reflected light and (c) transmitted light photomicrograph of mapped area show the location of very fine acicular crystals (white square is crystal visible at the surface and is shown in Figure 41. White circle is additional crystal which is not exposed on the thin section surface). These crystals are oriented parallel to the sphalerite bedding in this sample. Cadmium, Hg, Ge, As, and Tl are mostly homogeneously distributed in the sphalerite. Iron, Cu, and Ag are only present as inclusions of additional sulfide minerals.

Other than Cd, chalcophile elements were not quantitatively present above the EPMA LOD in any of the U1 textures. Trace element LA-ICPMS mapping did identify some chalcophile elements in the U1 sphalerite.

Lead is present in both U1a and U1c, however, in U1a it is less abundant and is associated with the pyrite and opaque material (Figure 37, 38). The Pb abundance increases in later U1c sphalerite (Figure 37, 38). In the U1c sphalerite, the Pb concentration and abundance appears to decrease toward the nodular pyrite (Figure 38).

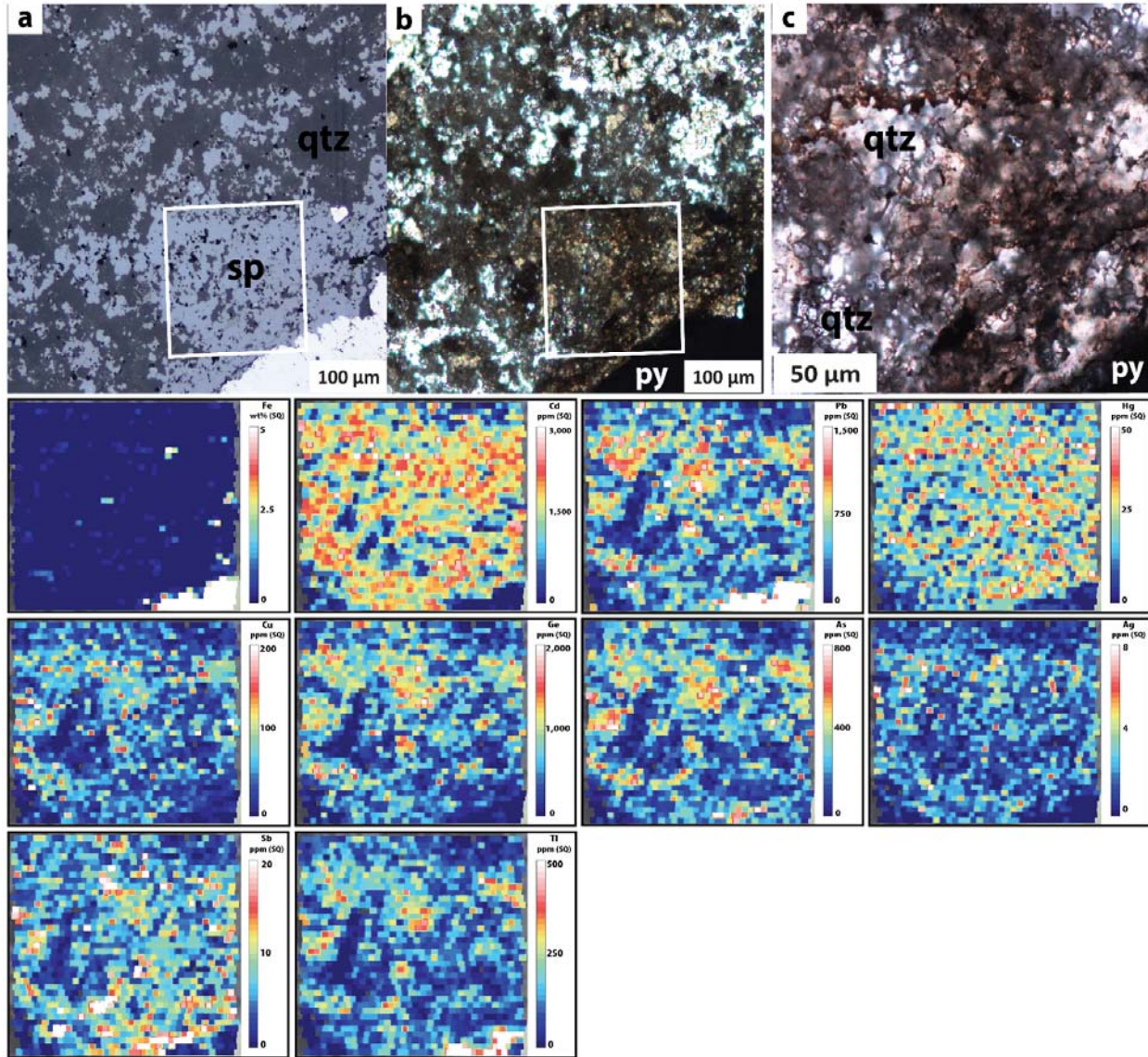


Figure 38. Quadrupole laser ablation element maps show the spatial distribution of trace elements present in U1c sphalerite. (a) Reflected light and (b) transmitted light photomicrograph showing location of (c) as well as trace element maps (white boxes). (c) Location of trace element mapping which shows sphalerite intergrown with abundant quartz. Aside from Fe, the trace element maps show a patchy spatial distribution and these elements are all present in the sphalerite and not in the quartz. Lead, Cu, Ge, As, Ag, and Tl appear to slightly increase in concentration further from the pyrite. Antimony shows an opposite trend and appears to increase toward the pyrite. Lead and Tl are higher in the pyrite nodule (lower right corner). I think I say abundance instead of concentration in the results

Similar to Pb, Ge, As, and Tl are present in both U1a and U1c sphalerite (Figure 37, 38). The spatial distribution of these elements in the U1c sphalerite also shows that the concentration and abundance decreases slightly toward the nodular pyrite (Figure 38). Antimony is also present

in both textures, however, is seen increasing in concentration and abundance towards the nodular pyrite in U1c.

Copper and Ag are only present in U1a in rare inclusions which are likely additional sulfide minerals (Figure 37). These elements are more homogeneously hosted in U1c sphalerite (Figure 38). Similarly to Pb, Ge, As, and Tl, the U1c Ag concentration decreases towards the nearby nodular pyrite (Figure 38).

4.2.1.2.2 *Lithophile elements*

Sodium was present in the majority of the EPMA quantitative spot analyses (24 of 28), however, the concentrations are much lower than that of the lower ore zone sphalerite (Figure 10; Table 5). The Na spatial distribution appears homogeneous in LA-ICPMS maps and sphalerite U1a Na also shows an orientation similar to the layering observed in the opaque material and on a macro scale (Figure 35a, 35g, 39, 40).

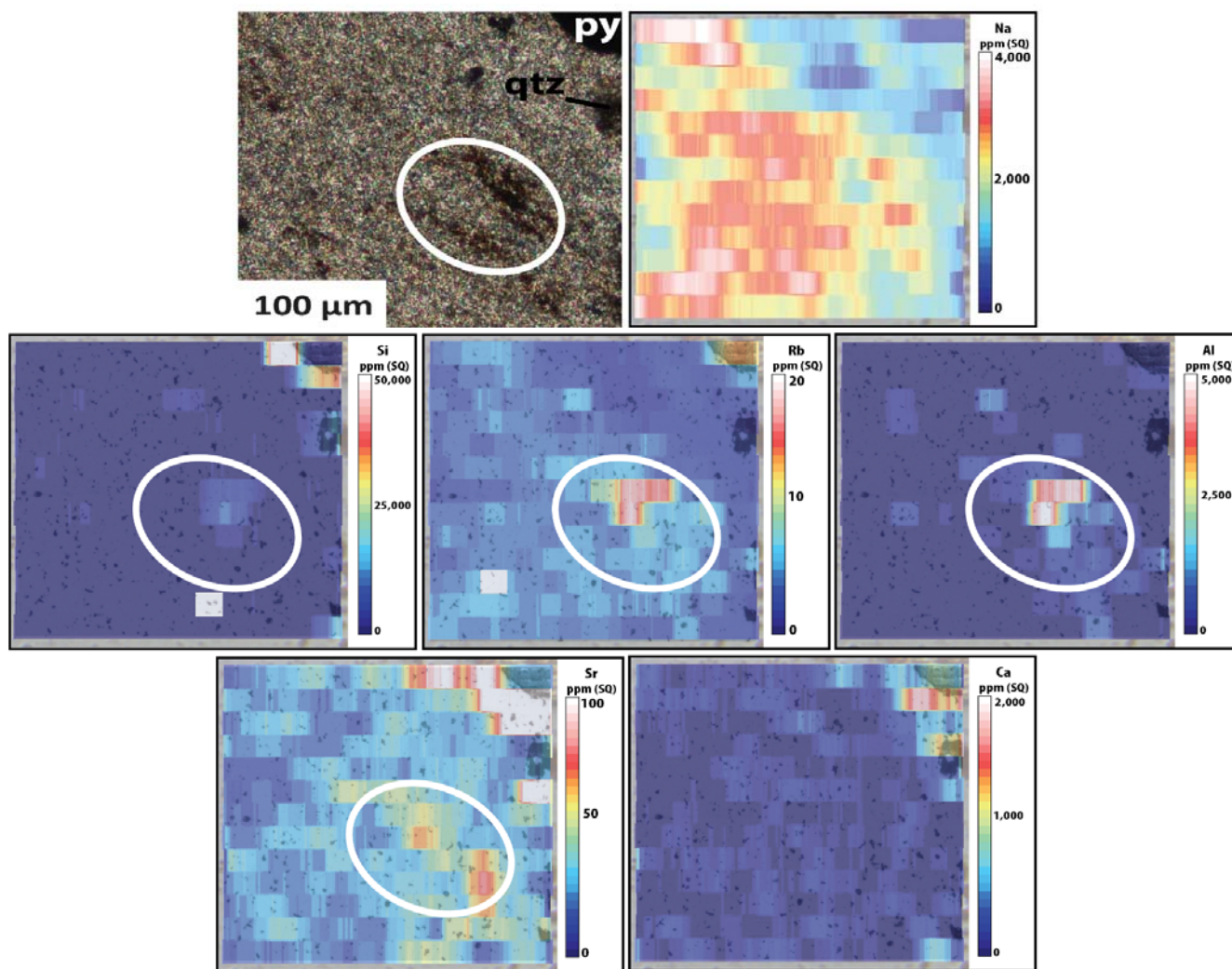


Figure 39. Quadrupole laser ablation trace element maps show the spatial distribution of lithophile elements in sphalerite U1a. The maps have been overlaid on reflected light photomicrographs to investigate the presence of lithophile elements relative to surface features. Sodium and Rb are more concentrated in the lower sphalerite U1a, whereas Sr occurs across the map area. Silicon, Rb, Al, and Sr are highly concentrated in the opaque material which is host to acicular crystals. Silicon, Rb, Sr, and Ca are associated with the nodular pyrite.

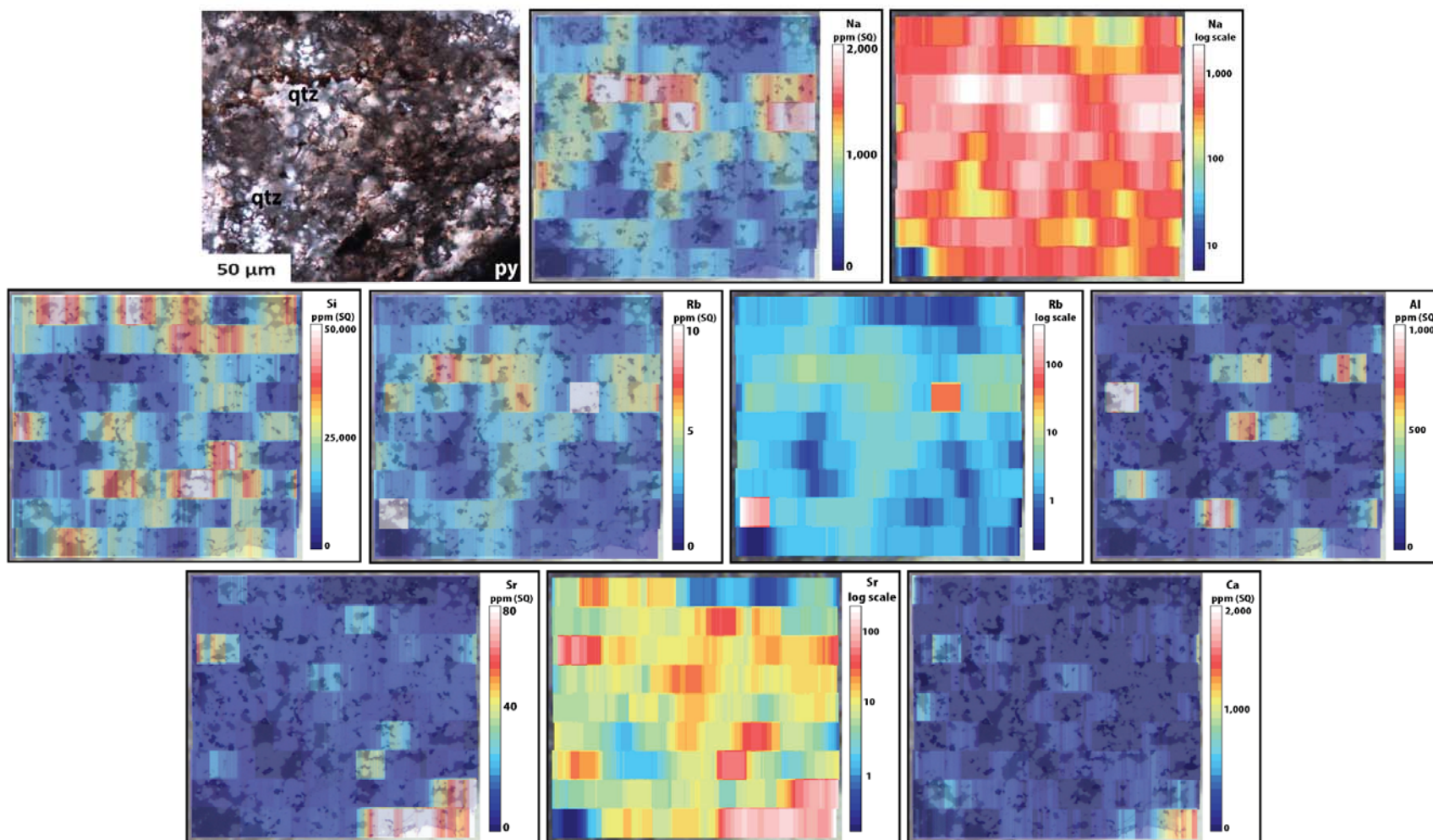


Figure 40. Quadrupole laser ablation trace element maps show the spatial distribution of lithophile elements in sphalerite U1c. The maps have been overlaid on reflected light photomicrographs to investigate the presence of lithophile elements relative to the pattern of sphalerite and quartz. Sodium, Rb, and Sr are all present throughout the sphalerite. Aluminum is present in some areas of the sphalerite and sometimes correlates with Rb. Strontium and Ca show some correlation and are both present in the pyrite.

Chlorine was analyzed in 26 EPMA spots and occurs at significantly higher concentrations than in the lower ore zone (Figure 10; Table 5). The spot analyses show that U1a sphalerite has higher Cl concentrations (Figure 10; Table 5), however, the X-ray maps suggest that Cl may increase in concentration from sphalerite U1a to U1c (Figure 36). A smaller scale X-ray map of U1a shows that Cl is heterogeneously present in the sphalerite and is not present in the acicular mineral (Figure 41).

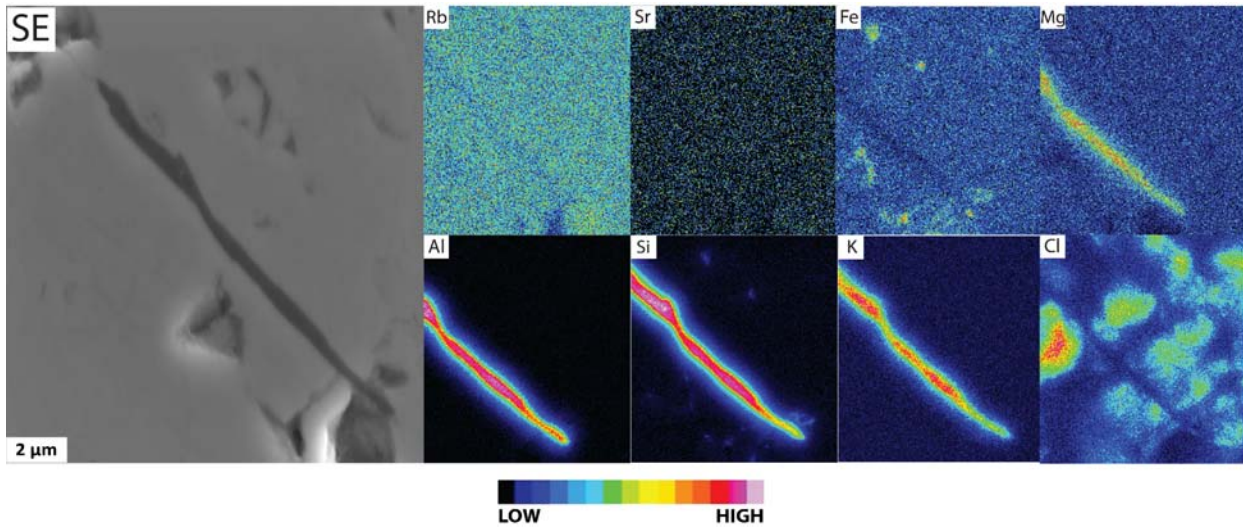


Figure 41. Field emission SE image and X-ray elemental maps of acicular mineral present in the opaque material of sphalerite U1a. The elemental maps indicate that the mineral is composed of Al, Si, and K with lesser amounts of Mg. Rubidium and Sr were not detected using this analytical technique. Chlorine is not present in the crystal of interest, however, is seen heterogeneously distributed in the U1a sphalerite.

Silicon was detected in 13 of the EPMA spots in the U1b and U1c sphalerite (Figure 10; Table 5). Silicon concentrations present in the element maps spatially correlates with quartz inclusions as well as the opaque material identified in sphalerite U1a (Figure 36, 39, 40). Aluminum was present in 6 U1 EPMA spots and is much higher in abundance and concentration than the lower ore zone textures (Figure 10; Table 5). Element mapping shows that Al present does not correlate with the quartz rich matrix surrounding sphalerite U1c, but is located within the sphalerite itself (Figure 36, 40).

Rubidium and Sr are concentrated in the opaque material and are also homogeneously present in lower concentrations within the LA-ICPMS maps of U1a (Figure 39). In U1c, Rb and Sr show a heterogeneous spatial distribution and Rb is more abundant than Sr (Figure 40).

Strontium, Rb, Ca, and Si are seen in higher concentrations associated with nodular pyrite (Figure 39, 40).

Using EPMA, a <1 μm wide acicular crystal was identified at the sample surface within the opaque material of sphalerite U1a (Figure 40). Because the mineral is too small, EPMA spot analyses was not successful, however, X-ray element maps show that the mineral consists mostly of Al, Si, and K with minor Mg (Figure 41).

5 Discussion

5.1 Potential alteration of sphalerite composition during the Brookian Orogeny

The rocks within the Red Dog district have been reported as being unmetamorphosed or only weakly metamorphosed by the Brookian orogeny (Moore et al., 1994). Despite this, the Red Dog district still underwent significant burial and fluid flow during this time. Using fission tracks on apatite and zircon, total burial depths have been estimated at 9 km using a surface temperature of 5 $^{\circ}\text{C}$ and a thermal gradient of 25 $^{\circ}\text{C}/\text{km}$ (O'Sullivan et al., 2000). Additionally, Dumoulin et al., (2004) used conodont alteration indices to show that temperatures were as high as 120-190 $^{\circ}\text{C}$ with burial depths of around 3.5-5.5 km. The Western Brooks Range shows widespread late fluid flow events, now preserved as late quartz-carbonate veins (Kelley et al., 1998). These late veins have a lower salinity of <5 wt% and yield homogenization temperatures of <220 $^{\circ}\text{C}$ which are similar to the ore precipitation temperatures of <200 $^{\circ}\text{C}$ (Leach et al., 2004).

Furthermore, studies investigating the remobilization of elements in sphalerite have reported that crystals below 350 $^{\circ}\text{C}$ maintain original composition (Mizuta, 1988). Additionally, sphalerite which experiences significant metamorphism can be differentiated from hydrothermal zoned sphalerite by a distinct lack of zoning (Mizuta, 1988; Lockington et al., 2014) which can include the S isotopic composition (Cook and Hoefs, 1997).

Because of the relatively low temperatures experienced during thrust related burial, the composition of the Anarraaq sphalerite is likely to reflect the ore forming processes.

5.2 Chalcophile elements in sphalerite

At Anarraaq and the main Red Dog deposits, previously determined *iron* concentrations determined using LA-ICPMS spot analyses range from 0.20-7.00 wt% and 0.40-7.30 wt%; respectively (Kelley et al., 2004b, 2004a). The EPMA spot analyses in this study show that Fe in

the Anarraaq sphalerite can actually be as high as >13 wt% (Figure 7; Table 5). Kelley et al., (2004b) reported Fe separately in the massive ore zone (lower ore zone; 1.00-7.00 wt%) and much lower Fe in the banded ore zone (upper ore zone; 0.20-0.40 wt%) of Anarraaq. This agrees with the significantly lower Fe observed in the EPMA analyses in the upper ore zone sphalerite of this study (Figure 7; Table 5). The previous findings also noted that Fe increases across the 4 sphalerite stages of the main Red Dog deposits (Kelley et al., 2004a) and although Anarraaq L4 has higher Fe overall, the late L5 sphalerite is Fe poor (Figure 7; Table 5).

Sphalerite incorporates a wide range in elements which impact the color of the mineral and can range from white to yellow, brown, red, pink, green, and black (Cook et al., 2009). The color variation in Anarraaq sphalerite is associated with the presence of Fe, where darker zones are associated with higher Fe concentrations (Figure 7, 8, 9, 13, 17, 27, 28, 29, 31, 33). This suggests that Fe is the main control on Anarraaq sphalerite color which agrees with previous observations at the main deposits (Kelley et al., 2004a). A strong negative correlation also exists between Fe and Zn concentrations in the EPMA data and this indicates that Fe is substituting for Zn (Figure 6b). Iron is the most studied substituent for Zn in sphalerite and FeS has been reported as high as 56 mol% in sphalerite (Barton and Toulmin, 1966; Lepetit et al., 2003).

In some Anarraaq sphalerites, Fe does not appear to control the color and this is best observed in sphalerite L2 (compared to L3 and L4; Figure 13). Sphalerite L2c typically appears darker than L3, however, L3 contains a higher Fe concentration (Figure 7, 18). This is likely due to the higher trace element content of L2 relative to L3 seen in the LA-ICPMS maps (Figure 13, 18). In the area where bright white to gray L2d sphalerite has a darker zone, Fe is poor (Figure 17). In this darker zone, Pb and Tl are present which indicates that one of these elements, or a combination of them, may have some control on L2d color. Iron is significantly lower in sphalerite in the upper ore zone based on EPMA analyses (Figure 7). Despite the lower Fe concentrations, the sphalerite color of U1c is darker than U1a (Figure 35). The LA-ICPMS maps show that Cu and Ag are not present in U1a, however, these elements are abundantly distributed in U1c and this suggests that Cu and Ag may also have an impact on U1 sphalerite color (Figure 37, 38).

In addition to Zn, sphalerite can also be an ore mineral for *cadmium* which is produced as a by-product of refining Zn concentrate (Cook et al., 2009). Cadmium is the second most abundant element (after Fe) that is consistently present in the Anarraaq sphalerite (Figure 7;

Table 5). Concentrations of Cd, determined using EPMA, range from 0.04 to 1.19 wt% (Figure 7; Table 5) which is similar to the sphalerite at the main Red Dog deposits (0.50-1.00 wt%) determined by LA-ICPMS spot analyses (Kelley et al., 2004a). A comparison of EPMA sphalerite data from the upper and lower ore zones shows that Cd is lower in the upper ore zone (0.07-0.27 wt% upper; 0.04 to 1.19 wt% lower; Figure 7; Table 5).

Previous work on the main Red Dog deposits determined that there was no systematic relationship between Cd and the other trace elements present in the sphalerite (Kelley et al., 2004a), however, some association of Cd and other elements has been identified in this study. Although a weak correlation is seen between the Cd and Zn EPMA data, the data show some scatter and outliers (Figure 6c). An investigation of the spatial distribution of Cd in LA-ICPMS maps shows that Cd sometimes, but not always, correlates with the Fe controlled color zoning (Figure 9, 13, 17, 18, 27, 29, 33) and this agrees with the EPMA findings. For example, Cd in sphalerite L5 has a darker zone with increased Fe and Cd concentrations, however, a closer look shows that Cd also has an irregular zoning which is very similar to the zoning in the Pb, Hg, Ge, Ag, Sb, and Tl (Figure 33). Cook et al., (2009) reported a similar irregular zoning, in sphalerite from the Baisoara skarn, known as sectorial zoning which is independent of the rhythmic oscillatory zoning often seen in sphalerite.

It has long been suggested that Cd occurs in a solid solution series with Zn in sphalerite (CdS-ZnS solid solution (Kroger, 1940) and CdS in sphalerite has been reported to be as high as 20 mol% (Tauson and Chernyshev, 1977). Cadmium typically has a narrow range in concentration in sphalerite from epithermal, skarn, and stratabound deposits (Cook et al., 2009), but higher Cd concentrations (0.70-2.50 wt%) have been reported in the Lisheen Pb-Zn deposit (Wilkinson and Eyre, 2005). Based on the previous Cd findings, the narrow range in Cd EPMA seen here, and the negative Zn-Cd EPMA data correlation, Anarraaq Cd is possibly present in the sphalerite lattice as a bivalent cation Zn substituent.

Mercury concentrations in sphalerite from the lower ore zone range from 0.03-0.23 wt% in the EPMA data and Hg was not present above the EPMA LOD in the upper ore zone sphalerite (Figure 7; Table 5). The Hg contents measured in this study in the lower ore zone sphalerite are similar to the concentrations in sphalerite in the main Red Dog deposits (106-3650 ppm) (Kelley et al., 2004a). The LA-ICPMS element mapping shows that Hg in the Anarraaq lower ore zone has more complex spatial distributions than any other element. The variation ranges from

oscillatory zoning in L1 and L2 sphalerite which is independent of the Fe controlled color zoning (Figure 9, 17), irregular zoning in sphalerite L2c and L4 which is independent of all other element distributions (Figure 13, 18, 27, 29), and irregular zoning in sphalerite L3 and L5 but distributed similar to the other elements measured (Figure 24, 33). In addition to these spatial patterns, Hg is uniformly distributed in the upper ore zone (Figure 37, 38), which may suggest that Hg^{2+} is substituting for Zn^{2+} in the upper ore zone sphalerite. This substitution has been reported in sphalerite from the Eskay Creek deposit, BC (Grammatikopoulos et al., 2006). However, the main Red Dog deposit sphalerite does not show any evidence for Hg being structurally present in either LA-ICPMS spot analyses (Kelley et al., 2004a) or the lower ore zone EPMA data of this study.

In addition to Hg, Pb, Cu, Ag, and Sb were not present above the EPMA LOD in the upper ore zone sphalerite (Table 5). **Lead** in the lower ore zone sphalerite ranges 0.01 to 4.52 wt% in EPMA data and was only present in 61/473 spot analyses (Figure 7; Table 5). Because of the wide range in concentrations and the low abundance overall, the EPMA Pb could be the result of discrete submicron PbS inclusions which are sometimes $>1 \mu\text{m}$ and visible in BSE images and Pb X-ray maps (Figure 8, 15, 23, 28). A low incidence (<25 of 482 analyses) of the Pb data being above the EPMA LOD was also reported for the Navan deposit, Ireland, and the authors attributed this to the presence of microscopic inclusions in sphalerite (Gagnevin et al., 2014). The LA-ICPMS analyses from the main Red Dog deposits shows that Pb in sphalerite ranges 557-9830 ppm which is a narrower range than the results of this study, however, peak profiles in this type of analyses allow the user to remove portions of the data which are clearly impacted by inclusions (Kelley et al., 2004a). These authors found that several elements, including Pb, were present in sphalerite as inclusions. Additional LA-ICPMS work conducted on sphalerite hosted in 26 different ore deposits, showed that Pb is mostly present in sphalerite as submicron to nano-scale inclusions (Cook et al., 2009).

Anarraaq sphalerite in this study contains <0.01 to 0.76 wt% **copper** (Figure 7; Table 5) which is similar to the EPMA maximum value reported at Navan (6980 ppm Cu) by Gagnevin et al., (2014). The main Red Dog deposit sphalerite hosts Cu (436-2820 ppm) which is slightly lower than the Anarraaq sphalerite results of this study (Kelley et al., 2004a) and these authors interpreted Cu to be present as mineral inclusions. Although it has been suggested that Cu can replace Zn ions as a coupled substitution in sphalerite (Johan, 1988; Ohta 1995; Cook et al.,

2009), recent in-situ studies have also suggested Cu is often present in sphalerite as submicroscopic tetrahedrite–tennantite (Grammatikopoulos et al., 2006; Pfaff et al., 2011), and sometimes also chalcopyrite (Kelley et al., 2004a), inclusions in the sphalerite.

Silver present in EPMA data of sphalerite from Anarraaq ranges 0.04-0.11 wt% and was only detected above the LOD in 29/473 lower ore zone spot analyses (Figure 7; Table 5). This range is slightly lower than Ag in sphalerite at the main Red Dog deposits (199-1720 ppm) (Kelley et al., 2004a). A previous Anarraaq study using LA-ICPMS reported Ag in sphalerite from the lower ore zone at much higher concentrations (67-130 ppm) than in the upper ore zone (3-9 ppm) (Kelley et al., 2004b), both of which had significantly lower Ag than sphalerite in the main Red Dog deposits. The significant Ag present in sphalerite at Red Dog is similar to that reported for the Nanisivik Pb-Zn-Ag deposit, Canada (>700 ppm Ag) and the Navan Zn-Pb deposit, Ireland (<1100) (Cabri et al., 1985; Gagnevin et al., 2014). Because of the low abundance of Ag present above the EPMA LOD across all textures in the lower ore zone, Ag in sphalerite is likely present as discrete sulfide inclusions which was previously suggested by Kelley et al., (2004a) for Ag in the main Red Dog deposit sphalerite.

Antimony is not common in sphalerite (Cook et al., 2009), however, it is abundant in Anarraaq sphalerite and ranges 0.01-0.76 wt% (Figure 7; Table 5); this is slightly higher than Sb in sphalerite at the main Red Dog deposits (0.5-3560 ppm) (Kelley et al., 2004a). Similar to the Pb, Ag, and Cu concentrations, Sb has previously been interpreted as being present in sulfide inclusions based on LA-ICPMS spot analyses of main Red Dog sphalerite (Kelley et al., 2004a). Sphalerite at the Navan Zn-Pb deposit also hosts Sb <7630 ppm (Gagnevin et al., 2014).

The LA-ICPMS spatial distributions of Pb, Cu, Ge, Ag, Sb, Tl (and rare As) are in agreement in many of the LA-ICPMS maps from this study. In large (mm) scale mapping, these elements (excluding Tl which was not mapped), are more abundant in Fe poor L2 and L4c sphalerite (Figure 13). Contrary to this observation, Pb, Ge, As, Ag, and Sb are more associated with Fe rich L4 sphalerite in another sample (Figure 27). Thin bands of Pb, Cu, Ge, Ag, Sb, and Tl are present as oscillatory zoning in sphalerite L1, L4 (excludes Cu, but also has Rb and Na), and L5 sphalerite (Figure 9, 29, 33). Lead, Cu, Ge, Ag, Sb, and Tl are abundant in fibrous L2c sphalerite and the fibrous texture is evident in the maps (Figure 18).

In addition to these spatial observations, trace elements in sphalerite L3 and L5 are associated with areas of visible opaque inclusions (Figure 24, 27, 33). Inclusions in L3 are

spatially associated with Pb, Cu, Ge, Ag, Sb, and Tl (Figure 24), whereas L5 inclusions are associated with Pb, Ge, Ag, Sb, and Tl (no Cu) (Figure 33). Maps of this L5 inclusion rich area also display sector zoning (Figure 33) which is also evident in the Ge, Ag, and Sb (Tl not mapped) maps of another L5 area (Figure 27).

Spatial distributions of LA-ICPMS trace element maps in the upper ore zone are far less complicated than the lower ore zone (Figure 37, 38). Sphalerite U1a hosts Pb, Ge, As, Sb, and Tl that are uniformly distributed in abundance, whereas Cu and Ag are present as rare inclusions (Figure 37). The U1c sphalerite also hosts Pb, Ge, As, Sb, Tl, as well as Ag, in nearly homogeneous distributions (Figure 38).

5.3 Controls on trace element distribution

The source of metals in the Red Dog district is poorly understood (Kelley and Jennings, 2004) and the variability in chalcophile elements in the Anarraaq sphalerite can be attributed to several factors including fluid mixing, fluid-rock interaction processes, preferential partitioning due to co-precipitation of additional minerals in an assemblage, physiochemical changes (T , fO_2 , total sulfur concentration, salinity) in the environment during sphalerite precipitation, and lattice-scale controls (Barnes, 1979; Yardley, 2005; Cook et al., 2013; George et al., 2016). Although the present study is unable to constrain these conditions, the complex distributions of chalcophile elements warrants a discussion of these potential parameters within the context of this study and of the previous literature.

5.3.1 Fluid mixing

Similar to many sediment hosted massive sulfide deposits globally, Kelley et al., (2004b) suggested that the precipitation of Anarraaq sphalerite was chemically triggered by fluid mixing of a metal rich brine and a shallow fluid containing reduced sulfur (e.g. Fallick et al., 2001; Pfaff et al., 2011; Goodfellow and Lydon, 2007). The most reasonable explanation for the variable sphalerite trace element content is the input of different concentrations of elements from these two sources during the mixing process. Previous work on the Irish ore field sphalerite which coupled in-situ trace element analyses with S isotopic analyses has elucidated these processes. An association between Fe content and isotopically lighter S has been determined at the Galmoy and Navan deposits (Barrie et al., 2009; Gagnevin et al., 2014), and it has been suggested this is

one fluid end-member. Additionally, Navan sphalerite with isotopically heavy S values is associated with Cd, Sb, Cu, and Ag (Gagnevin et al., 2014); this is interpreted to be the hydrothermal input to the system. However, a similar correlation between Fe, Cd and S isotopic values at the Wiesloch MVT deposit, Germany, was not observed suggesting that different processes occur at different sites (Pfaff et al., 2011). The black shales of the Kuna Formation have abnormally low Fe/Ti ratios (Slack et al., 2004a) possibly due to the presence of significant amounts of diagenetic pyrite so it is unlikely that Fe was abundant in the pore fluids at Anarraaq. At Red Dog, the brines were likely derived from evaporated seawater and then descended deep into the basin (up to 7.4 km) where they became heated (Leach et al., 2004). It is also possible that the brine mixed with basement fluids which were released during episodes of tectonism (Blevings et al., 2013) and this could have caused variability in metals present in the brine over the long lived precipitation (0.3 m.y.; Schardt et al., 2008).

The trace element maps in this study have a high degree of spatial variability in element distributions in the sphalerite (discussed above). If fluid mixing was the sole cause of this variability, the mixing would have to be very complex or the metal rich fluids would have to have a very heterogeneous metal concentration. Pfaff et al., (2011) found that colloform Wiesloch MVT sphalerite precipitated as a result of episodic mixing between hydrothermal fluids and BSR sulfur rich fluid in the cavities. This cavity-hosted disequilibrium fluid mixing led to oversaturation which resulted in the incorporation of Pb, As, and Tl, which typically aren't hosted in sphalerite (Pfaff et al., 2011). Although the Anarraaq deposit is interpreted to be the result of carbonate replacement, the complexities of the carbonate dissolution are not known. Additional isotopic analyses would be required to link potential fluid variability with the trace element distributions.

5.3.2 Fluid-rock interaction

Lead isotopic analyses show that the Pb source cannot be attributed solely to the Kuna Formation or associated igneous rocks, and therefore was likely sourced from the deeper underlying rocks (Ayuso et al., 2004). It is not yet understood if the fluids laterally migrated through sandstones of the Endicott Group or even deeper in unknown Devonian and older rocks (Blevings et al., 2013) and they could have also interacted with Hunt Fork Shale, Noatak Sandstone, Kanayut Conglomerate, Kayak Shale, as well as the underlying Kivalina unit prior to

infiltration into the Kuna Formation. Fluid buffering with wall-rock is dominant in sediment hosted sulfide deposits (Yardley, 2005) and this likely resulted in leaching of cations along the trajectory of the metal rich brines from the deep aquifer to the site of deposition. In addition to low Fe₂O₃, the black, siliceous mudstones of the Kuna Formation also have depleted Zn, Pb, Cu, Sb and As concentrations relative to other black shales (Slack et al., 2004a). Similar to the Kuna Formation, the Kayak Shale has lower Fe₂O₃ concentrations and depleted Zn, Pb, Cu, Sb and As relative to other shales (Slack et al., 2004a). Therefore, either these two lithologies did not significantly contribute to the metal content of the brine or the present day compositions of the shales reflect significant fluid rock interaction which stripped these metals and added them to the mineralizing system.

5.3.3 Co-precipitation of a sulfide assemblage

Preferentially partitioning has been clearly demonstrated by LA-ICPMS element mapping of base metal sulfide assemblages from several deposits (George et al., 2015; 2016) and these results show that elements such as Ag, Tl, and Sb are located preferentially in galena whereas Cd, Cu, In, Mn, and Hg are located in sphalerite. This preferential partitioning is independent of temperature, pressure, redox, and metal source (George et al., 2016). Rather, the partitioning is controlled by the oxidation state of the element, the ionic radius of the element, and the coordination of the element relative to the coordination of sulfide (e.g. Zn in sphalerite is in tetrahedral coordination; George et al., 2016). The trace element maps of the present study show that Ag, Tl, and Sb, which preferentially partition into galena, are similar in distribution to Cu (Figure 9, 17, 18, 24). Anarraaq pyrite in the LA-ICPMS maps from this study preferentially contain more As and Tl than sphalerite, however the pyrite typically predates or postdates the sphalerite (e.g. Figure 17, 37). Additionally, the galena that is present in sphalerite typically cross-cuts the sphalerite (Figure 8, 12, 16). Because of a general lack of co-precipitating sulfides in the Anarraaq deposit and the combined presence of elements which typically partition between galena and sphalerite, partitioning of elements between sulfides in an assemblage does not appear to impact the presence of the trace elements in the Anarraaq sphalerite.

5.3.4 Physiochemical changes

Many studies have shown that base metal solubility and precipitation from a hydrothermal fluid is controlled by a number of factors including temperature, oxidation, sulfur concentration, pH, and salinity (e.g. Cooke et al., 2000 and references therein). Although Red Dog sulfide deposition is thought to have occurred at the site of mixing between a metalliferous brine and a source of reduced S, the exact geochemical conditions during ore precipitation remain unclear (Leach et al., 2004; Kelley and Jennings, 2004; Kelley et al., 2004a). Because these conditions have not been constrained, it is possible that several parameters influenced the trace metals present in the ore.

Because significant buffering of metal rich fluids with wall rock can limit drastic decreases in solubility caused by changes in oxidation, sulfur, and pH, it has been suggested that temperature and salinity are the only independent, and therefore dominant, controls on metal concentrations in sediment hosted systems (Yardley, 2005). Sulfide precipitation at Anarraaq occurred in shallow sediment below the sea floor (Kelley et al., 2004b). Considering the shallow depths as well as the interpreted temperature of precipitation at the site, (<200°C; Leach et al., 2004), the migrating metal rich brine was likely significantly hotter than the pore fluid at the site of deposition. If the hot brines were episodically introduced at the site of mineralization, the rapid decrease in temperature could have impacted the solubility of trace elements.

If the metalliferous brines were locally not in equilibrium with Kuna Formation host rock, additional controls such as oxidation, the concentration of sulfur, and pH could have also impacted the metals present in Anarraaq sphalerite. There is some evidence for fluctuations in the oxidation state during deposition of the Kuna Formation (Slack et al., 2004b; Johnson et al., 2004) as well as locally within the mineralized area (Reynolds et al., 2015). Although this doesn't necessarily imply fluctuating redox during sulfide precipitation, it indicates that redox conditions during Kuna deposition were much more complicated than originally proposed and they could have impacted the trace element content of the sphalerite. Recent X-ray absorption near edge structure (XANES) spectroscopy has determined oxidation states and substitution mechanisms of Ge in sphalerite (Cook et al., 2015; Bonnett et al., 2017). These studies have identified both Ge⁴⁺ in sphalerite from the Tres Marias deposit (Cooke et al., 2015) and Ge²⁺ as well as Ge⁴⁺ in Tennessee sphalerite (Bonnet et al., 2017). Both ions were in tetrahedral coordination in the sphalerite which can be interpreted to suggest they were lattice-bound,

however, the Tennessee sphalerite also hosted Ge^{4+} surrounded by oxygen atoms (Bonnett et al., 2017). Previous trace element analyses of Red Dog sphalerite has suggested that elements such as Pb, Ag, Cu, and Sb are hosted as discrete mineral inclusions within the sphalerite (Kelley et al., 2004a) and the present study cannot prove otherwise (for these elements or Hg, Ge, As, and Tl). Because the speciation of these trace elements cannot be confirmed, the oxidation of these elements during sulfide mineralization cannot be constrained without additional analyses.

The ZnS-FeS solid solution is dependent on temperature and the concentration of reduced sulfur in the system (Barton and Toulmin, 1966). Experiments at high temperatures ($>580^\circ\text{C}$) have shown that this substitution can be negatively impacted by an increase in sulfur concentration into the stability field of FeS_2 (Barton and Toulmin, 1966). Additional studies on natural sphalerite show a similar dependency on the concentration of FeS at lower temperatures ($<300^\circ\text{C}$) and lower FeS is present in sphalerite formed in higher sulfur concentrations (Scott and Kissin, 1973). This agrees with the substitution of Zn^{2+} for Fe^{2+} which does not significantly distort the lattice because of a very similar ionic radius (Pring et al., 2008). Despite this, some authors (e.g. Lepetit et al., 2003 and references therein) have discussed the potential presence of Fe^{3+} in sphalerite which precipitated under higher sulfur concentrations. Because of the effect sulfur concentration has on ZnS-FeS solid solution, the Fe controlled color zoning seen present in many Anarraaq sphalerite generations may be caused by fluctuations in sulfur rather than the overall concentrations of Fe in the system.

Besides oxidation, temperature, and total sulfur, many authors have studied pH as a control on metal solubility (e.g. Barnes, 1979). In these studies, sulfide mineral precipitation leads to the addition of H^+ in the system. Therefore, precipitation of sulfides from a hydrothermal fluid subsequently increases the acidity of the fluid (Hofstra and Cline, 2000). Although the fluids may be buffered with the host rock, the initial precipitation of sulfides likely decreased pH and then subsequently led to additional dissolution of carbonates at Anarraaq. Although the carbonate dissolution would buffer the pH of the fluid, it is possible that this was a cyclical process at Anarraaq and caused pH fluctuations which impacted the trace element content of the sphalerite.

5.3.5 Lattice-scale controls

In addition to the high degree of structural variability reported for ZnS (Makovichy, 2006), the hexagonal ZnS polymorph, wurtzite, has been suggested to host higher solubility of elements such as Fe, Cd, and Mn (Scott and Barnes, 1972). Because of the structurally complex nature of ZnS, researchers have also investigated potential crystallographic controls on trace element content. Recent advances in nano-scale analytical techniques have shown that trace element heterogeneity in sphalerite extends beyond the micron scale and distributions are sometimes preferentially controlled by lattice-scale variations in the sphalerite structure (e.g. Cook et al., 2015). The potential for wurtzite as well as the structural complexities of sphalerite at Anarraaq are not known, so therefore it cannot be ruled out that the trace element content may also be impacted by nano-scale variations.

5.4 Distribution of Rb in sphalerite

The major focus of this study was to assess the distribution and nature of Rb and Sr in the Anarraaq sphalerite samples. Homogenous Rb concentrations are only apparent in the zoned L2 sphalerite textures, fibrous L2c, and the light tan U1a Anarraaq sphalerite texture (Figure 19, 21, 39).

The substitution of Rb into the sphalerite lattice has been suggested by previous authors, but is problematic due to the large ionic radii of Rb (and Sr) relative to Zn (Nakai et al., 1993; Pettke and Diamond, 1996; Christensen et al., 1996). The results of this study support the theory that some of the Rb and Sr could be present in the lattice of the sphalerite. The previous suggestion of the coupled substitution:



where Me^{3+} is a metal cation (Pettke and Diamond, 1996) was tested through the addition of chalcophile elements to the LA-ICPMS mapping. Rubidium is present in L2a, L2b, and L2d, with an increase in concentration in L2b and the outer zone of L2d (Figure 19). Within the chalcophile maps of these zoned L2 textures, the distribution of Pb, Ag, Sb, and Tl is most similar to the Rb map (Figure 17). Elemental maps of fibrous L2c sphalerite show that Pb, Cu, Ge, Ag, Sb, and Tl are also similar to the Rb maps (Figure 18, 21). The Rb, Pb, As, and Tl maps of sphalerite U1a are comparable (Figure 37, 39). Considering the charge of these ions (Pb^{2+} , Tl^{3+} , and Tl^{1+}), Tl is the only candidate that agrees with the Me^{3+} suggestion of Pettke and

Diamond (1996), however, only Tl^+ has been suggested in previous studies (Xiong, 2007). Additionally, Sb (likely Sb^{3+}) in the lower ore zone does show a similar distribution to Rb which agrees with the occasional weak Sb and Rb correlation in spot analyses of Laisvall sphalerite (Saintilan et al., 2015). However, As has a more obvious spatial correlation with Rb in the upper ore zone (Figure 17, 18, 19, 21, 37, 39). In general, Rb is more abundant in Fe poor sphalerite (Figure 17, 18, 19, 21, 31, 37, 39), therefore Fe^{3+} is not a potentially coupled substituent with Rb. A comparison of the Rb spatial distribution relative to the chalcophile distributions in the LA-ICPMS maps of this study show that Rb is homogenous in some Anarraaq sphalerite, however, evidence for a coupled substitution involving Rb is not uniform across the maps and substitution mechanisms are also not evident. Additionally, this Rb could reside in crystal defects or octahedral voids, as proposed by Nakai et al., (1993); Pettke and Diamond, 1996; and Saintilan et al., (2015), rather than in the sphalerite lattice.

Rubidium is commonly present as isolated pixels or clusters of several pixels in sphalerite L1, L2a, L2c, L4, and U1 (Figure 11, 19, 21, 30, 39, 40). Because the Rb frequently correlates with both Al and Si, the Rb bearing inclusions are interpreted to be silicate minerals. These silicate inclusions could be the result of syngenetic precipitation within the sphalerite, incorporation of pre-ore matrix material, or the result of post-mineralization fluid flow.

The mineralogy of the Kuna Formation has been investigated using X-ray diffraction analyses and consists of quartz, muscovite, illite and organic matter (Slack et al., 2004a). The matrix material located in the lower ore zone consists of disseminated sphalerite, pyrite, and galena hosted in quartz and Kuna Formation mudstone (Figure 5, 12, 14, 15, 27). The lithophile elements in the matrix consist of Rb, Al, and Si, based on X-ray and LA-ICPMS element mapping (Figure 8, 11, 14, 15). In some samples, the matrix cross cuts the sphalerite, however, in other samples, clasts of the matrix are hosted in the sphalerite (Figure 19). This complicated timing is the result of sulfide precipitation prior to lithification of the sediment. Other inclusions consisting of Rb, Al, and Si in sphalerite L2c, L3, U1 (Figure 20, 21, 25, 39, 41) do not show any clear cross cutting relationship within the sphalerite and are possibly syngenetic with the sphalerite, or mudstone that was trapped during rapid sphalerite precipitation.

Rubidium, Al, and Si bearing veinlets, only sometimes visible in transmitted light microscopy, BSE imaging, or X-ray element maps, are clearly evident in LA-ICPMS maps which represent micro-veinlets cutting across sphalerite L4 and U1c (Figure 28, 30, 40). Because

significant post-ore fluid flow during the Brookian orogeny has been reported at Red Dog (Kelley et al., 1998; Leach et al., 2004) and secondary muscovite, associated with quartz and pyrite, with young ages has been identified in the district ($^{40}\text{Ar}/^{39}\text{Ar}$ ages of ~195 Ma above the Anarraaq deposit and ~126 Ma within the main deposits; (Rombach and Layer et al., 2004), it cannot be ignored that these micro-veinlets could significantly postdate the sphalerite.

Based on the previous observations of pre-mineralization muscovite and illite in the Kuna Formation (Slack et al., 2004) as well as post-mineralization muscovite (Rombach and Layer et al., 2004), the potential size of the silicate inclusions identified in this study can be inferred. Assuming muscovite with an Al concentration of 20.3 wt%, using a 20x20 μm laser aperture, assuming an ablation depth of 1 μm , a single pixel with a concentration of ~20 wt% Al would indicate an inclusion of 20x20 μm and <1 wt% would indicate a submicron size inclusion. Using illite with an Al concentration of 9 wt% would decrease the potential size of the inclusion by over 50%. If these assumptions are correct, many Rb bearing inclusions in the Anarraaq deposit are likely sub-micron in size (Figure 11, 19, 20, 30) and this explains the lack of visible microscopic inclusions in L4 and somewhat in L2c (Figure 20, 30), however, this is also complicated by the averaging and smoothing effects of CellSpace.

In addition to silicate inclusions, Rb distributions sometimes spatially correlate well with Na in L2c and with Na and Sr in L5 (Figure 21, 42). Because of a lack of correlation with other elements, these inclusions are interpreted as Rb rich fluid inclusions.

Aside from sphalerite, Rb and Sr in the LA-ICPMS maps are commonly associated with pyrite (Figure 19, 25, 30, 34, 39, 40) which sometimes clearly predates (Figure 39, 40) or postdates the sphalerite (Figure 19).

5.5 Distribution of Sr in sphalerite

Strontium concentrations have a homogeneous distribution in sphalerite L4c veins and colloform bands (Figure 30, 31). Sphalerite U1a also appears to contain homogeneously distributed Sr and this is the only texture where homogeneous Rb and Sr spatially correlate.

Strontium commonly occurs as isolated high concentrations (Figure 19, 20, 25, 30, 34, 39, 40) and sometimes these occurrences correlate with Ca present in L2c and L3 sphalerite (Figure 20, 25) and therefore it is interpreted that these are Sr bearing carbonates.

Sphalerite L2c, L3, L5, and U1a contain inclusions of Sr which are not present in obvious veins (Figure 20, 25, 34, 39). The L2c carbonate inclusions are not evidently cutting the sphalerite and could be syngenetic with sphalerite or the incorporation of earlier carbonates. In zoned L2 sphalerite, L4 veins, L5, and the U1c texture, Sr and Ca are clearly present as late carbonate bearing veins (Figure 17, 19, 30). Strontium and Ca also occur together in L4 and U1c hosted veins which also contain Rb, Al, and Si (Figure 30). Sphalerite L5 sometimes contains abundant visible inclusions of fluid and opaque minerals, which are likely sulfides, and Sr correlates well with the Na in this area (Figure 33), therefore these are interpreted as Sr rich fluid inclusions.

The isolated Sr bearing inclusions could be the result of syngenetic precipitation within the sphalerite or incorporation of host rock during sphalerite precipitation. The Kuna Formation also hosts carbonate units which are dominantly calcareous radiolarites within a carbonate matrix (Dumoulin et al., 2004). Strontium is thought to be mostly hosted in carbonates and possibly also material containing phosphorus (Slack et al., 2004). Anarraaq sulfide mineralization involved carbonate replacement and secondary calcite is common in the deposit (Kelley et al., 2004b), therefore primary carbonates could have been completely dissolved and secondary calcite was precipitated during ore mineralization.

Late stage carbonate veins are also present throughout Anarraaq (Kelley et al., 2004b) and even later fluid flow during the Brookian orogeny resulted in abundant quartz and carbonate veins in the Brooks Range (Kelley et al., 1998). Unlike the isolated occurrences, the Sr bearing carbonate veins are potentially the result of late fluid flow which could have occurred shortly after sulfide mineralization or as recent as the Brookian orogeny.

5.6 Implications for the Rb-Sr dating of sphalerite

The main goal of this study was to investigate whether Rb-Sr bearing inclusions were present in Anarraaq sphalerite and whether the samples are suitable for Rb-Sr dating. The Anarraaq sphalerite displays abundant colloform and banded textures which are the result of rapid precipitation. Any hydrothermal minerals and fluid inclusions which formed and trapped Rb and Sr at the same time as the sphalerite would not impact age dating and several of the Anarraaq textures (L3, L5, U1a) contain hydrothermal mineral inclusions that are syngenetic with the sphalerite (Figure 25, 35, 39). However, some of these inclusions are likely the result of

mechanical entrainment of host rock fragments or remnant carbonates preserved after replacement by sulfides.

The more recent Rb-Sr sphalerite dating methods have pre-leached the sample fractions (prior to crushing) in acids to deal with the issue of carbonate inclusions (10% acetic for Christensen et al., 1995a, 1995b; 1.5 N HCL for Nelson et al., 2002; 2 N HCL for Efimenko et al., 2014). Schneider et al., (1999) and Saintilan et al., (2015) added stronger acid (2 N HF) to their fraction pre-leach in an attempt to also remove potential non-carbonate mineral inclusions on the surface of the fractions. Saintilan et al., (2015) began soaking sphalerite residues again in 2 N HCL and 2 N HF for 15 minutes each, following crushing. This would likely remove any carbonates that were present in the sphalerite, however, any silicate inclusions would remain. Following pre-leaching and rinsing, the residue is typically dissolved in 6 N HCL (Christensen et al., 1995a, 1995b; Nelson et al., 2002; Efimenko et al., 2014; Saintilan et al., 2015) and Brannon et al., (1996a) points out that although silicate contaminants would not be dissolved in this solution, cation leaching from the silicates during the digestion is still an issue for contamination. Furthermore, any pyrite inclusions would be dissolved into the sphalerite residue and because the epigenetic pyrite appears to host Rb (Figure 19, 39), this would compromise the accuracy of the age.

The presence of mineral inclusions and Rb and Sr homogeneously distributed in the sphalerite means that accurate Rb-Sr dating of the Anarraaq sphalerite would be extremely challenging. Although the carbonate inclusions can be removed with the pre-leaching of sphalerite residues (Saintilan et al., 2015), the silicate and pyrite inclusions are significant enough in size and present at an abundance that make the current method of hand picking and acid digestion impossible to avoid these inclusions. Even the application of an in situ sampling technique to preferentially sample inclusion free material would likely encounter inclusions at depth as the mapping conducted in this study only ablated and analyzed ~1 μm of the surface material.

These findings have a significant impact on the utility of the Rb-Sr method to date sediment hosted base metal deposits. If attempted in the future, any age dating should be prefaced by a microscopic analytical investigation similar to this study. Reconnaissance element mapping using LA-ICPMS must first be carried out to determine the presence and spatial

distribution of potential Rb-Sr bearing mineral and fluid inclusions. These findings could later be coupled with observations from the isochron plot to aid in identifying any potential issues.

5.7 Distribution of Na in sphalerite

In addition to the fluid inclusions discussed above, Na also has a homogenous distribution in some mapped areas (zoned L2, fibrous L2c, veins of L4, and areas of U1a; Figure 19, 20, 21, 30, 39). This observation is supported by the negative correlation between the Na and Zn concentrations in the EPMA data (Figure 6e). Fluid inclusion salinity at Red Dog has been reported to vary between 14 – 19 wt% NaCl equivalent (Leach et al., 2004). As such, the possibility that the Na detected is hosted by fluid inclusions was assessed by also analyzing Cl using X-ray mapping and EPMA spot analyses. Sodium present in the zoned L2 and U1a LA-ICPMS maps correlates with the Cl X-ray maps, however, the Cl occurs in such low concentrations (or the fluid inclusions are submicron) in the maps that the distribution could be the result of X-ray continuum and may not be real (Figure 15, 19, 36, 39). Aside from the low concentration Cl in zoned L2 and U1a, Cl was not abundantly distributed in the other X-ray maps or the EPMA data (Figure 6f, 10, 16, 28).

It is possible therefore, that Na may be present in the sphalerite lattice as a substituent for Zn. Because of the +1 charge of the Na ion and the +2 charge of Zn, this substitution would require a coupled substitution with a 3+ ion similar to that which was suggested for Rb by Pettke and Diamond (1996), however, such an ion could not be confidently identified in this study and further work is needed to resolve this issue. An alternative explanation is that Na resides in crystal defects or the octahedral void of the sphalerite lattice as suggested for Rb and Sr by Nakai et al., (1993); Pettke and Diamond, 1996; and Saintilan et al., (2015).

5.8 Implications for geometallurgy

Although this study was focused on small scale analyses of sphalerite and not bulk lithochemical analyses, these results provide valuable insights regarding the distribution of minor and trace elements in sphalerite, the dominant ore mineral, of the Anarraaq deposit. For example, recent work has shown that high Fe can negatively impact sphalerite flotation cells (Boulton et al., 2005; Simpson et al., 2011).

Furthermore, knowing the trace element distribution of sphalerite ore can also aid in forecasting the presence of penalty and credit elements in Zn concentrates. For example, Hg is a penalty element and if it is not solely present as HgS in sphalerite, it cannot be removed by froth flotation (Grammatikopoulos et al., 2006). In contrast to penalty elements, additional elements such as Cd, Ge, Ga, In, and Tl can be produced as by-products of refining Zn concentrate (Cook et al., 2009 and references therein). Understanding the presence and distribution of penalty and credit elements, therefore, is an important consideration for the economics of a deposit.

If the distributions of elements which impact recovery or result in penalties are known, short range planning can incorporate blending which involves mixing of different material from various parts of a deposit for processing. Efficient forecasting of the minor elements in the ore minerals can lead to effective blending and prevent recovery loss and penalty accruals.

6 Conclusions

The compositional variations in the Anarraaq sphalerite are attributed to fluctuations in physio-chemical parameters during ore formation such as fluid mixing, fluid mixing prior to infiltration of the host rock, or buffering with wall rock during deep basement circulation. Iron is the most minor element present in Anarraaq sphalerite and largely controls the color of, however, in the absence of significant Fe, the chalcophile elements appear to also have an impact on color. The spatial distributions of chalcophile elements are most complex in the lower ore zone and include oscillatory zoning somewhat similar to the Fe controlled color zoning (mostly seen in Cd and Hg), oscillatory zoning which is independent of the Fe zoning (which typically includes Pb, Cu, Ag, Ge, As, Sb, and Tl), irregular or sectorial zoning (L5 sphalerite), and isolated inclusions of sulfides. Additionally, the upper ore zone is host to many homogeneous chalcophile distributions.

The Rb and Sr sometimes appear to be homogeneously distributed in Anarraaq sphalerite and this could be the result of lattice bound Rb and Sr either as a direct substituent in the structure itself, in crystal defects, or as abundant submicron inclusions. If these elements are indeed present as substituents, this would require a coupled substitution in order to maintain charge balance. However, the addition of chalcophile elements to the LA-ICPMS mapping did not reveal a clear correlation between Rb or Sr and any single chalcophile element. This suggests the substitution mechanisms could be even more complex than originally proposed. Although the

chalcophile element mapping failed to reveal a uniform coupled substitution involving Rb and Sr, the maps reveal a complex heterogeneity and distribution of these elements well beyond what was anticipated.

More often, Rb and Sr are present in pyrite inclusions or inclusions which contain additional lithophile elements indicating that Rb is present in aluminosilicate inclusions and Sr is present in carbonate inclusions. Although some isolated inclusions may in fact be the result of minerals precipitating from the hydrothermal fluid, syngenetic with the sphalerite, they could also be the result of entrainment during the rapidly precipitating colloform sphalerite. Furthermore, Rb and Sr are also hosted in micro-veinlets which postdate the main stage of ore formation and could be the result of fluid flow during the Brookian Orogeny.

These observations have huge implications for the application of Rb-Sr dating of sphalerite and any future work done using the current dating method should first focus on a detailed spatial investigation of the elements.

6.1 Future work

Continued lithophile mapping of sphalerite hosted in additional deposits would help determine additional patterns in Rb, Sr, and Na in sphalerite textures, precipitation conditions, and post-depositional impacts. Ongoing mapping for lithophile distributions should include additional elements such as K, Ba, and P which were eliminated early in this LA-ICPMS mapping due to low signal during analytical reconnaissance. It would also be very beneficial to couple these observations with isotopic analyses of Rb and Sr sampled by an in-situ technique such as micro-milling. This would aid in correlating specific inclusion features in sphalerite which may negatively impact an isochron age calculation. The high Rb identified in this study that is associated with the inclusions in sphalerite mean that in-situ mass spectrometry techniques such as laser ablation multi-collector plasma mass spectrometry will not be well suited to Rb-Sr sphalerite analysis due to i) the difficulty in resolving the isobaric interference of ^{87}Rb on ^{87}Sr , and ii) the low Sr abundances identified in this study.

An alternative hypothesis to Rb and Sr being hosted in the sphalerite lattice is the possible presence of abundant nano-scale inclusions hosted in the sphalerite. The sites and mechanisms for substitution of these elements would need to be further investigated using nanometer analytical technology such as transmitted electron microscopy (TEM). TEM imaging has been

applied to sulfides to investigate the chemical contents and crystal structure on a nanometer scale (Ciobanu et al., 2011; Cook et al., 2015) and this technique could be applied to investigate whether the homogeneously distributed Rb, Sr, and Na concentrations do reflect lattice bound lithophile elements in sphalerite and the mechanisms of any potential substitution. TEM could also be used to investigate how structural variations between the ZnS polytypes as well as lattice defects may have an impact on this. XANES analyses could be applied to Anarraaq sphalerite to identify ion speciation and coordination of elements. This would help constrain the oxidation (e.g. Bonnet et al., 2017) during sphalerite precipitation as well as investigate the potential for lithophile elements present in the sphalerite lattice.

Chalcophile mapping shows that the trace element content of Anarraaq sphalerite is variable in distribution and that these distributions are extremely complicated. This indicates that there are likely multiple controls on the trace element content. Coupling this level of detailed mapping with additional analyses would be effective at identifying some of these controls. In-situ S isotopic analyses could aid in identifying whether hydrothermal or host rock pore fluid account for each of the chalcophile elements. In-situ Zn or Pb isotopic analyses using a micro-milling technique would help identify any small scale variability in metal sourcing. LA-ICPMS using a laser equipped with very high magnification optics and cathodoluminescence may also be used in the future to identify metals trapped during sulfide mineralization in sphalerite fluid inclusions.

References

- Ayuso, R. A., Kelley, K. D., Leach, D. L., Young, L. E., Slack, J. F., Wandless, G., Lyon, M., & Dillingham, J. L. (2004). Origin of the Red Dog Zn-Pb-Ag deposits, Brooks Range, Alaska: Evidence from regional Pb and Sr isotope sources. *Economic Geology*, *99*(7), 1533–1553. <https://doi.org/10.2113/gsecongeo.99.7.1533>
- Barnes, H. L. (1979). Solubilities of ore minerals. *Geochemistry of hydrothermal ore deposits*, *2*, 404-460.
- Barrie, C. D., Boyce, A. J., Boyle, A. P. P., Williams, P. J. J., Blake, K., Wilkinson, J. J., Lowther, M., McDermott, P., & Prior, D. J. (2009). On the growth of colloform textures: a case study of sphalerite from the Galmoy ore body, Ireland. *Journal of the Geological Society*, *166*(3), 563–582. <https://doi.org/10.1144/0016-76492008-080>
- Barton, P. B., & Toulmin, P. (1966). Phase relations involving sphalerite in the Fe-Zn-S system. *Geology*, *61*(5), 815–849. <https://doi.org/10.2113/gsecongeo.61.5.815>
- Blevings, S. K., Kraft, J. L., Stemler, J. U., & Krolak, T. E. (2013). An Overview of the Structure, Stratigraphy, and Zn-Pb-Ag Deposits of the Red Dog District, Northwestern Alaska. *Society of Economic Geologists, Special Publication 17*, 361–387.
- Bonnet, J., Cauzid, J., Testemale, D., Kieffer, I., Proux, O., Lecomte, A., & Bailly, L. (2017). Characterization of Germanium Speciation in Sphalerite (ZnS) from Central and Eastern Tennessee, USA, by X-ray Absorption Spectroscopy. *Minerals*, *7*(79), 1–16. <https://doi.org/10.3390/min7050079>
- Boulton, A., Fornasiero, D., & Ralston, J. (2005). Effect of iron content in sphalerite on flotation. *Minerals Engineering*, *18*(11), 1120–1122. <https://doi.org/10.1016/j.mineng.2005.03.008>
- Bradley, D. C., & Leach, D. L. (2003). Tectonic controls of Mississippi Valley-type lead-zinc mineralization in orogenic forelands. *Mineralium Deposita*, *38*(6), 652–667. <https://doi.org/10.1007/s00126-003-0355-2>
- Bradley, D., Leach, D., Symons, D., Emsbo, P., Premo, W., Breit, G., & Sangster, D. F. (2004). Reply to Discussion on “Tectonic controls of Mississippi Valley-type lead-zinc mineralization in orogenic forelands” by S.E. Kesler, J.T. Christensen, R.D. Hagni, W. Heijlen, J.R. Kyle, K.C. Misra, P. Muechez, and R. van der Voo, *Mineralium Deposita*. *Mineralium Deposita*, *39*(4), 515–519. <https://doi.org/10.1007/s00126-004-0420-5>
- Bragg, W. H., & Bragg, W. L. (1913). The Structure of the Diamond. *Nature*, *91*(2283), 557.
- Bragg, W. L. (1914). The Analysis of Crystals by the X-ray Spectrometer. *Proceedings of the Royal Society of London. Series A, Containing Papers of a Mathematical and Physical Character*, *89*(613), 468–489.
- Brannon, J. C., Podosek, F. A., & McLimans, R. K. (1992). Alleghenian age of the Upper Mississippi Valley

zinc-lead deposit determined by Rb-Sr dating of sphalerite. *Nature*, 356, 509–511.

Brannon, J.C., Cole, S.C., Podosek, F.A., & Misra, K.C. (1995). Radiometric dating of ancient calcite, Th-Pb and U-Pb isochrons for ore-stage and late-stage calcite from central Tennessee zinc district, an Appalachian-Ouachita age MVT deposit: Geological Society of America, Abstracts with Programs, 27, 118.

Brannon, J.C., Podosek, F.A., & Cole, S.C. (1996a). Radiometric Dating of Mississippi Valley-type Ore Deposits. In: Sangster DF (ed) Carbonate-hosted zinc–lead deposits. *Society of Economic Geologists Special Publication 4*, 536-545.

Brannon, J. C., Cole, S. C., Podosek, F. A., Ragan, V. M., Coveney Jr, R. M., Wallace, M. W., & Bradley, A. J. (1996b). Th-Pb and U-Pb dating of ore-stage calcite and Paleozoic fluid flow. *Science*, 271(November), 491–493.

Cabri, L. J., Campbell, J. L., Leigh, R. G., Maxwell, J. A., & Scott, J. D. (1985). Proton-microprobe analysis of trace elements in sulfides from some massive-sulfide deposits. *The Canadian Mineralogist*, 133–148.

Christensen, J. N., Halliday, A. N., Leigh, K. E., Randell, R. N., & Kesler, S. E. (1995a). Direct dating of sulfides by RbSr: A critical test using the Polaris Mississippi Valley-type ZnPb deposit. *Geochimica et Cosmochimica Acta*, 59(24), 5191–5197. [https://doi.org/10.1016/0016-7037\(95\)00345-2](https://doi.org/10.1016/0016-7037(95)00345-2)

Christensen, J. N., Halliday, A. N., Vearncombe, J. R., & Kesler, S. E. (1995b). Testing Models of Large-Scale Crustal Fluid Flow Using Direct Dating of Sulfides: Rb-Sr Evidence for Early Dewatering and Formation of Mississippi Valley-Type Deposits, Canning Basin, Australia. *Economic Geology*, 90, 877–884.

Christensen, J.N., Halliday, A.N., & Kesler, S.E. (1996). Rb-Sr dating of sphalerite and the ages of Mississippi Valley-type Pb–Zn deposits. In: Sangster DF (ed) Carbonate-hosted zinc–lead deposits. *Society of Economic Geologists Special Publication 4*, 527-535.

Ciobanu, C. L., Cook, N. J., Utsunomiya, S., Pring, A., & Green, L. (2011). Focussed ion beam-transmission electron microscopy applications in ore mineralogy: Bridging micro- and nanoscale observations. *Ore Geology Reviews*, 42(1), 6–31. <https://doi.org/10.1016/j.oregeorev.2011.06.012>

Cook, N. J., & Hoefs, J. (1997). Sulphur isotope characteristics of metamorphosed Cu- (Zn) volcanogenic massive sulphide deposits in the Norwegian Caledonides. *Chemical Geology*, 135, 307–324.

Cook, N. J., Ciobanu, C. L., Pring, A., Skinner, W., Shimizu, M., Danyushevsky, L., Saini-Eidukat, & B., Melcher, F. (2009). Trace and minor elements in sphalerite: A LA-ICPMS study. *Geochimica et Cosmochimica Acta*, 73(16), 4761–4791. <https://doi.org/10.1016/j.gca.2009.05.045>

Cook, N. J., Ciobanu, C. L., Giles, D., & Wade, B. P. (2013). Correlating textures and trace elements in ore minerals.

Cook, N., Etschmann, B., Ciobanu, C., Geraki, K., Howard, D., Williams, T., Rae, N., Pring, A., Chen, G.,

- Johannessen, B., & Brugger, J. (2015). Distribution and Substitution Mechanism of Ge in a Ge-(Fe)-Bearing Sphalerite. *Minerals*, 5(2), 117–132. <https://doi.org/10.3390/min5020117>
- Craig, J. R., & Scott, S. D. (1974). Sulfide phase equilibria. *Sulfide mineralogy*, 1, CS-1.
- Di Benedetto, F., Bernardini, G. P., Costagliola, P., Plant, D., & Vaughan, D. J. (2005). Compositional zoning in sphalerite crystals. *American Mineralogist*, 90(8–9), 1384–1392. <https://doi.org/10.2138/am.2005.1754>
- Dumoulin, J. A., Harris, A. G., Blome, C. D., & Young, L. E. (2004). Depositional Settings, Correlation, and Age of Carboniferous Rocks in the Western Brooks Range, Alaska. *Economic Geology*, 99, 1355–1384.
- Efimenko, N., Schneider, J., Spangenberg, J. E., Chiaradia, M., Adatte, T., & Föllmi, K. B. (2014). Formation and age of sphalerite mineralization in carbonate rocks of Bajocian age in the Swiss Jura Mountains: Evidence of Mesozoic hydrothermal activity. *International Journal of Earth Sciences*, 103(4), 1059–1082. <https://doi.org/10.1007/s00531-014-1015-8>
- Elliot, W. C., & Aronson, J. L. (1987). Alleghanian episode of K-bentonite illitization in the southern Appalachian Basin. *Geology*, 15(8), 735–739. [https://doi.org/10.1130/0091-7613\(1987\)15<735](https://doi.org/10.1130/0091-7613(1987)15<735)
- Fallick, A. E., Ashton, J. H., Boyce, A. J., Ellam, R. M., & Russell, M. J. (2001). Bacteria Were Responsible for the Magnitude of the World-Class Hydrothermal Base Metal Sulfide Orebody At Navan, Ireland. *Economic Geology*, 96(4), 885–890. <https://doi.org/10.2113/gsecongeo.96.4.885>
- Fleet, M. E. (2006). Phase Equilibria at High Temperatures. *Reviews in Mineralogy and Geochemistry*, 61(1), 365–419. <https://doi.org/10.2138/rmg.2006.61.7>
- Gagnevin, D., Menuge, J. F., Kronz, A., Barrie, C., & Boyce, A. J. (2014). Minor elements in layered sphalerite as a record of fluid origin, mixing, and crystallization in the navan Zn-Pb ore deposit, Ireland. *Economic Geology*, 109(6), 1513–1528. <https://doi.org/10.2113/econgeo.109.6.1513>
- Garven, G., & Sverjensky, D. A. (1994). Paleohydrogeology of the Canadian Rockies and origins of brines, Pb-Zn deposits and dolomitization in the Western Canada Sedimentary Basin: Comment and Reply. *Geology*, 243–246.
- Garven, G., Raffensperger, J., Dumoulin, J., Bradley, D., Young, L., Kelley, K., & Leach, D. (2003). Coupled heat and fluid flow modeling of the Carboniferous Kuna Basin, Alaska: implications for the genesis of the Red Dog Pb-Zn-Ag-Ba ore district. *Journal of Geochemical Exploration*, 78–79(2), 215–219. <https://doi.org/10.1016/S0375>
- George, L., Cook, N. J., Cristiana, C., & Wade, B. P. (2015). Trace and minor elements in galena: A reconnaissance LA-ICP-MS study. *American Mineralogist*, 100(2–3), 548–569. <https://doi.org/10.2138/am-2015-4862>
- George, L. L., Cook, N. J., & Ciobanu, C. L. (2016). Partitioning of trace elements in co-crystallized sphalerite–galena–chalcopyrite hydrothermal ores. *Ore Geology Reviews*, 77, 97–116.

<https://doi.org/10.1016/j.oregeorev.2016.02.009>

- Grammatikopoulos, T. A., Valeyev, O., & Roth, T. (2006). Compositional variation in Hg-bearing sphalerite from the polymetallic Eskay Creek deposit, British Columbia, Canada. *Chemie Der Erde - Geochemistry*, 66(4), 307–314. <https://doi.org/10.1016/j.chemer.2005.11.003>
- Goodfellow, W.D., & Lydon, J.W. (2007). Sedimentary-exhalative (SEDEX) deposits: Geological Association of Canada, Mineral Deposits Division, Special Publication 5, 163–183.
- Hearn, P. P., Sutter, J. F., & Belkin, H. E. (1987). Evidence for Late-Paleozoic brine migration in Cambrian carbonate rocks of the central and southern Appalachians: Implications for Mississippi Valley-type sulfide mineralization. *Geochimica et Cosmochimica Acta*, 51(5), 1323–1334. [https://doi.org/10.1016/0016-7037\(87\)90222-5](https://doi.org/10.1016/0016-7037(87)90222-5)
- Heijlen, W., Muchez, P., Banks, D. A., Schneider, J., Kucha, H., & Keppens, E. (2003). Carbonate-Hosted Zn-Pb Deposits in Upper Silesia, Poland: Origin and Evolution of Mineralizing Fluids and Constraints on Genetic Models. *Economic Geology*, 98, 911–932.
- Hnatyshin, D., Creaser, R. A., Wilkinson, J. J., & Gleeson, S. A. (2015). Re-Os dating of pyrite confirms an early diagenetic onset and extended duration of mineralization in the Irish Zn-Pb ore field. *Geology*, 143–146. <https://doi.org/10.1130/G36296.1>
- Hofstra, A. H., & Cline, J. S. (2000). Characteristics and models for carlin-type gold deposits. *Reviews in Economic Geology*, 13, 163–220.
- Jennings, S., & King, A. R. (2002). Geology, exploration history and future discoveries in the Red Dog district, western Brooks Range, Alaska. In D. Cooke & J. Pongratz (Eds.), *Giant Ore Deposits: Characteristics, genesis and exploration* (pp. 151–158).
- Johan, Z. (1988). Indium and germanium in the structure of sphalerite: an example of coupled substitution with Copper. *Mineralogy and Petrology*, 39(3–4), 211–229. <https://doi.org/10.1007/BF01163036>
- Johnson, C. A., Kelley, K. D., & Leach, D. L. (2004). Sulfur and oxygen isotopes in barite deposits of the western Brooks Range, Alaska, and implications for the origin of the Red Dog massive sulfide deposits. *Economic Geology*, 99(7), 1435–1448. <https://doi.org/10.2113/gsecongeo.99.7.1435>
- Johnston, J. D. (1999). Regional fluid flow and the genesis of Irish Carboniferous base metal deposits. *Mineralium Deposita*, 34(5–6), 571–598. <https://doi.org/10.1007/s001260050221>
- Kelley, B. K. D., Leach, D. L., & Johnson, C. A. (1998). Sulfur-, Oxygen-, and Carbon-Isotope Studies of Ag-Pb-Zn Vein Breccia Occurrences, Sulfide-Bearing Concretions, and Barite Deposits in the North-Central Brooks Range, with Comparisons to Shale-Hosted Stratiform Massive Sulfide Deposits. *Geologic Studies in Alaska by the U.S. Geological Survey*, 1998.
- Kelley, K. D., Leach, D. L., Johnson, C. A., Clark, J. L., Fayek, M., Slack, J. F., Anderson, V.M., Ayuso, R.A., & Ridley, W. I. (2004a). Textural, Compositional, and Sulfur Isotope Variations of Sulfide Minerals in

- the Red Dog Zn-Pb-Ag Deposits, Brooks Range, Alaska : Implications for Ore Formation. *Economic Geology*, 99, 1509–1532.
- Kelley, K. D., Dumoulin, J. A., & Jennings, S. (2004b). The Anarraaq Zn-Pb-Ag and barite deposit, northern Alaska: Evidence for replacement of carbonate by barite and sulfides. *Economic Geology*, 99(7), 1577–1591. <https://doi.org/10.2113/gsecongeo.99.7.1577>
- Kelley, K. D., & Jennings, S. (2004). A Special Issue Devoted to Barite and Zn-Pb-Ag Deposits in the Red Dog District, Western Brooks Range, Northern Alaska. *Economic Geology*, 99(7), 1267–1280. <https://doi.org/10.5962/bhl.title.18736>
- Kelley, K. D., Wilkinson, J. J., Chapman, J. B., Crowther, H. L., & Weiss, D. J. (2009). Zinc Isotopes in sphalerite from base metal deposits in the Red Dog District, Northern Alaska. *Economic Geology*, 104(6), 767–773. <https://doi.org/10.5962/bhl.title.18736>
- Kesler, S. E., & Carrigan, C. W. (2002). Discussion on “Mississippi Valley-type lead–zinc deposits through geological time: implications from recent age-dating research” by D.L. Leach, D. Bradley, M.T. Lewchuk, D.T.A. Symons, G. de Marsily, and J. Brannon. *Mineralium Deposita*, 37(8), 800–802. <https://doi.org/10.1007/s00126-002-0291-6>
- Kesler, S. E., Chesley, J. T., Christensen, J. N., Hagni, R. D., Heijlen, W., Kyle, J. R., Muchez, P., Misra, K.C., & van der Voo, R. (2004). Discussion of “Tectonic controls of Mississippi Valley-type lead-zinc mineralization in orogenic forelands” by D.C. Bradley and D.L. Leach. *Mineralium Deposita*, 39(4), 512–519. <https://doi.org/10.1007/s00126-004-0422-3>
- King, A.R., Leach, D.L., Kelley, K.D., Clark, J.L., Young, L.E., Slack, J.F., De Vera, J., & Ayuso, R.A. (2002). A summary of ongoing research in the Red Dog district and possible applications to exploration, in Large, R.R. et al., eds.: Stratiform Zn-Pb-Ag Deposits and Geological Environments, with Emphasis on the Australian and North American Giants: Society of Economic Geologists/Prospectors and Developers Association of Canada (SEG/PDAC) Workshop, Toronto, 2002, 6 p
- Leach, D. L., Bradley, D., Lewchuk, M. T., Symons, D. T. A., De Marsily, G., & Brannon, J. (2001). Mississippi Valley-type lead-zinc deposits through geological time: Implications from recent age-dating research. *Mineralium Deposita*, 36(8), 711–740. <https://doi.org/10.1007/s001260100208>
- Leach, D. L., Bradley, D., Lewchuk, M., Symons, D. T., Premo, W., Brannon, J., & de Marsily, G. (2002). Reply to Discussion on “Mississippi Valley-type lead–zinc deposits through geological time: implications from recent age-dating research” by S.E. Kesler and C.W. Carrigan. *Mineralium Deposita*, 37(8), 803–805. <https://doi.org/10.1007/s00126-002-0292-5>
- Leach, D. L., Marsh, E., Emsbo, P., Rombach, C. S., Kelley, K. D., & Anthony, M. (2004). Nature of hydrothermal fluids at the shale-hosted Red Dog Zn-Pb-Ag deposits, Brooks Range, Alaska. *Economic Geology*, 99(7), 1449–1480. <https://doi.org/10.2113/gsecongeo.99.7.1449>
- Leach, D., Bradley, D., Huston, D. L., Pisarevsky, S., Taylor, R., & Gardoll, S. (2010). Sediment-Hosted Lead-Zinc Deposits in Earth History. *Society of Economic Geologists*, 105, 593–625. <https://doi.org/10.2113/gsecongeo.105.3.593>

- Lepetit, P., Bente, K., Doering, T., & Luckhaus, S. (2003). Crystal chemistry of Fe-containing sphalerites. *Physics and Chemistry of Minerals*, 30(4), 185–191. <https://doi.org/10.1007/s00269-003-0306-6>
- Li, W., Huang, Z., & Yin, M. (2007). Dating of the giant huize Zn-Pb ore field of Yunnan Province, Southwest China: Constraints from the Sm-Nd System in hydrothermal calcite. *Resource Geology*, 57(1), 90–97. <https://doi.org/10.1111/j.1751-3928.2006.00007.x>
- Lockington, J. A., Cook, N. J., & Ciobanu, C. L. (2014). Trace and minor elements in sphalerite from metamorphosed sulphide deposits. *Mineralogy and Petrology*, 108(6), 873–890. <https://doi.org/10.1007/s00710-014-0346-2>
- Makovicky, E. (2006). Crystal Structures of Sulfides and Other Chalcogenides. *Reviews in Mineralogy and Geochemistry*, 61, 7–125. <https://doi.org/10.2138/rmg.2006.61.2>
- Mayfield, C. F., TAILLEUR, I. L., & ELLERSIECK, I. (1988). Stratigraphy, structure, and palinspastic synthesis of the western Brooks Range, northwestern Alaska. *USGS Professional Paper 1399*, 143–186.
- McManus, A., & Wallace, M. W. (1992). Age of Mississippi Valley-Type Sulfides Determined using Cathodoluminescence cement stratigraphy, Lennard Shelf, Canning Basin, Western Australia. *Economic Geology*, 87, 189–193.
- Medford, G. A., Maxwell, R. J., & Armstrong, R. L. (1983). $^{87}/^{86}\text{Sr}$ Ratio Measurements on Sulfides, Carbonates, and Fluid Inclusions from Pine Point, Northwest Territories, Canada: An $^{87}/^{86}\text{Sr}$ Ratio Increase Accompanying the Mineralizing Process. *Economic Geology*, 78, 1375–1378.
- Mizuta, T. (1988). Interdiffusion rate of zinc and iron in natural sphalerite. *Economic Geology*, 83(6), 1205–1220. <https://doi.org/10.2113/gsecongeo.83.6.1205>
- Moore, D. W., Young, L. E., Modene, J. S., & Plahuta, J. T. (1986). Geologic Setting and Genesis of the Red Dog Zinc-Lead-Silver Deposit, Western Brooks Range, Alaska. *Economic Geology*, 81, 1696–1727. <https://doi.org/10.2113/gsecongeo.81.7.1696>
- Moore, T. E., Wallace, W. K., Bird, K. J., Karl, S. M., Mull, C. G., & Dillon, J. T. (1994). Geology of northern Alaska. In *The Geology of North America Vol G-1, The Geology of Alaska*, 49–140.
- Morelli, R. M., Creaser, R. A., Selby, D., Kelley, K. D., Leach, D. L., & King, A. R. (2004). Re-Os Sulfide Geochronology of the Red Dog Sediment-Hosted Zn-Pb-Ag Deposit, Brooks Range, Alaska. *Economic Geology*, 99, 1569–1576.
- Mull, C. G. (1982). The tectonic evolution and structural style of the Brooks Range: an illustrated summary. *Geologic Studies of the Cordilleran Thrust Belt*, 1, 1–45.
- Nakai, S., Halliday, A. N., Kesler, S. E., & Jones, H. D. (1990). Rb-Sr dating of sphalerites from Tennessee and the genesis of Mississippi Valley type ore deposits. *Letters to Nature*, 346(26 July 1990), 354–357. [https://doi.org/10.1016/0021-9797\(80\)90501-9](https://doi.org/10.1016/0021-9797(80)90501-9)

- Nakai, S., Halliday, A. N., Kesler, S. E., Jones, H. D., Kyle, J. R., & Lane, T. E. (1993). Rb-Sr dating of sphalerites from Mississippi Valley-type (MVT) ore deposits. *Geochimica et Cosmochimica Acta*, 57(2), 417–427. [https://doi.org/10.1016/0016-7037\(93\)90440-8](https://doi.org/10.1016/0016-7037(93)90440-8)
- Nelson, J. L., Paradis, S., Christensen, J. N., & Gabites, J. (2002). Canadian Cordilleran Mississippi Valley-Type Deposits : A Case for Devonian-Mississippian Back-Arc Hydrothermal Origin. *Economic Geology*, 97, 1013–1036. <https://doi.org/10.2113/97.5.1013>
- Oftedahl, I. (1940). Untersuchungen u"ber die Nebenbestandteile von Erzmineraleien norwegischer zinkblendfu"render Vorkommen. Skrift. Norsk Vidensk. Akad. Oslo, Math. Naturv. Kl. 8, 1–103
- Ohta, E. (1995). Common features and genesis of tin-polymetallic veins. *Resource Geology Special Issue 18*, 187–195.
- O'Sullivan, P.B., Kelley, K.D., & Jennings, S. (2000). Post-mineralization thermotectonic evolution of the region of the Red Dog Pb-Zn-Ag mine, northwest Alaska [abs. 58], in Noble, W.P., O'Sullivan, P.B., and Brown, R.W., eds., International Conference on Fission Track Dating and Thermochronology, 9th, Lorne, Australia, 2000: Geological Society of Australia Abstracts, 255–257.
- Ostendorf, J., Henjes-kunst, F., Schneider, J., Melcher, F., & Gutzmer, J. (2017). Genesis of the Carbonate-Hosted Tres Marias Zn-Pb-(Ge) Deposit, Mexico: Constraints from Rb-Sr Sphalerite Geochronology and Pb Isotopes. *Society of Economic Geologists*, 112, 1075–1087. <https://doi.org/10.5382/econgeo.2017.4502>
- Pannalal, S.J., Symons, D.T.A., & Sangster, D.F. (2008a). Paleomagnetic evidence for an Early Permian age of the Lisheen Zn-Pb deposit, Ireland. *Economic Geology*, 103, 1641–1655.
- Pannalal, S.J., Symons, D.T.A., & Sangster, D.F. (2008b). Paleomagnetic evidence of a Variscan age for the epigenetic Galmoy zinc-lead deposit, Ireland. *Terra Nova*, 20, 385–393.
- Paul, B., Paton, C., Norris, A., Woodhead, J., Hellstrom, J., Hergt, J., & Greig, A. (2012). CellSpace: A module for creating spatially registered laser ablation images within the Lolite freeware environment. *Journal of Analytical Atomic Spectrometry*, 27, 700–706. <https://doi.org/10.1039/c2ja10383d>
- Pettke, T., & Diamond, L. W. (1995). Rb-Sr isotopic analysis of fluid inclusions in quartz: Evaluation of bulk extraction procedures and geochronometer systematics using synthetic fluid inclusions. *Geochimica et Cosmochimica Acta*, 59(19), 4009–4027. [https://doi.org/10.1016/0016-7037\(95\)00260-7](https://doi.org/10.1016/0016-7037(95)00260-7)
- Pettke, T., & Diamond, L. W. (1996). Rb-Sr dating of sphalerite based on fluid inclusion-host mineral isochrons: a clarification of why it works. *Economic Geology*, 91, 951–956.
- Pfaff, K., Koenig, A., Wenzel, T., Ridley, I., Hildebrandt, L. H., Leach, D. L., & Markl, G. (2011). Trace and minor element variations and sulfur isotopes in crystalline and colloform ZnS: Incorporation mechanisms and implications for their genesis. *Chemical Geology*, 286(3–4), 118–134. <https://doi.org/10.1016/j.chemgeo.2011.04.018>

- Potts, P. J. (1992). *A Handbook of Silicate Rock Analysis*. Springer, New York, 622.
- Pring, A., Tarantino, S., Tenailleau, C., Etschmann, B., Carpenter, M., Zhang, M., Liu, Y., & Withers, R. (2008). The crystal chemistry of Fe-bearing sphalerites: An infrared spectroscopic study. *American Mineralogist*, *93*, 591–597. <https://doi.org/10.2138/am.2008.2610>
- Reynolds, M. A., Gingras, M. K., Gleeson, S. A., & Stemler, J. U. (2015). More than a trace of oxygen: Ichnological constraints on the formation of the giant Zn-Pb-Ag Ba ± deposits, Red Dog district, Alaska. *Geology*, *43*(10), 867–870. <https://doi.org/10.1130/G36954.1>
- Rosa, D., Schneider, J., & Chiaradia, M. (2016). Timing and metal sources for carbonate-hosted Zn-Pb mineralization in the Franklinian Basin (North Greenland): Constraints from Rb-Sr and Pb isotopes. *Ore Geology Reviews*, *79*, 392–407. <https://doi.org/10.1016/j.oregeorev.2016.05.020>
- Riehle, J.R., Fleming, M.D., Molnia, B.F., Dover, J.H., Kelley, J.S., Miller, M.L., Nokleberg, W.J., Plafker, G., & Till, A.B. (1997, May 11). U.S. Geological Survey Geologic Investigations Series I-2585. Retrieved May 09, 2017, from <https://pubs.usgs.gov/imap/i2585/>
- Rombach, C. S., & Layer, P. W. (2004). Geochronology of the western and central Brooks Range, Alaska: Implications for the geologic evolution of the Anarraaq and Red Dog Zn-Pb-Ag deposits. *Economic Geology*, *99*(7), 1307–1322. <https://doi.org/10.2113/gsecongeo.99.7.1307>
- Saintilan, N. J., Schneider, J., Stephens, M. B., Chiaradia, M., Kouzmanov, K., Walle, M., & Fontbote, L. (2015). A middle ordovician age for the laisvall sandstone-hosted Pb-Zn deposit, Sweden: A response to early caledonian orogenic activity. *Economic Geology*, *110*(7), 1779–1801. <https://doi.org/10.2113/econgeo.110.7.1779>
- Schaltegger, U., Zwingmann, H., Clauer, N., Larqué, P., & Stille, P. (1995). K–Ar dating of a Mesozoic hydrothermal activity in Carboniferous to Triassic clay minerals of northern Switzerland. *Schweizerische Mineralogische und Petrographische Mitteilungen*, *75*(2), 163–176.
- Schardt, C., Garven, G., Kelley, K. D., & Leach, D. L. (2008). Reactive flow models of the Anarraaq Zn-Pb-Ag deposit, Red Dog district, Alaska. *Mineralium Deposita*, *43*(7), 735–757. <https://doi.org/10.1007/s00126-008-0193-3>
- Schneider, J., Haack, U., Hein, U. F., & Germann, A. (1999). Direct Rb-Sr dating of sandstone-hosted sphalerites from stratabound Pb-Zn deposits in the northern Eifel, NW Rhenish Massif, Germany. 1287–1290.
- Schneider, J., Melcher, F., & Brauns, M. (2007a). Concordant ages for the giant Kipushi base metal deposit (DR Congo) from direct Rb-Sr and Re-Os dating of sulfides. *Mineralium Deposita*, *42*(7), 791–797. <https://doi.org/10.1007/s00126-007-0158-y>
- Schneider, J., Quadt, A. V., Wilkinson, J. J., & Boyce, A. J. (2007b). Age of Silvermines Irish-type Zn-Pb deposit from direct Rb-Sr dating of sphalerite. In *Digging deeper: Proceedings of the Ninth Biennial SGA meeting: Dublin, Ireland, Irish Association for Economic Geology*. 373–376.

- Scott, S. D., & Barnes, H. L. (1972). Sphalerite-wurtzite equilibria and stoichiometry. *Geochimica et Cosmochimica Acta*, 86, 1275–1295.
- Scott, S. D., & Kissin, S. A. (1973). Sphalerite Composition in the Zn-Fe-S System Below 300°C. *Economic Geology*, 68, 475–479.
- Selby, D., Creaser, R. A., Dewing, K., & Fowler, M. (2005). Evaluation of bitumen as a ¹⁸⁷Re-¹⁸⁷Os geochronometer for hydrocarbon maturation and migration: A test case from the Polaris MVT deposit, Canada. *Earth and Planetary Science Letters*, 235(1–2), 1–15.
<https://doi.org/10.1016/j.epsl.2005.02.018>
- Simpson, D., Bredow, T., Chandra, A., Cavallaro, G., & Gerson, A. (2011). The effect of iron and copper impurities on the wettability of sphalerite (110) surface. *Journal of Computational Chemistry*, 32, 2022–2030. <https://doi.org/10.1002/jcc>
- Slack, J. F., Dumoulin, J. A., Schmidt, J. M., Young, L. E., & Rombach, C. S. (2004a). Paleozoic sedimentary rocks in the Red Dog Zn-Pb-Ag district and vicinity, western Brooks Range, Alaska: Provenance, deposition, and metallogenic significance. *Economic Geology*, 99(7), 1385–1414.
<https://doi.org/10.2113/gsecongeo.99.7.1385>
- Slack, J. F., Kelley, K. D., Anderson, V. M., Clark, J. L., & Ayuso, R. A. (2004b). Multistage hydrothermal silicification and Fe-Tl-As-Sb-Ge-REE enrichment in the Red Dog Zn-Pb-Ag district, northern Alaska: Geochemistry, origin, and exploration applications. *Economic Geology*, 99(7), 1481–1508.
<https://doi.org/10.2113/gsecongeo.99.7.1481>
- Slack, J. F., Selby, D., & Dumoulin, J. A. (2015). Hydrothermal, biogenic, and seawater components in metalliferous black shales of the Brooks Range, Alaska: Syndimentary metal enrichment in a carbonate ramp setting. *Economic Geology*, 110(3), 653–675.
<https://doi.org/10.2113/econgeo.110.3.653>
- Symons, D. T. A., & Sangster, D. F. (1992). Late Devonian paleomagnetic age for the Polaris Mississippi Valley-type Zn-Pb deposit, Canadian Arctic Archipelago. *Canadian Journal of Earth Sciences*, 29, 15–25.
- Symons, D. T. A., Sangster, D. F., & Leach, D. L. (1995). A Tertiary age from paleomagnetism for Mississippi Valley-type zinc-lead mineralization in upper Silesia, Poland. *Economic Geology*, 90(4), 782–794.
- Symons, D.T.A., Sangster, D.F., & Leach, D.L. (1996). Paleomagnetic Dating of Mississippi Valley-type Pb-Zn-Ba Deposits. In: Sangster DF (ed) Carbonate-hosted zinc-lead deposits. *Society of Economic Geologists Special Publication 4*: 515-526
- Symons, D. T. A., & Stratakos, K. K. (2000). Palaeomagnetic dating of dolomitization and Mississippi Valley type zinc mineralization in the Mascot Jefferson City district of eastern Tennessee: a preliminary analysis. *Journal of Geochemical Exploration*, 69–70, 373–376.

- Symons, D.T.A., Pannalal, S.J., Kawasaki, K., Sangster, D.F., & Stanley, G.A. (2007). Paleomagnetic age of the Magcobar Ba deposit, Silvermines, Ireland, in Andrew, C.J., et al., eds., *Mineral exploration and research: Digging deeper*: Dublin, Irish Association for Economic Geology, 377–380.
- Tauson, V. L., & Chernyshev, L. V. (1977). Phase relationships and structural features of ZnS-CdS mixed crystals. *Geochemistry International*, 14, 11-22.
- Teck Resources Limited. (2017). 2016 Annual Information Form: February 23, 2017 (48-51, Rep.).
- The Iolite Team. (2015). *Iolite 3 User's Manual*.
- Tompkins, L. A., Pedone, V. A., Roche, M. T., & Groves, D. I. (1994). The Cadjebut Deposit as an Example of Mississippi Valley-Type Mineralization on the Lennard Shelf, Western Australia - Single Episode or Multiple Events? *Economic Geology*, 89, 450–466. <https://doi.org/10.2113/gsecongeo.89.3.450>
- Ubide, T., McKenna, C. A., Chew, D. M., & Kamber, B. S. (2015). High-resolution LA-ICP-MS trace element mapping of igneous minerals: In search of magma histories. *Chemical Geology*, 409, 157–168. <https://doi.org/10.1016/j.chemgeo.2015.05.020>
- Wilkinson, J. J., Eyre, S. L., & Boyce, A. J. (2005). Ore-forming processes in Irish-type carbonate-hosted Zn-Pb deposits: Evidence from mineralogy, chemistry, and isotopic composition of sulfides at the Lisheen Mine. *Economic Geology*, 100(1), 63–86. <https://doi.org/10.2113/100.1.0063>
- Wilkinson, J. J., Vowles, K., Muxworthy, A. R., & Niocaill, C. Mac. (2017). Regional remagnetization of Irish Carboniferous carbonates dates Variscan orogenesis, not Zn-Pb mineralization. *Geology*, 45(7), 1–4. <https://doi.org/10.1130/G39032.1>
- Xiong, Y. (2007). Hydrothermal thallium mineralization up to 300C: A thermodynamic approach. *Ore Geology Reviews*, 32(1–2), 291–313. <https://doi.org/10.1016/j.oregeorev.2006.10.003>
- Yardley, B. W. D. (2005). 100th Anniversary Special Paper: Metal concentrations in crustal fluids and their relationship to ore formation. *Economic Geology*, 100(4), 613–632. <https://doi.org/10.2113/gsecongeo.100.4.613>
- Ye, L., Cook, N. J., Ciobanu, C. L., Yuping, L., Qian, Z., Tiegeng, L., Wei, G., Yulong, Y., & Danyushevskiy, L. (2011). Trace and minor elements in sphalerite from base metal deposits in South China: a LA-ICPMS study. *Ore Geology Reviews*, 39(4), 188-217.
- Young, L. E. (2004). A geologic framework for mineralization in the Western Brooks Range, Alaska. *Economic Geology*, 99(7), 1281–1306. <https://doi.org/10.2113/gsecongeo.99.7.1281>
- Zhou, J., Huang, Z., Zhou, M., Li, X., & Jin, Z. (2013). Constraints of C-O-S-Pb isotope compositions and Rb-Sr isotopic age on the origin of the Tianqiao carbonate-hosted Pb-Zn deposit, SW China. *Ore Geology Reviews*, 53, 77–92. <https://doi.org/10.1016/j.oregeorev.2013.01.001>